

Positron Emission Tomography

FOPRA No. 65

Date Performed: 10 July, 2018
TU Muenchen, Garching

Authors: Bryan Chambers (b.chambers@tum.de)
Caroline Dahlqvist (caroline.dahlqvist@tum.de)

Supervisor: Erwin Gutmiedl (erwin.gutmiedl@my.tum.de)

Introduction

Positron Emission Tomography (PET) is a functional modality, where instead of imaging the anatomy of the object or patient the physiological processes are imaged instead. The method is heavily used in both medicine and research where processes can be monitored such as brain activity, blood or glucose flow. There are two processes contributing to the production of positrons; pair production and β^+ decay, the latter of which are of most importance in PET. In both processes the energy required to initiate the processes is $1022 \text{ keV}/c^2$, the total energy of an electron and a positron, only then is the momentum and energy conserved. In pair production, a photon of enough energy interacts with an atomic nucleus and creates an electron-positron pair. β^+ decay occurs when a neutron deficient radionuclide decays to a more energetically favourable state by converting a proton to a neutron, a positron (to balance the charge) and an electron-neutrino. The excess of kinetic energy is shared between the daughter nuclei the positron and neutrino (which has negligible mass). The daughter nucleus is then in an excited state and de-excites with the emission of a gamma photon with a characteristic energy 1022 keV . The generated positron is ejected from the nucleus and has an energy spectrum depicting how the energy is split between the positron and neutrino. The maximum energy depends on the mass difference of the parent and daughter nucleus and the mean kinetic energy is around 33 % of the maximum energy.

The positron does not travel far before encountering its antiparticle, an electron, in the surrounding material and quickly loses its kinetic energy due to coulomb interactions. The range the positron travels, depending on the initial energy, is typically between 0.1 to 1.0 mm. In the collision, for a short time, a hydrogen-like state is formed, called positronium, with a lifetime of about 10^{-10} s after which the electron and positron annihilate. During this state, the mass of the two annihilated particles is converted into mass and shared between at least two photons. The kinetic energy is negligible compared to the masses and since the reaction occurs when the particles are almost at rest, the momentum is almost zero. Thus the energy, see Einstein's mass energy equivalence below, is mainly from the particles' masses.

$$E = mc^2 = m_{e^-}c^2 + m_{e^+}c^2$$

For energy and momentum to be conserved for the two particles, two photons are generated and ejected into opposite direction, 180° apart. The total energy of $1022 \text{ keV}/c^2$ is split equally between them and in each direction a photon with initial energy $511 \text{ keV}/c^2$ can be detected and provide spatial information since the annihilation event occurs close to the decay of the radionuclide. Forming a line between the two back-to-back photons is referred to the '*line of response*' (LOR) and it is along this line that the event took place, see fig. 1. What also is imperative is the timing of the detected photons, to ensure that the photons are detected in coincidence from the same annihilation event. The region of valid LOR's between an opposing detector pair is defined by the size of their active area. There is one annihilation per decay of the radionuclide.

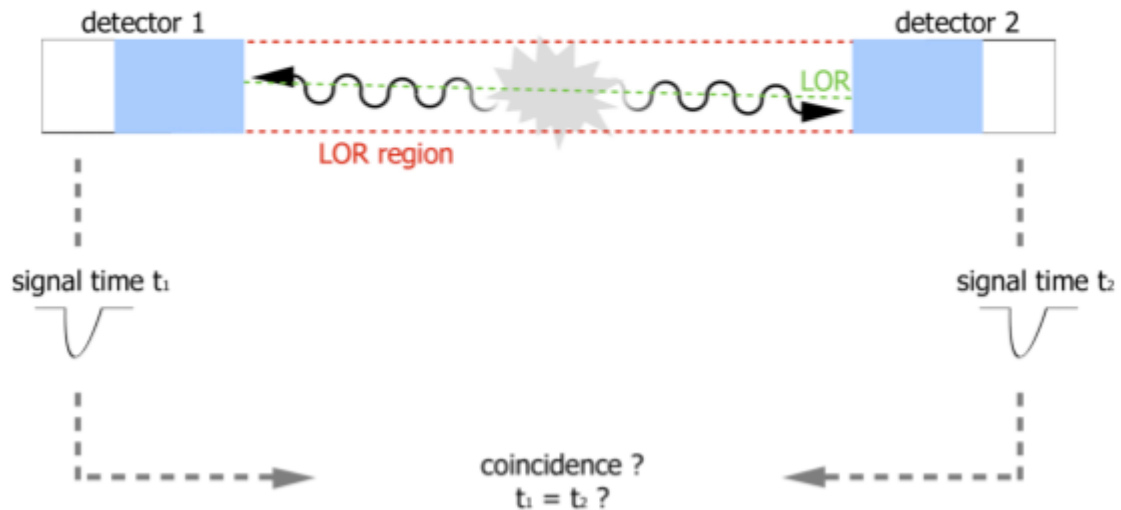


Fig. 1: The 'Line of Response (LOR)' for coincidence detection.

The radionuclides which are used all behave chemically as their non radioactive counterpart, are harmless (chemically) and does not alter or change biological processes. This is important since the naturally occurring processes is the target of the imaging. They are generally short lived and have to be produced with an accelerator in close proximity to the imaging process. The radioactive nuclei are used to replace either their non-radioactive counterpart or an OH⁻ group in the chosen 'tracer'. A commonly used tracer in PET is FDG (fluorodeoxyglucose) with decaying ¹⁸F in a glucose molecule. The distribution of glucose is then imaged with the help of the radio-nuclei. This is essential since cancer tissue has a higher consumption of glucose than healthy tissue and therefore more of the tracer is accumulated there. The brain also has a high glucose consumption and some of the tracer will also end up in the urine bladder. The brain's high glucose uptake can also be used to monitor brain activity. For calibration it is common to use a ²²Na source which is a β^+ emitter.

Experimental Setup

The main hardware for the experiment are the ring detector, and the readout PC. The ring detector can be seen in fig. 2. The six trapezoidal shaped metal compartments are detector modules. Each one has two rows of APDs (avalanche photodiodes) which serve as the radiation detectors of a source placed in the middle of the six detectors. Originally the device was created for performing PET scans on small animals, which explains why the source region is so small. During a scan the platform in the middle will rotate the source so the scan covers all angles. The detector system is referred to as *MADPET*. Each of the six detector modules has two rows of eight channels, giving a total of 96 channels. APD's are essentially a n-p semiconductor that will be operated in the 'reverse bias' mode to increase the resistance of an external current applied to the semiconductor.

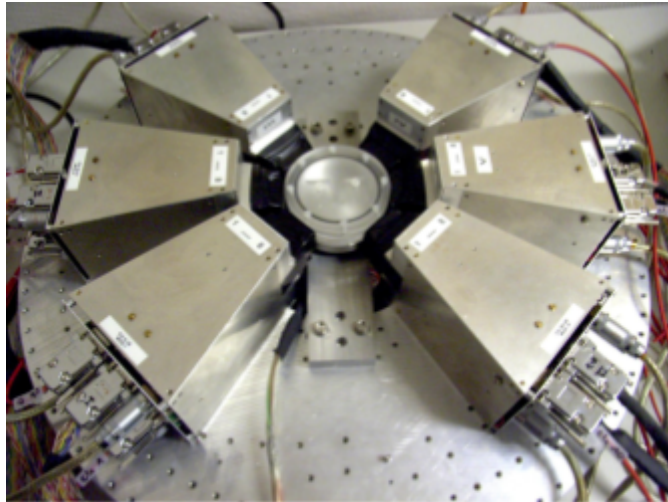


Fig. 2: The MADPET set up of six ADPs surrounding a source

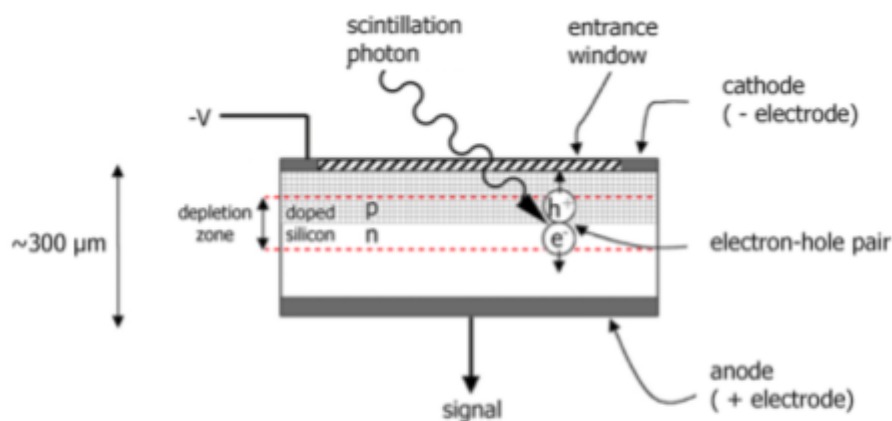


Fig. 3: A semiconductor p-n diode, demonstrating the process of signal creation in an APD detector.

The ADPs have an efficiency of about 0.75 in terms of incident detected radiation and a gain of $10^2 - 10^3$. The gain is due to a 'breakdown' process whereby a photons collides with an electron-hole pair and then a freed electron will gain a significant amount of kinetic energy from the electric field supplied between the anode and cathode that it knocks out other electrons in the semiconductor, and they in turn contribute to the current. For this reason we call it an 'avalanche photodiode', shown in fig. 3.

There are some advantages and disadvantages of using the ADP as a radiation detector. The advantages are they have a compact assembly, they can operate in high magnetic fields (up to 9.4 T) making them suitable for use in conjunction with MRI, and their energy and time performance is comparable to that of a PMT. The disadvantages are that they have

relatively low gain, are highly influenced by ambient temperature, and they require more calibration.

Signals created by the channels in the MADPET are processed by one of three SADCs (sampling analog to digital converters). Each SADC handles 32 of the 96 channels and has a J2-USB card with a single USB port for reading the data. A USB cable connects the SADC to the PC running on Linux for data acquisition, data processing, and image reconstruction. One of the J2-USB cards also activates the motor for rotating the source. See fig.4 for a schematic of the readout system.

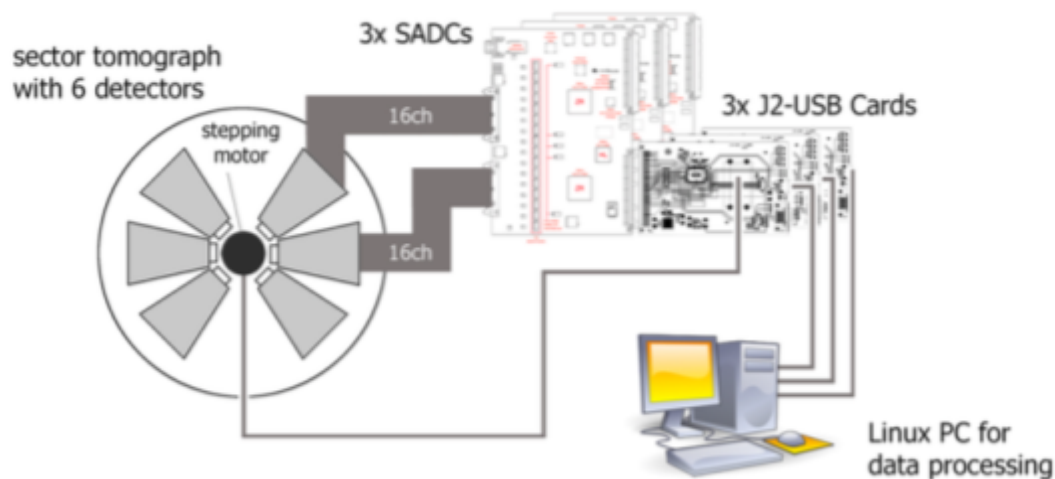


Fig. 4: A schematic displaying the integration of the ring detector, signal converters, and readout.

Method / Experimental Procedure

Initialization and firmware

The program *isegCANHVControl* is used to control the bias voltage delivered to the detector system. To make sure the SADCs are on the upper green LED on each one should be lit and both red LED's on each J2-USB should be lit as well. Next the firmware of the FPGAs is loaded with the PC which enables the SADC to take data. This is done in the Linux directory. In addition the data is recorded and readout in the Linux. The hardware limits is set to 410 V, 0.60 mA and 5 V/s ramp up speed yielding a 80 s long ramp-up procedure.

Taking Data

To read data from the SADC modules at a fixed angle we open the program *sacdata*. The histograms are constructed by a program called *streamusbhist*. The data is sent from

sacdata to **streamusbhist** and the spectrum is built. Viewing the histograms while data comes in can be useful because it allows the setting of energy and voltage thresholds for each channel. The data analysis, detector calibrations, and image constructions are based on what is termed as a ROOT tree. ROOT is a program commonly used for analysis of particle physics data. A 'tree' is basically a hierarchy of storing data and consists of 'leaves' and 'branches'. The function of the leaves is to store data and the branch's is to group it. For example, there are two groups of data called 'events' and 'data'. The 'events' branch contains leaves of data such as peak maxima or signal baseline for the channels and the data branch contains leaves that in turn contain the data about ADC pulse samples. The 'trees' are created by a program called **createtree**.

Energy Calibration

As previously mentioned, the ADPs are temperature sensitive so a photons of equivalent energy could produce a varying amplitude for a measured signal. In addition, each ADP has different calibration properties and the cable lengths between them and the SADCs may not be the same necessarily. A stable thermal environment is crucial along with calibrating the instrumentation.

The value of the ADC channel (see horizontal axis of fig. 5) is proportional the energy of an incoming photon and the vertical axis is the number of entries. The sum of the entries creates a peak at 511 keV. The calculation for the energy of a given channel E_c , is given by:

$$E_c = (511 \text{ keV} / \mu_p) \cdot c_{ADC}$$

Where μ_p is the mean value of the energy of the photopeak in channel value (such as 311 for the 511 keV peak) and c_{ADC} is the channel value of the analog to digital converter. Notice in the graph in fig. 5 there are red, green, and yellow intensity plots. The sum of the three is black. The red plot is the data from the ^{22}Na source and would be the data of interest for us, the yellow plot is background radiation, and the green plot is due to Compton scattering that occurs in the detector. Also all channels below 150 are cut off to reject unnecessary data.

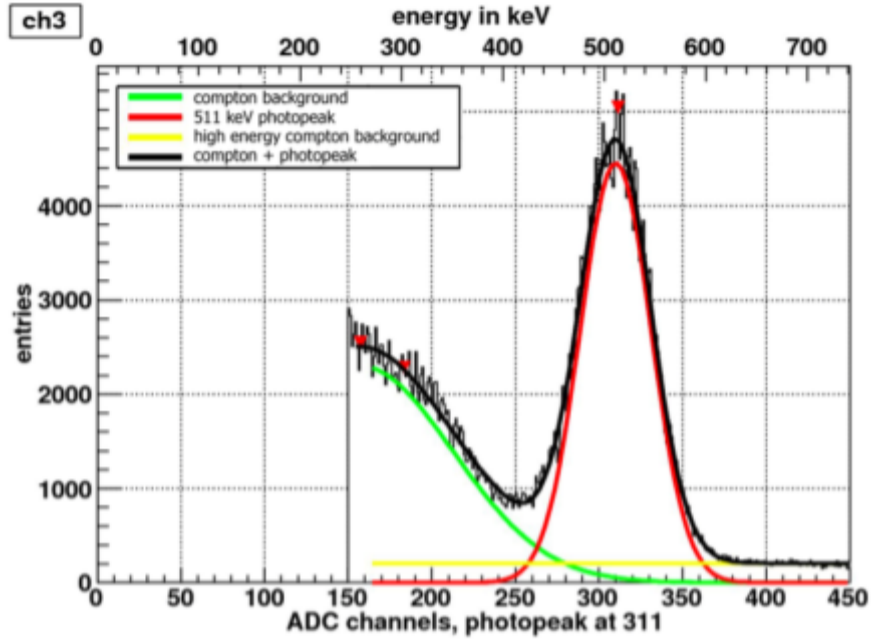


Fig. 5: This figure shows the detector readout, entries vs. channel for an APD with the calibrated energy at the top. Included are the different contributing processes in the resulted readout.

In the experiment the calibration is done for one channel using automated software, and the rest of the channels will conveniently be calibrated automatically placing the histograms into one pdf file.

Fitting and Resolution of the Spectrums

The program 'ROOT' is used to investigate the channel peaks. To calculate the resolution of a detector channel a Gaussian functions must be fitted to the photopeak of the channel. The resolution of the peak can be found by

$$\frac{\Delta E}{E} [\%] = \frac{\sigma_f}{\mu_f} \cdot 100$$

Where σ_f is the standard deviation and μ_f is the mean of the fit. The smaller this ratio is the better the resolution, i.e. the more narrow a peak is the higher the resolution.

Time Calibration

Knowing the precise time photon is detected by the channels is a critical factor in determining the image quality of a PET scan. Factors that create asynchronous detections of

the same event for the different channels can be varying preamplification properties of a signal and various cable lengths.

As an example, consider fig.6 shown below. There are four channels labeled 0-3 and there will be four corresponding LORs.

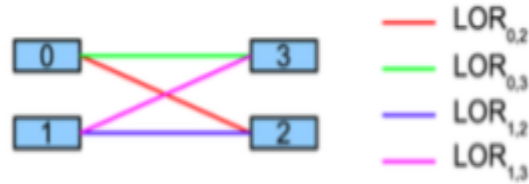


Fig. 6: A depiction of the lines of LORs for four detectors.

According to the electronics the peaks created for each LOR occur at slightly different times, as shown on the left for fig. 7 and this results in a broadening of the Gaussian peak and a broader coincidence window. We can get a tighter fit for the LOR's by doing a time calibration done automatically by a program called **tcal** which analyzes the data from the ROOT tree, as shown in the right of fig. 7.

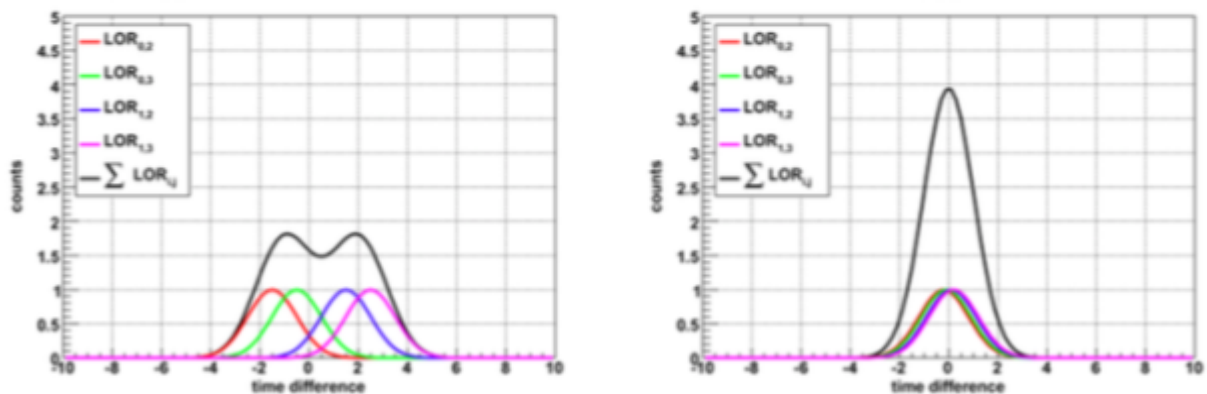


Fig. 7: Shows the LOR peaks and the relative time difference between them (left). The time differences are accounted for to create a synchronous signal (right).

Data Readout for Image Construction

To create an image of a radiation emitting source and get an energy spectrum of it for a given amount of time. Then the source is rotated slightly and another energy spectrum is created for the same amount of time as the first interval. The process is repeated until the object has completed one full rotation. For each angle a ROOT tree data file is created serving as the basis for the sinogram which is used for the image reconstruction. The two methods of image reconstruction are Backprojection (BP) and Filtered Backprojection (FBP).

Without getting too much into the technical details, these processes are basically assigning weighted values to the pixels that are in the path of the LOR's based on how much time a LOR spends passing over that pixel and then doing a Fourier transform of these weighted values to create an image. The rotation step width is used as an input in the rotation motor control program, and the results of the BP and FBP images are saved in an output file. The sinogram results can be analyzed with the program 'Amide' which is used for viewing, analyzing, and registering volumetric medical imaging data sets. In the final sinogram image the background radiation is eliminated. This is done by taking a reading of the background for a time 5 times longer than the coincidence window, measuring that rate and the subtracting it from the final sinogram.

Results

For channel 2 the signal begins to appear at 360 V, the signal becomes clear at 380 V. The breakdown voltage is due to the material being saturated with electrons. This appears as a cutoff of the peak. Experimentally, it was found that this occurs at around 406-408V as seen in fig. 8.

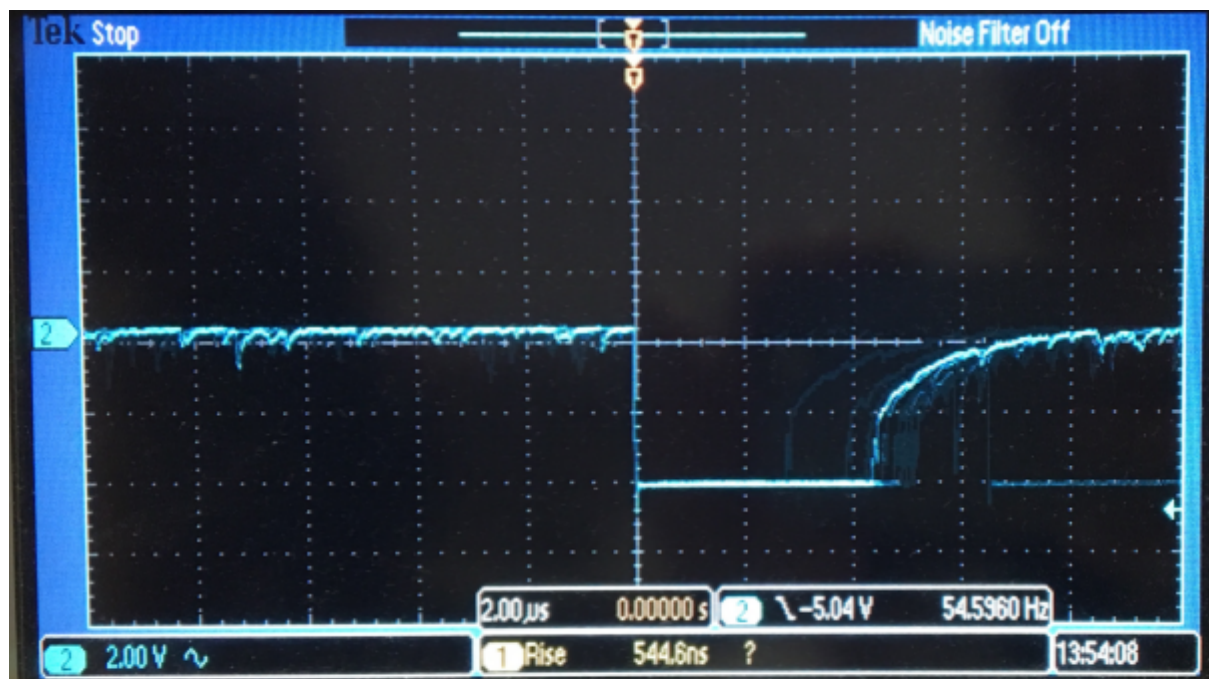


Fig. 8: Waveform at break-down voltage.

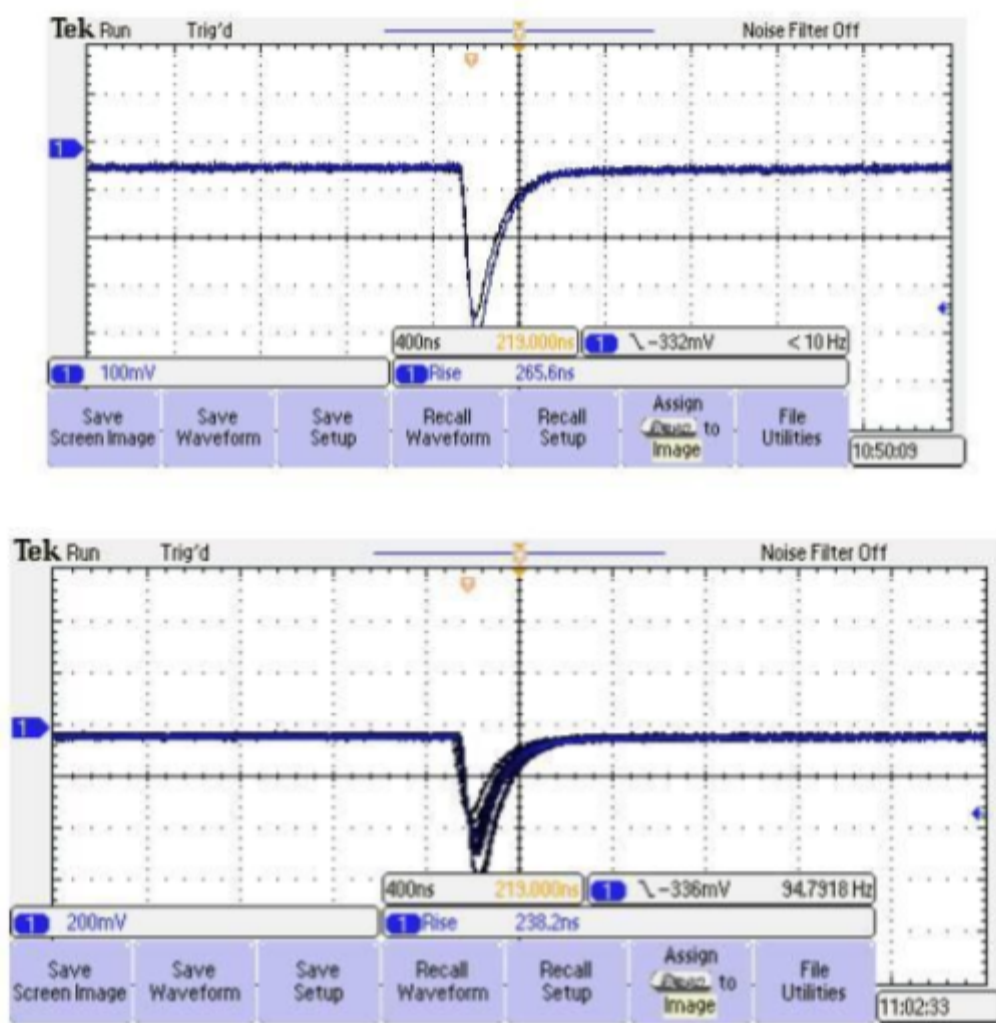


Fig. 9: At the top, the waveform without source. At the bottom, the waveform with the ^{22}Na source.

The signal response is a negative signal pulse from the ADP since we are detecting electrons with a reverse bias. Underneath the breakdown voltage there is a clear baseline (including noise) and a clear negative signal pulse, asymmetric with a vertical back. When the break-down voltage is reached the signal pulse gets a flat bottom as well as rapid fluctuations in the 'tail' and the noise in the baseline. When the radioactive source is placed in the centre of the detector ring, the rise time is slightly shorter, 238 ns versus 266 ns and there are a multitude of signals all with a significantly lower amplitude compared to at the breakage-voltage. The breakdown voltages have an amplitude of 5 V and the amplitude of the signal with the source is only 7 % of the amplitude at the breakdown. The amplitude with and without a source below 400 V are similar, only 2 mV difference, see fig. 9

The *streamusbhist* program displays in real time the number of registered coincidences per SADC. In table 1, the SADC3 has a lot lower efficiency than the other two, about 40 % less

with the source in front of them. Based on the table, having a source causes the SADC signal to be amplified vs. having no source at all (background count rate, see table. 1).

Table 1;
Energy spectra of SADC data with and without a source (events/s).

	SADC 1 (events/s)	SADC 2 (events/s)	SADC 3 (events/s)
Without source	30	30	20
With source	500	500	300

The highest peak on the left side in fig. 10 is the corresponding 511 keV energy peak from the coincidence detection. The small peak at the left end is due to the compton scattering in the detector and the small response on the right side is from the 1 022 keV energy from the gamma photons produced when the daughter nuclide de-excites to a stable state by emission of a gamma photon with the characteristic energy of the energy difference of the two states. The resolution is approximated from the FWHM, we can calculate this by multiplying the equation for the resolution by 2.35 to get:

$$\frac{\Delta E}{E_{FWHM}} \approx 2.35 \frac{\sigma_F}{\mu_F} \cdot 100 \approx 15.6 \%$$

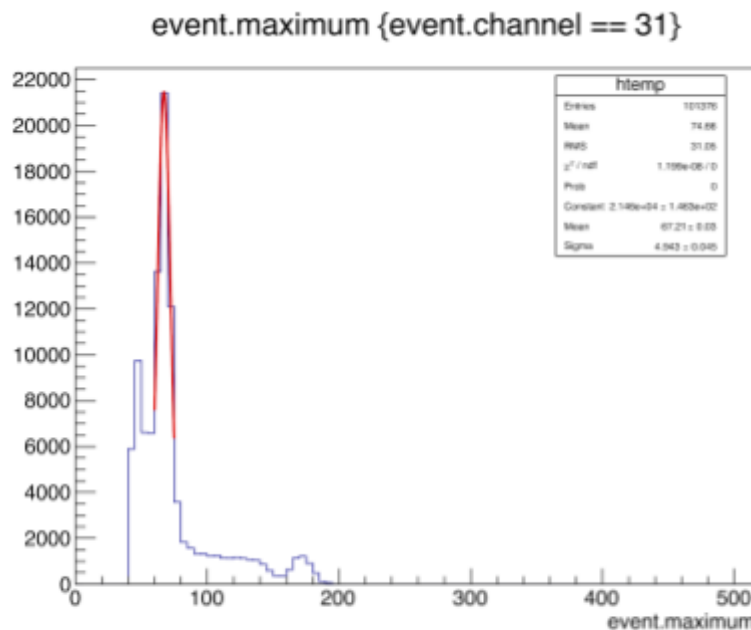


Fig. 10: Gaussian fitted histogram for readout-channel 31. The fit has a mean around 67 and a standard deviation of 4.9 AU.

Fig. 11 is the superimposed bin location of the 511 keV energy peak for all channels, the spectrum for each readout channel is included as an appendix. This figure gives an overview of the spread of the location of the peak as well as the intensity difference for each readout channel and which ones that are not functioning properly, in this instance channel 36 and 47.

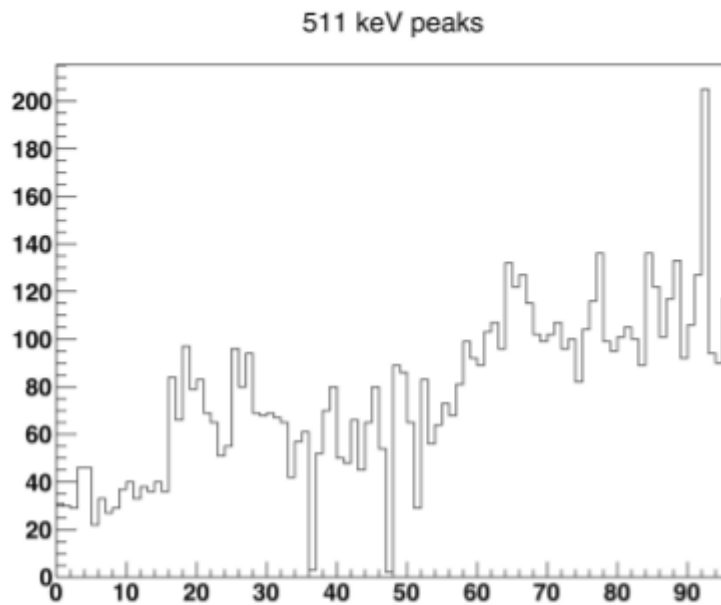


Fig. 11: The location of the 511 keV energy peak in each readout channel.

When the bias voltage is lowered the mean also moves to the left, its value also decreases, see table 2 for channel 2. A linear fit can be performed for the data points as shown in fig. 12.

Table 2:

Voltage and mean values for seven different data sets. Plotted in fig. 12.

Ch 2	Data 1	Data 2	Data 3	Data 4	Data 5	Data 6	Data 7
Voltage (V)	290.0	289.5	289.0	288.5	288.0	287.5	287.0
mean	29	27	27	26	26	25	24

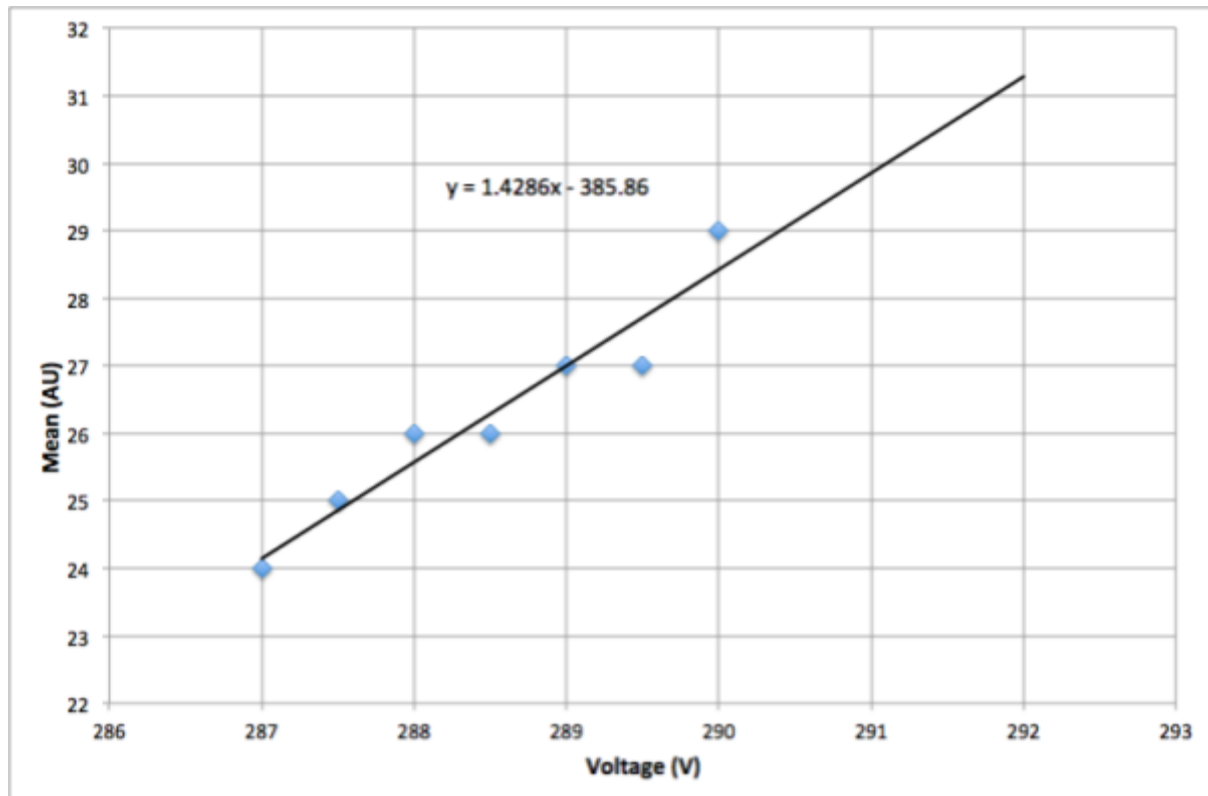


Fig. 12: A linear fit to the data from table 2 of the mean photopeak value vs. voltage for channel 2.

The FWHM of the timing calibration before iteration is around 7.4 ns and after three iterations is 4.9 ns, that is, it has decreased by 30 %. The window size should match the FWHM, therefore with a maximum value of ± 10 ns, as seen in fig. 13. To successfully perform time of flight measurements, the delay of the signal from the scintillator and the electronics need to be compensated for since the difference in the time of arrival is also used to calculate the spatial location of the event. In this set-up the LSO (Lutetium Orthosilicate) crystals have both the fast timing and high light output necessary for TOF calculations. The APD should also not be a problem with its 75 % quantum efficiency as long as the cable length is accounted for. It is possible that other reconstructive method could yield better reconstructed images, such as an iterative method although it requires more computational powers.

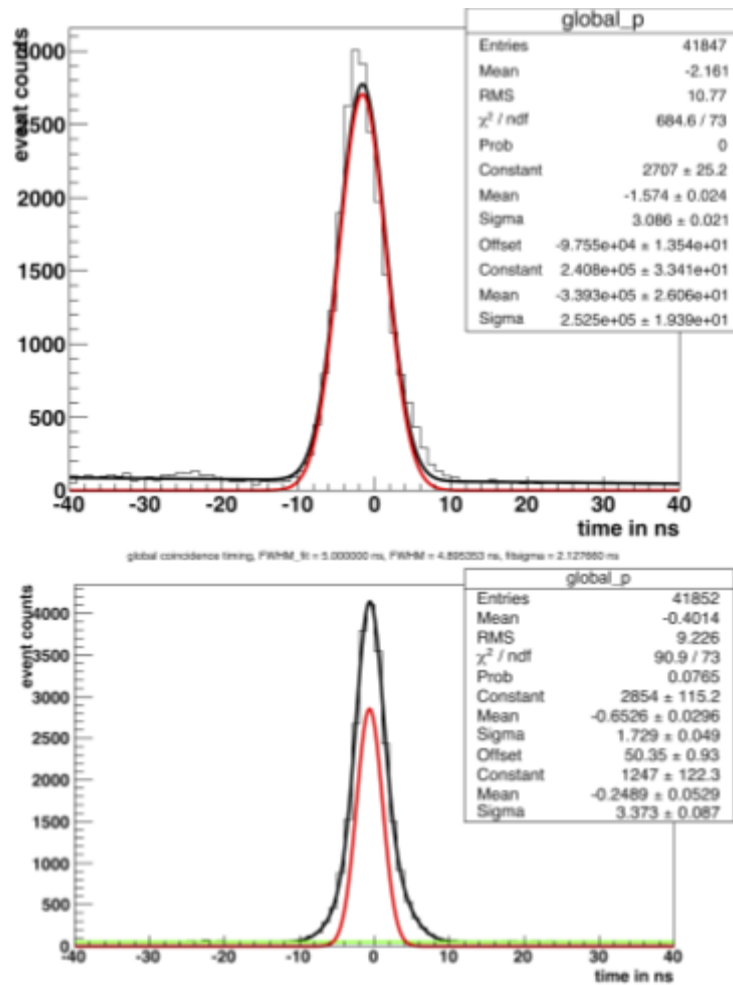


Fig. 13: Two iterations of the timing calibration. At the top is the first calibration, at the bottom is after three iterations.

It should be noted that due to a faulty accelerator there was no FDG tracer available for imaging of the plexiglass structure. Previous results of reconstructed images were supplied for this part of the analysis.

The black lines in the sinogram in fig. 14 are from lack of projection data. The more angles covered in the data collection, the fewer and narrower the lines becomes. For optimal reconstruction the data should be collected at each half or one degree interval, also, the result would improve with more detectors.

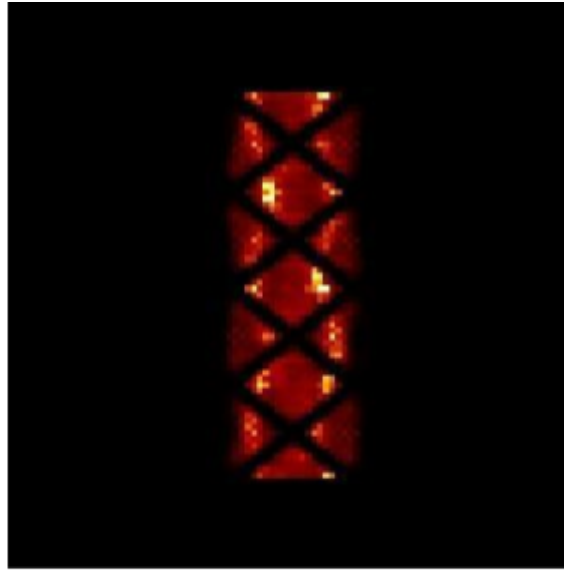


Fig. 14: Sinogram of the star-shaped plexiglas taken at 45° angle intervals. The black lines corresponds to lack of collected data for reconstruction.

The filtered back-projection includes the application of a weighted high-pass filter in the frequency domain, such as a ramp-filter. This yields more weight to the higher frequency and suppresses low frequencies which contributes to the noise in the reconstructed image. Further noise reduction can be performed by normalizing the data against a mean value or background value, leading to less of a graininess in the image as seen in fig. 15.

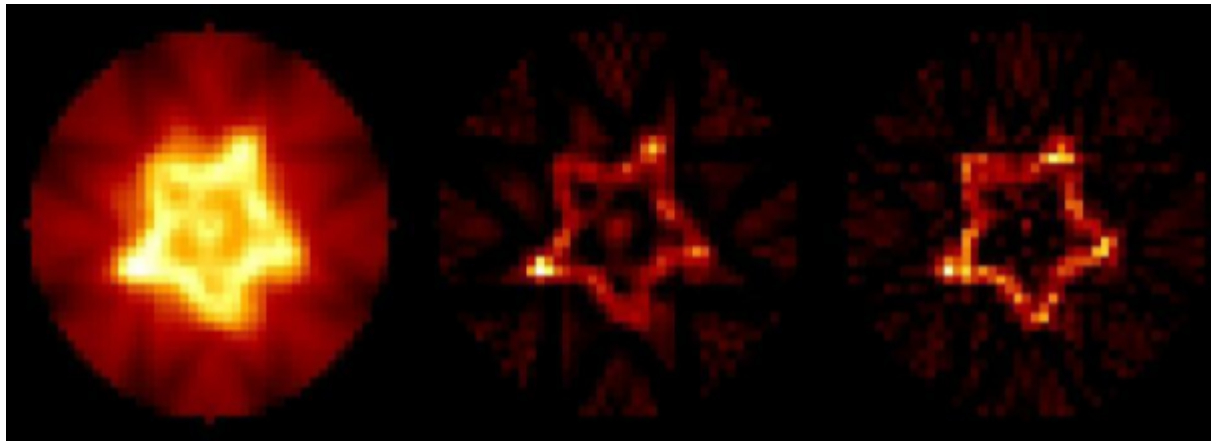


Fig. 15: The PET scans of star shaped plexiglass sources with FDG. The leftmost image is normal BP and the middle is filtered back projection (FBP) with a ramp-filter. The rightmost is the the same as the middle but with normalized data.

For the skyscraper plexiglas source in fig. 16 the resolution for the different reconstruction methods can be estimated by observing which lines can be distinguished in the reconstructed images and calculate the physical distance from the schematics. With simple subtraction of the width of the milling from the given dimensions, the resolution can be

approximated. For the normal BP the base of the middle skyscraper can be distinguished, which corresponds to 8.75 mm. For the FBP the top of the middle skyscraper can be clearly seen with the width of 5.00 mm. Lastly, in the normalised FBP the base of the right skyscraper with a width of 4.75 mm. With improved noise suppression the resolution improves.

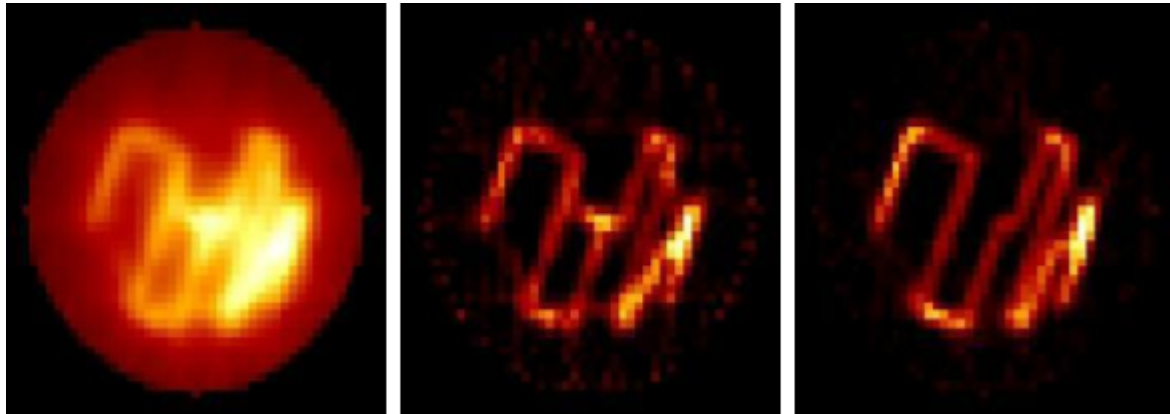


Fig. 16: The PET scans of star shaped plexiglass sources with FDG. The leftmost image is normal BP and the middle is filtered back projection (FBP) with a ramp-filter. The rightmost is the the same as the middle but with normalized data.

Conclusion

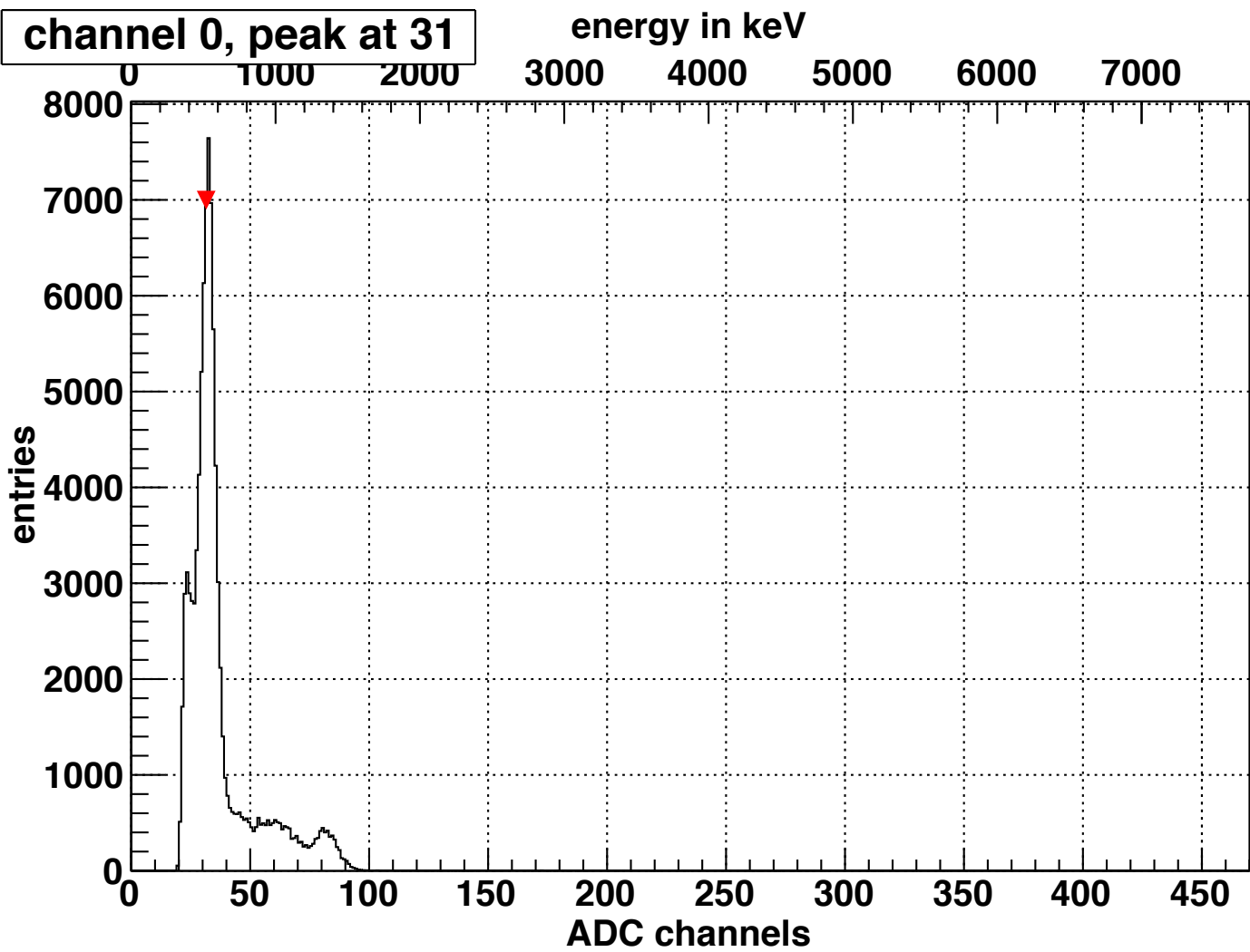
The observed breakdown voltage occurred around 407 V. Adding a source creates a multitude of signals with slightly different amplitudes. It was determined that the energy resolution of the detector system had a resolution of slightly higher than 15 % which is considered a good value according to modern day clinical PET, other semiconductor materials such as CZT produce higher resolution but has a higher monetary cost. In each of the readout channel histograms of energy the highest peak was the 511 keV gamma ray but other processes were also detected, such as Compton scattering and the the gamma photon due to the de-excitation of the daughter nuclei of the Na decay process. Two of the ninety six detectors were dysfunctional as can be seen in fig. 11. Lowering the bias voltage lowered the mean channel value as seen if fig. 12. The coincidence window which is the timing window for two events to be considered due to the same process is was improved from 7.4 ns down to 4.9 ns by doing three iterations.

In the analysis of the imaged sinogram depicts the connection between image accuracy and the angular intervals for which data is collected. For example, doing only eight sets of data, corresponding to relatively large 45° intervals creates an image with black lines which are unrevealing and undesirable, therefore smaller intervals provide a more complete image. Adding more detectors to the ring, effectively filling in the gaps between them is another way of yielding more complete images. Applying a filter before reconstruction improves the

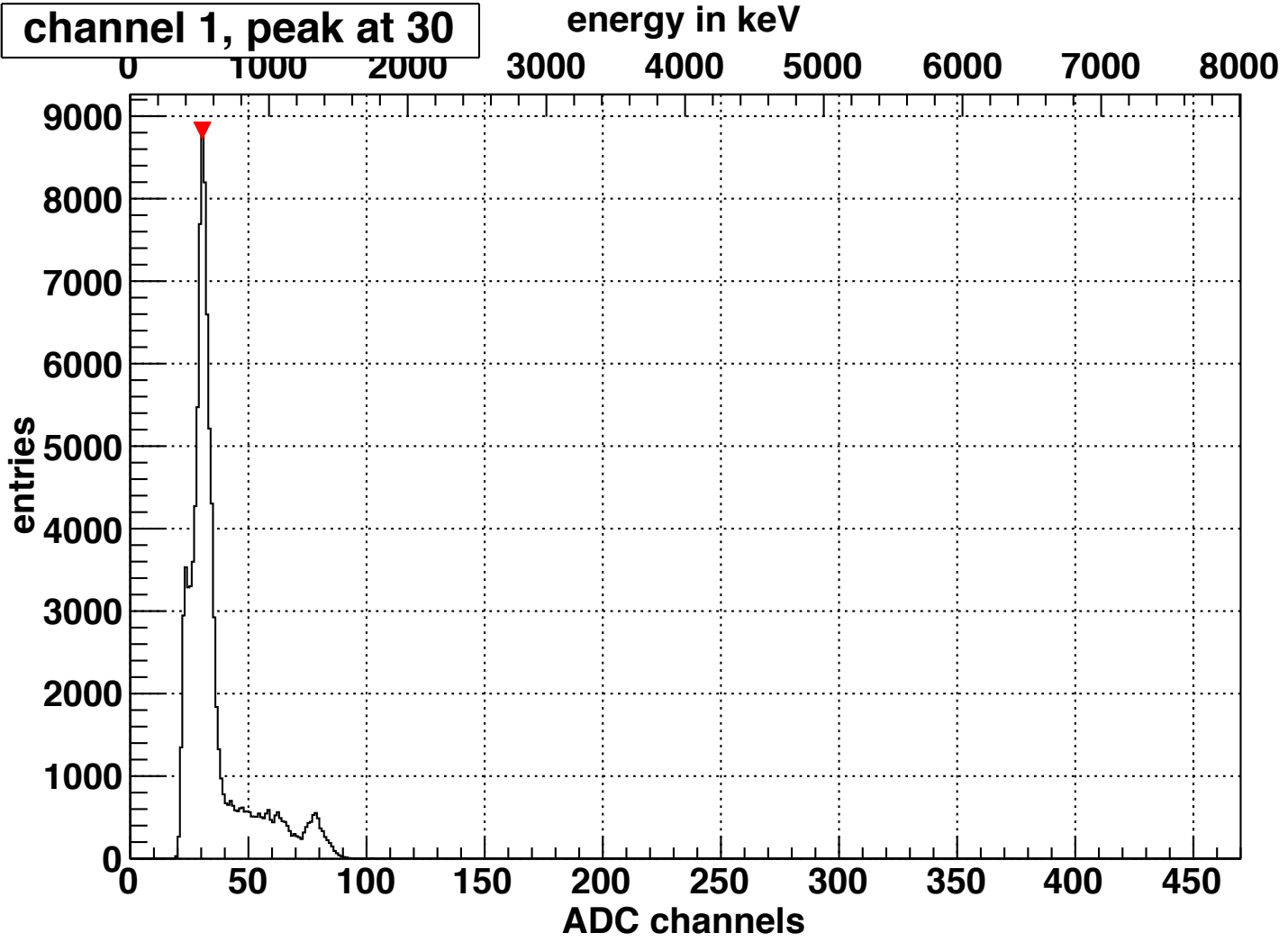
reconstructed image. The image can be further improved by normalizing the data. The best achieved resolution was around 4.75 mm with the normalised FBP.

Appendix

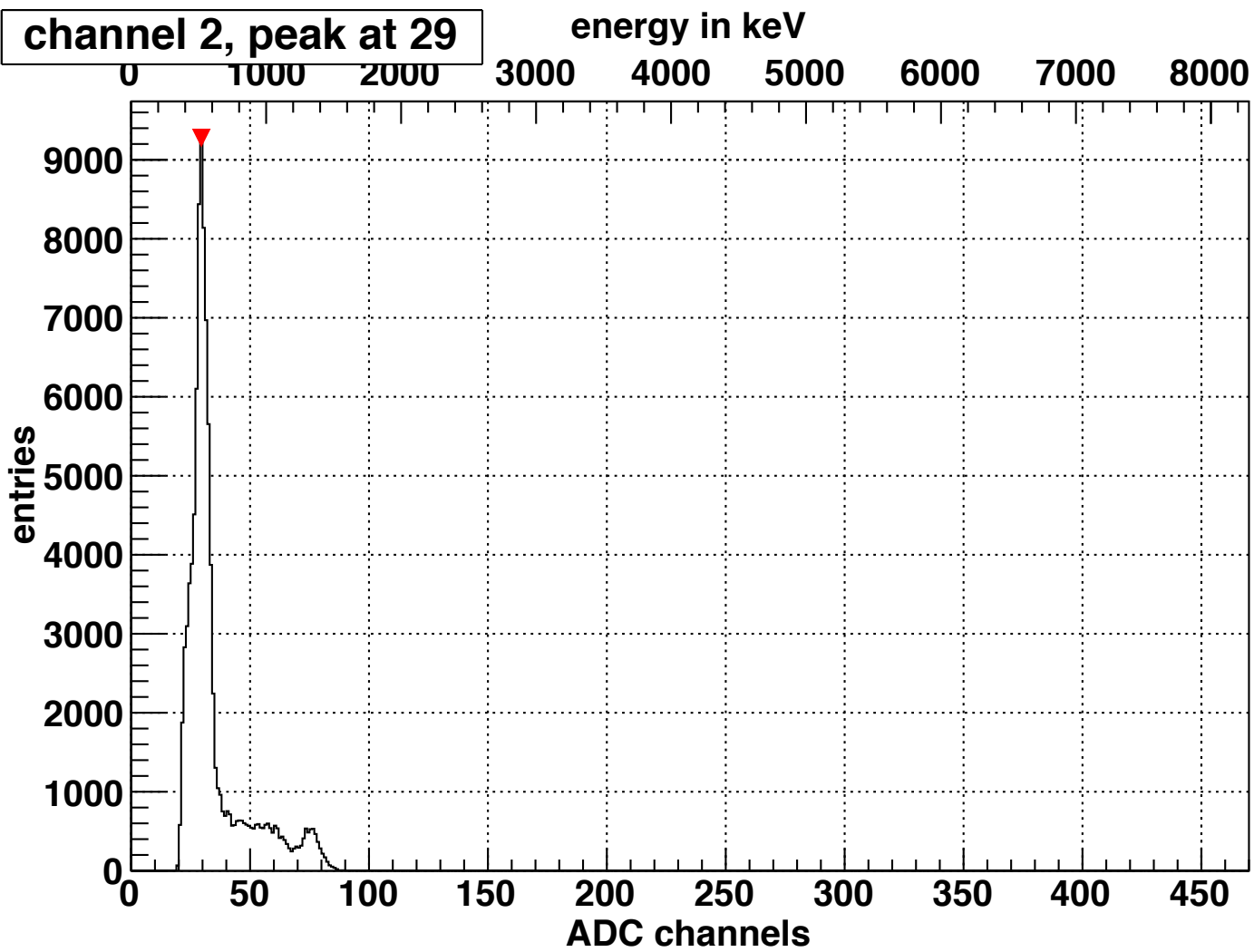
channel 0, peak at 31



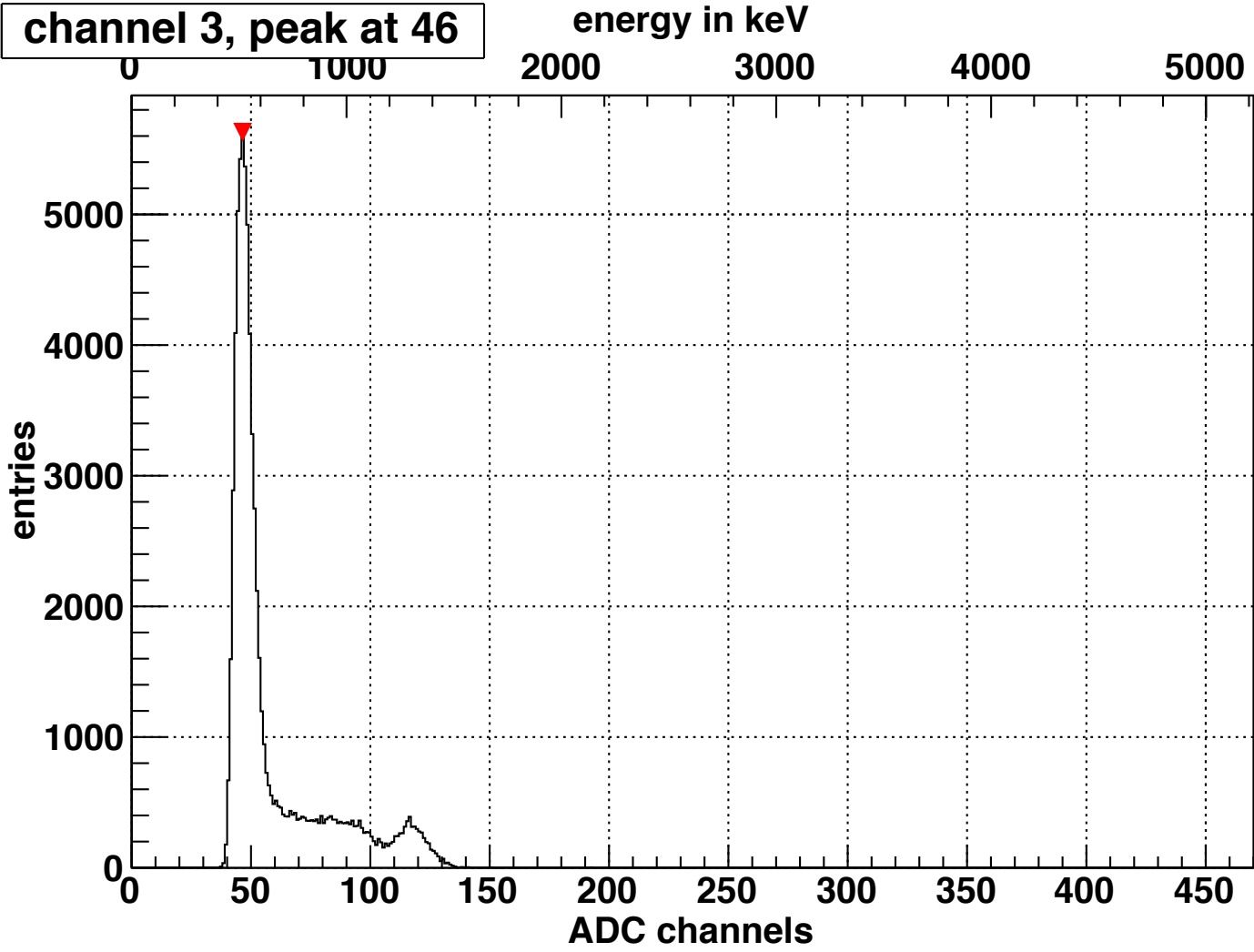
channel 1, peak at 30



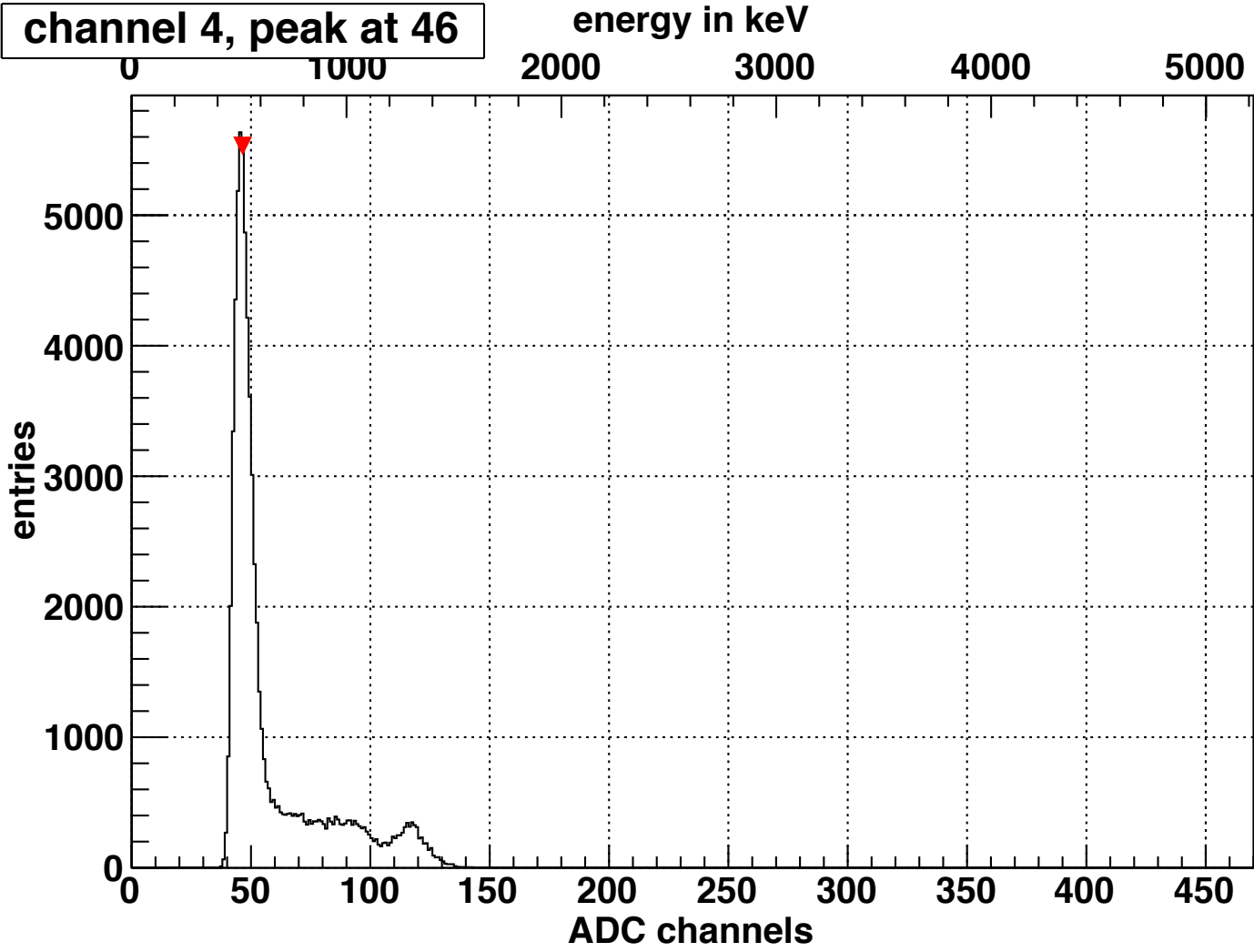
channel 2, peak at 29



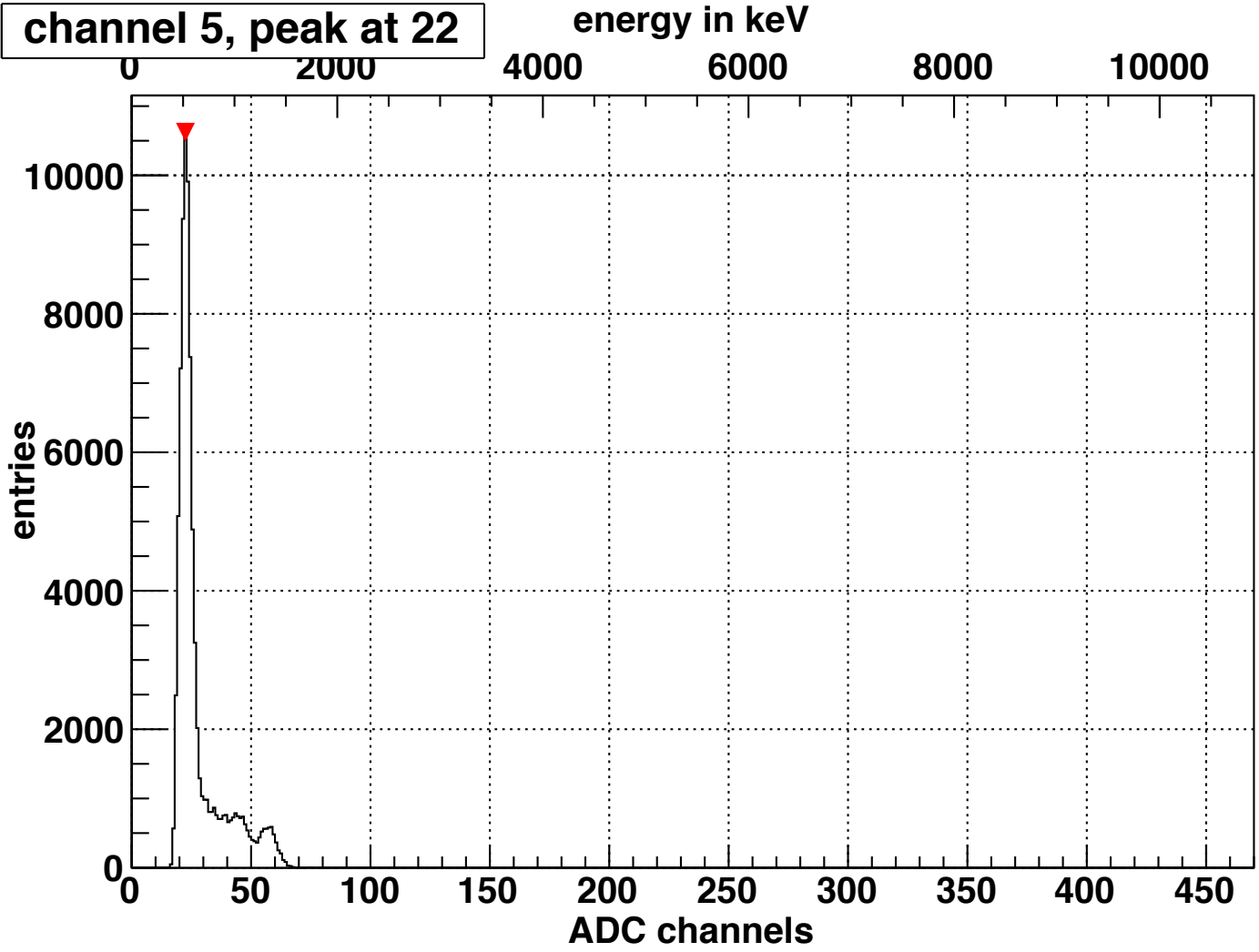
channel 3, peak at 46



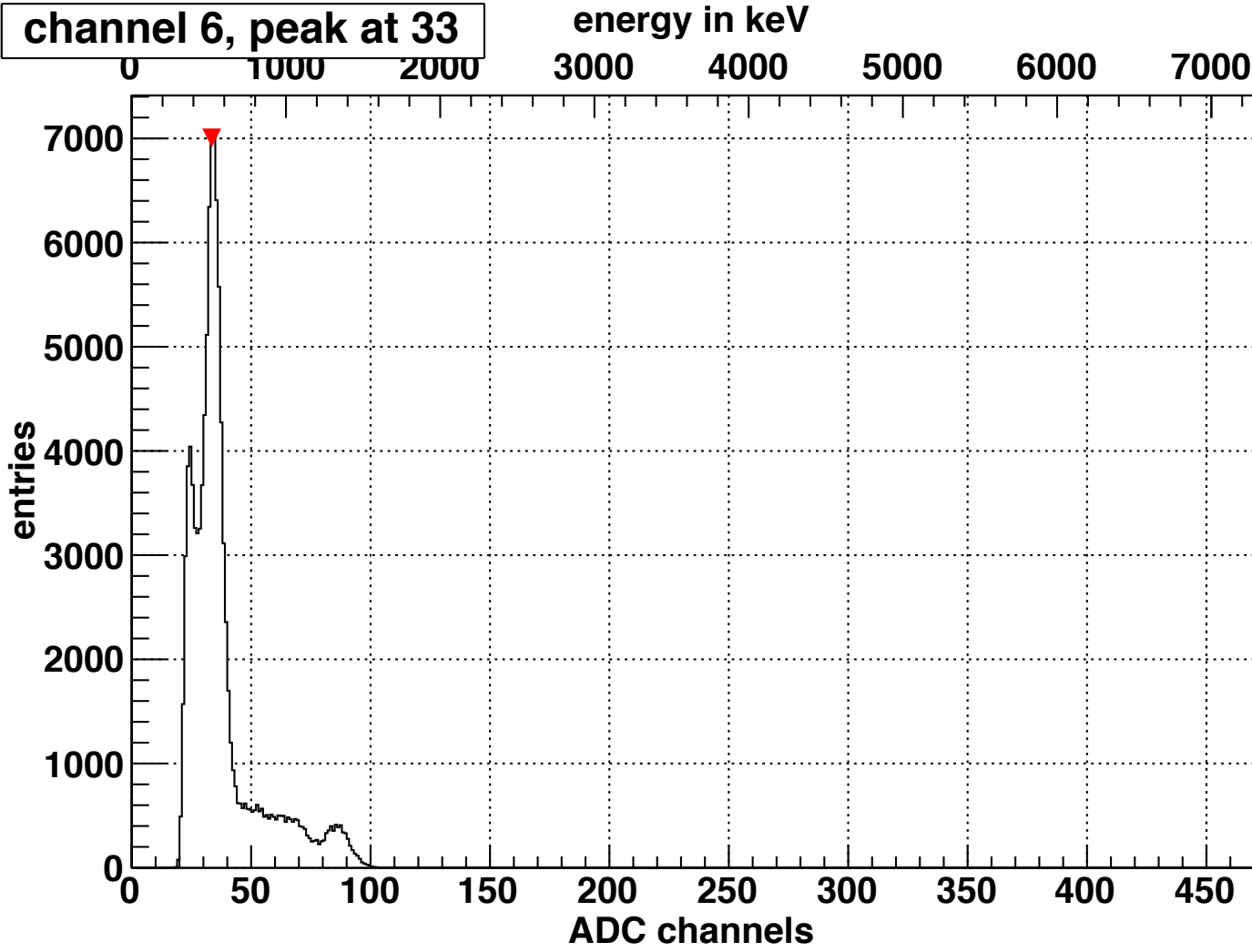
channel 4, peak at 46



channel 5, peak at 22

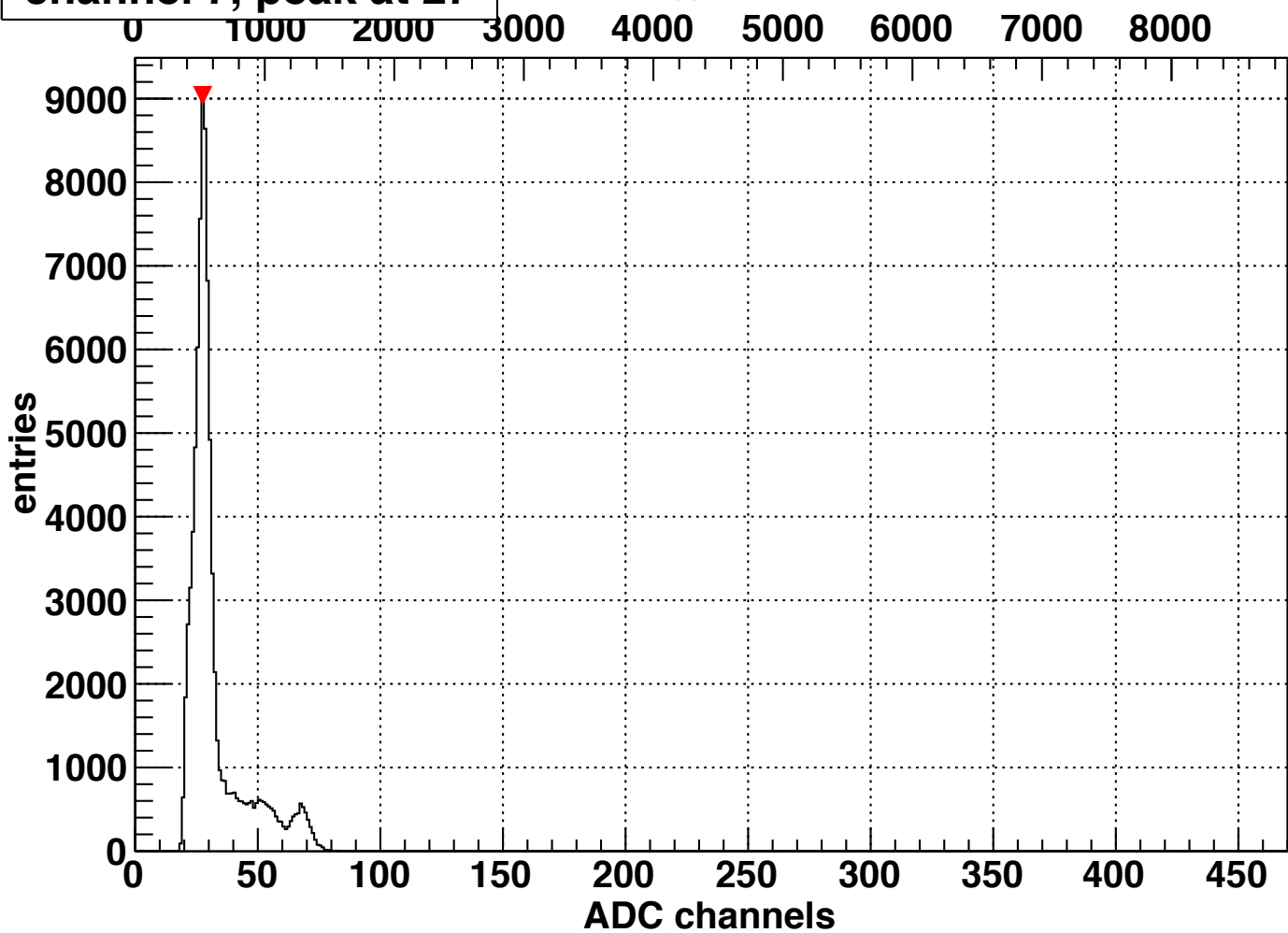


channel 6, peak at 33

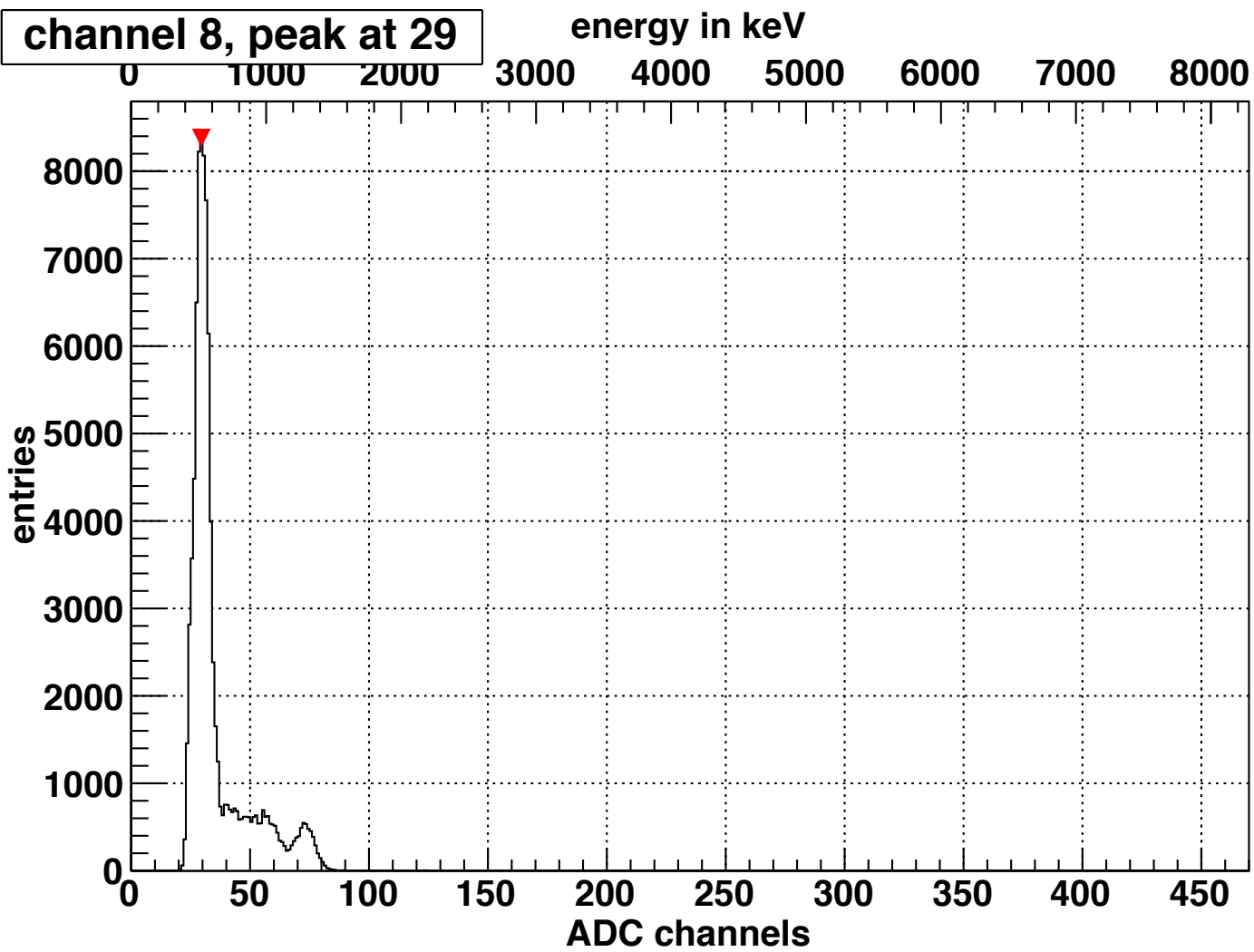


channel 7, peak at 27

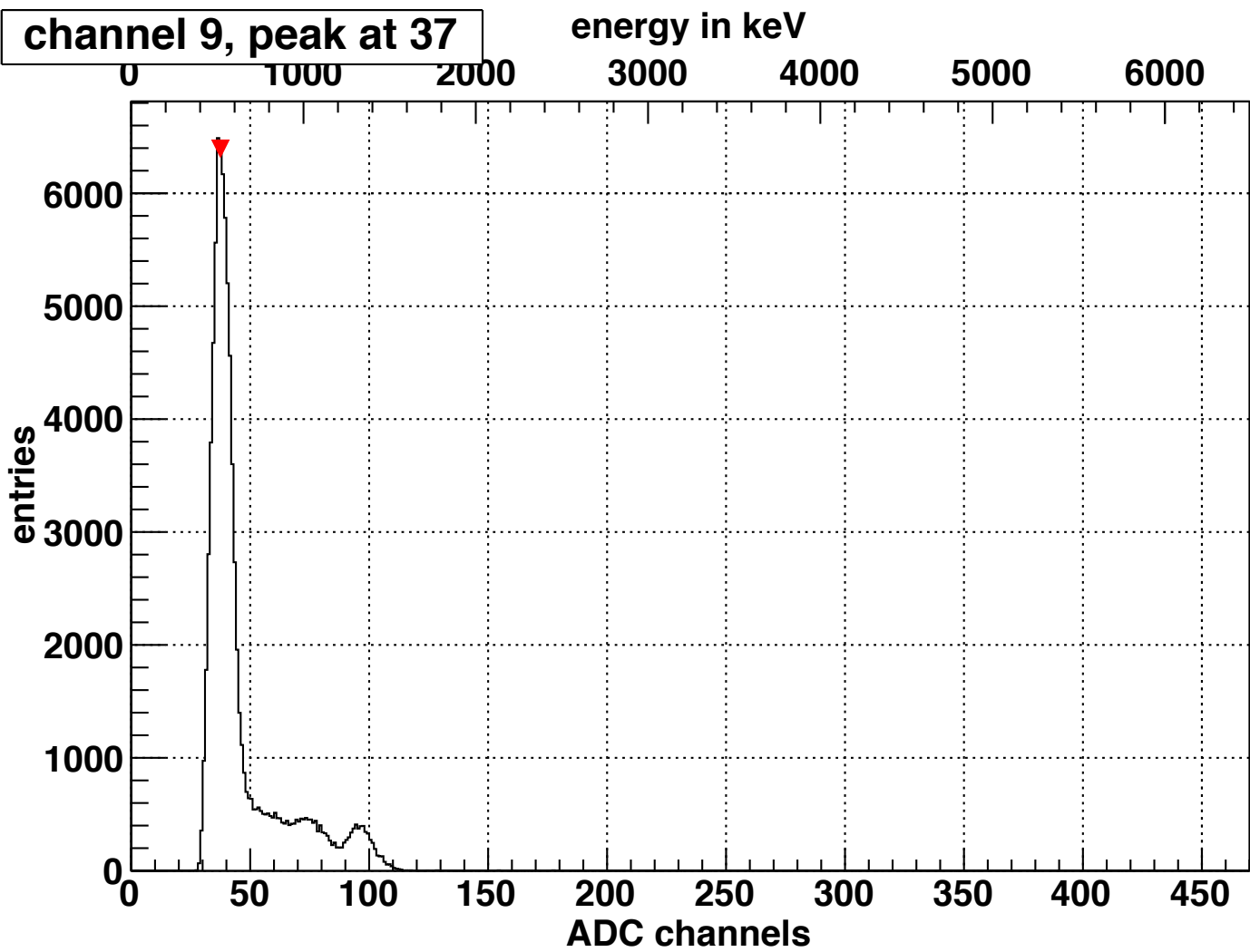
energy in keV



channel 8, peak at 29

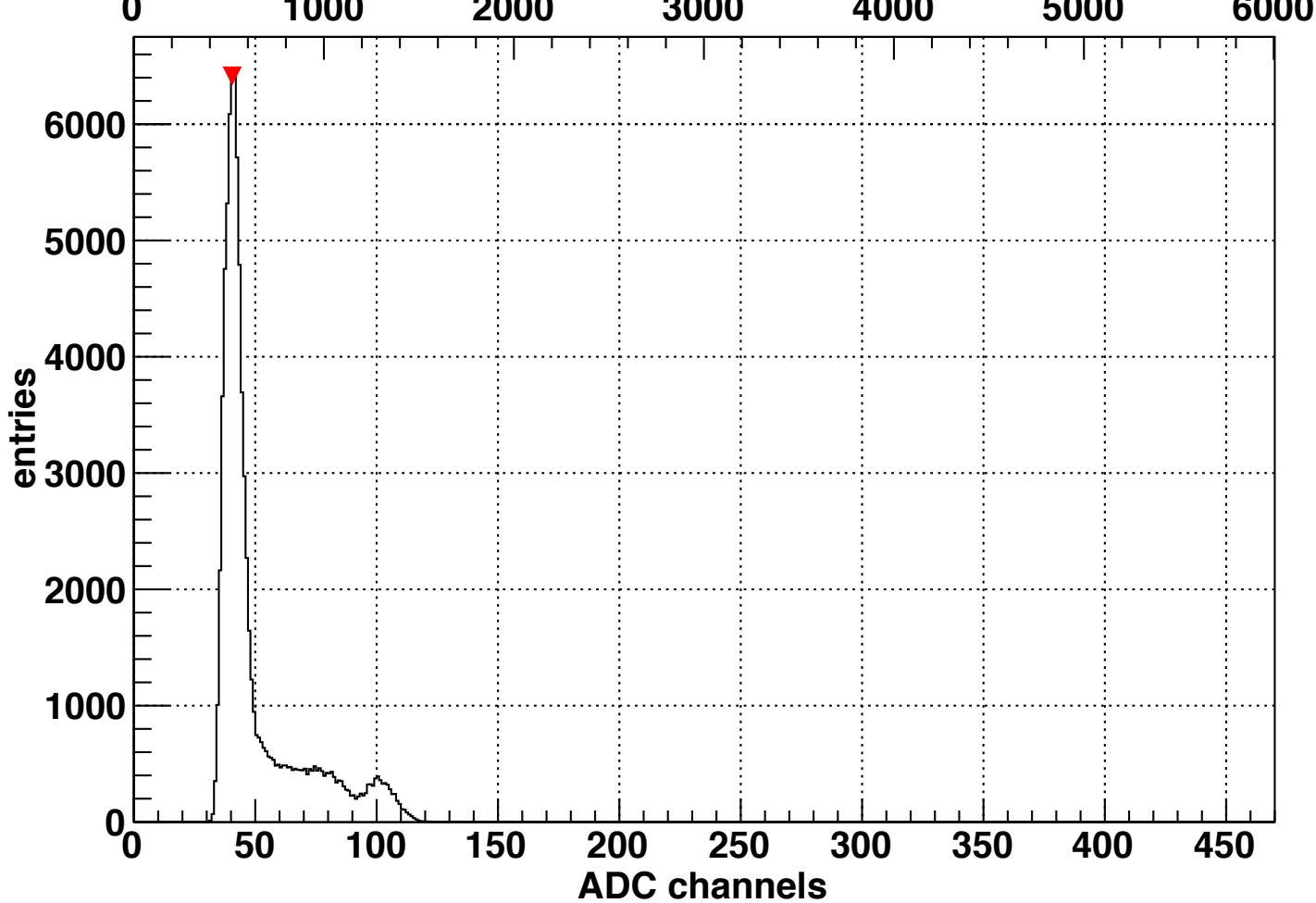


channel 9, peak at 37

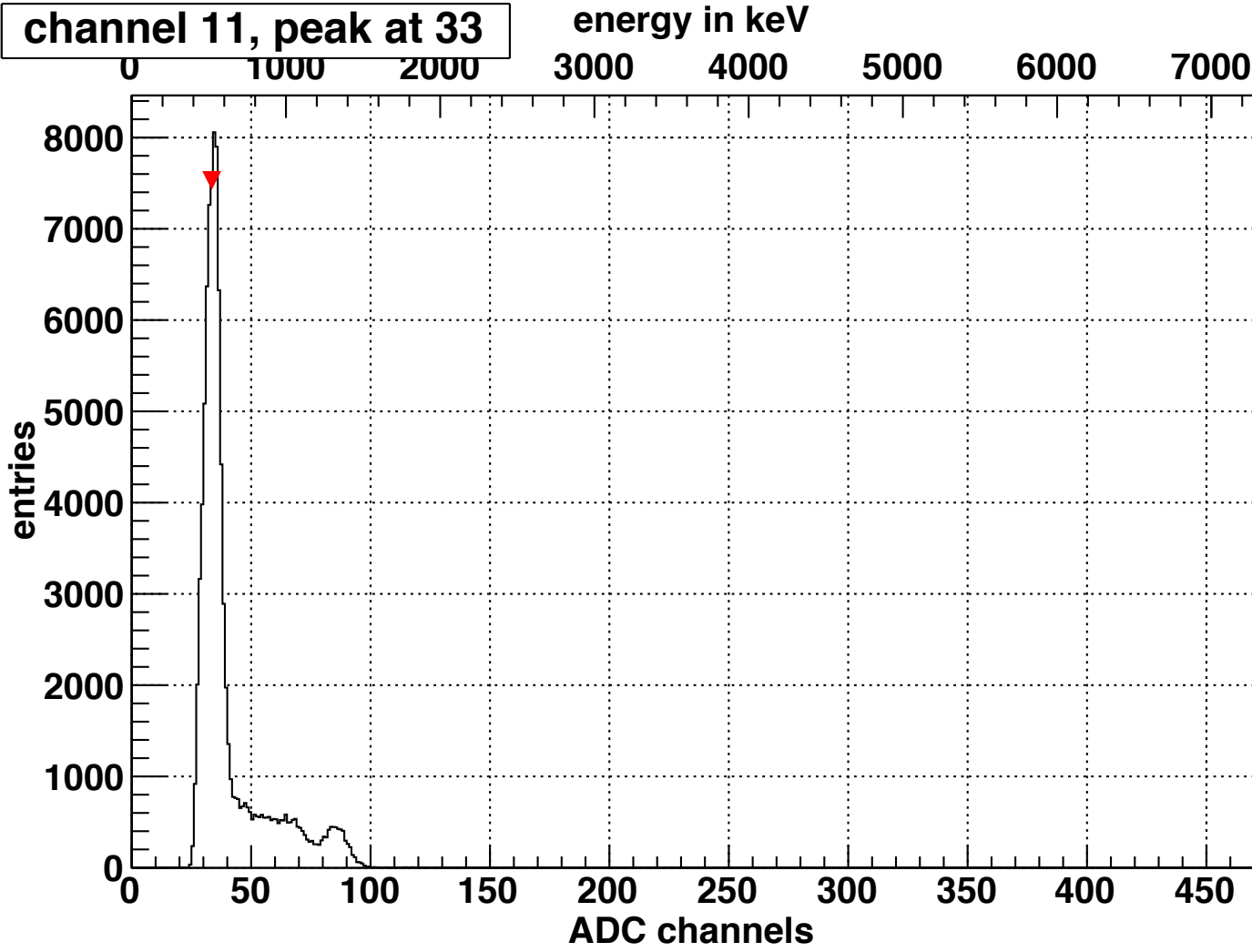


channel 10, peak at 40

energy in keV

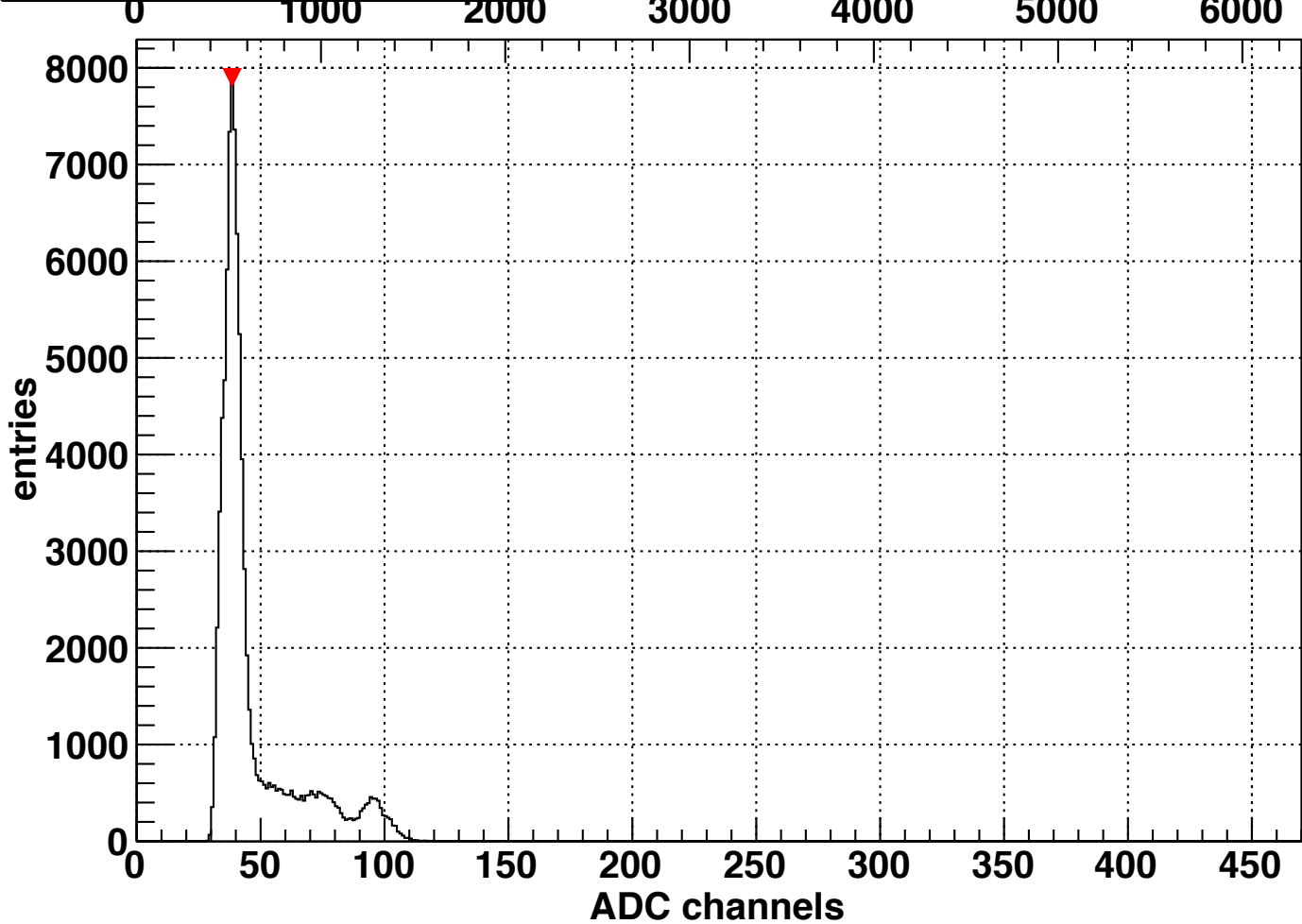


channel 11, peak at 33



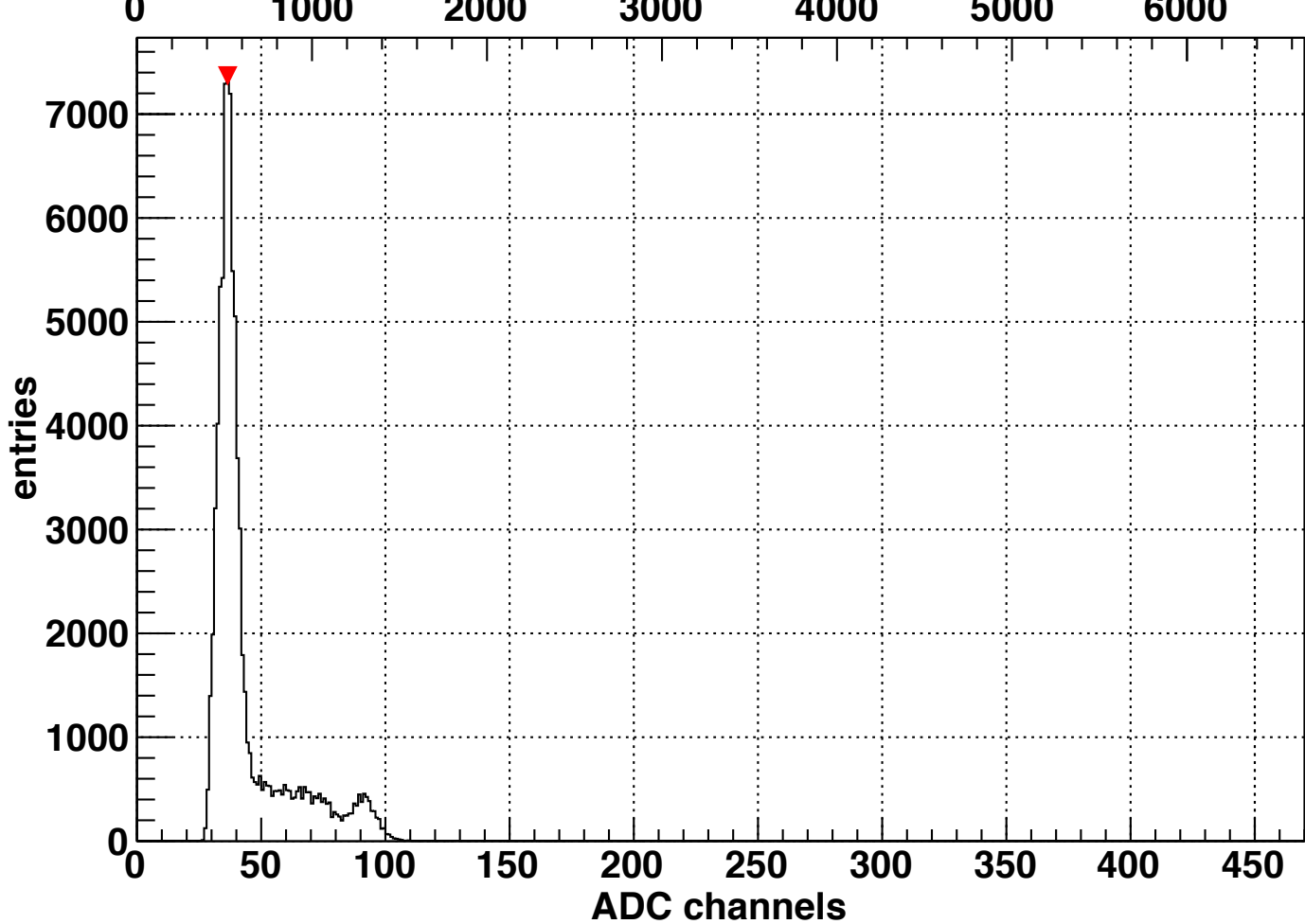
channel 12, peak at 38

energy in keV



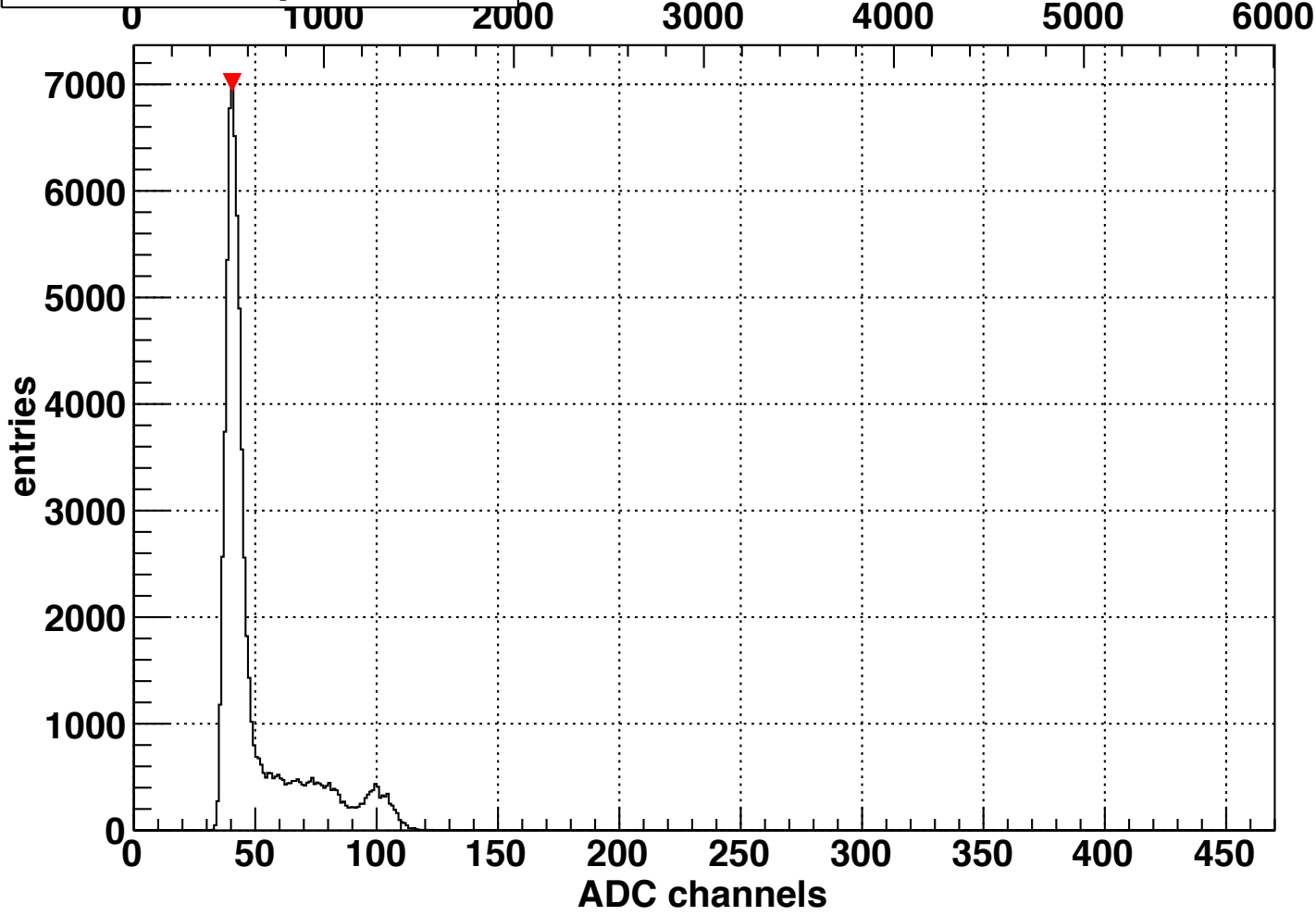
channel 13, peak at 36

energy in keV



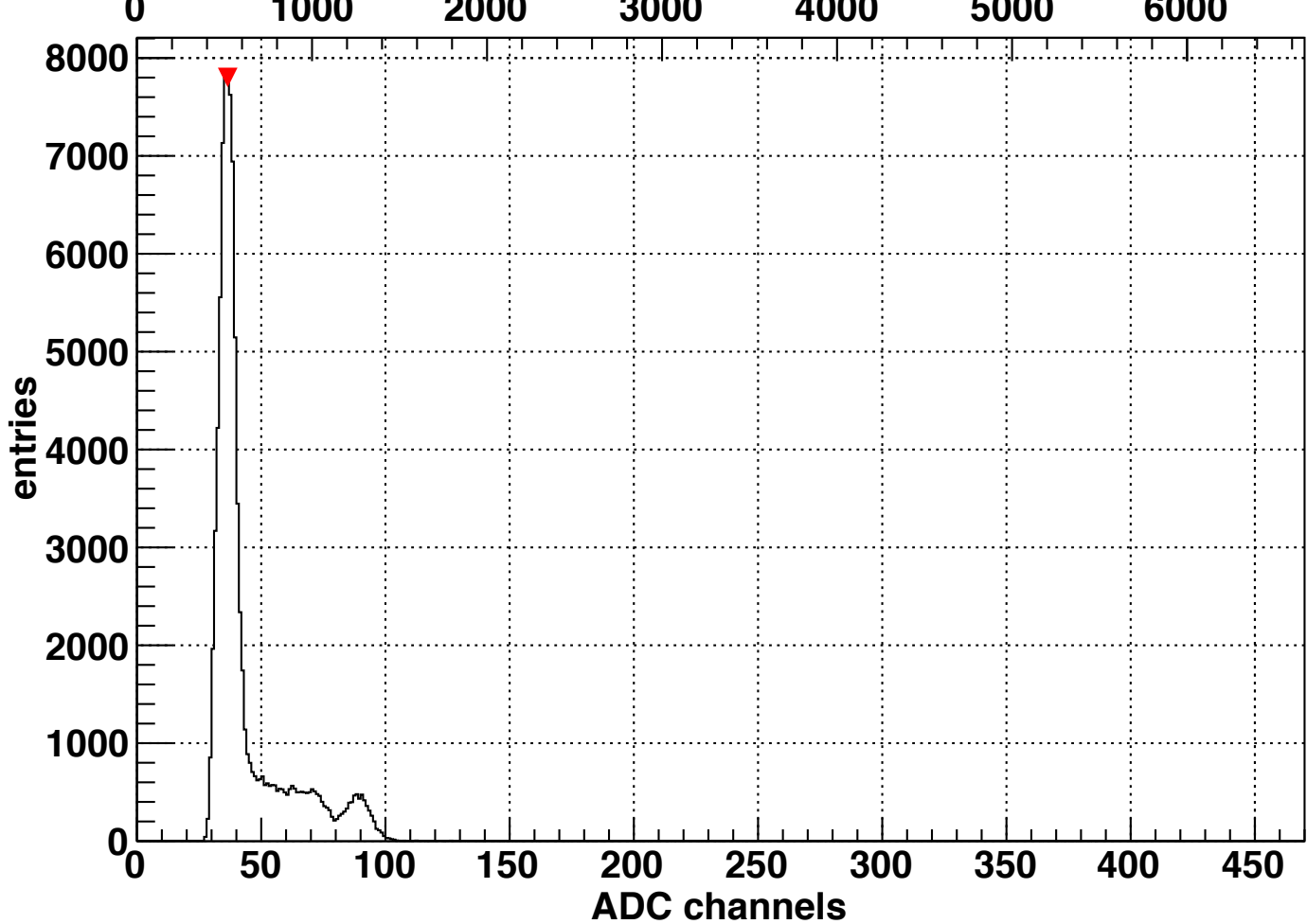
channel 14, peak at 40

energy in keV



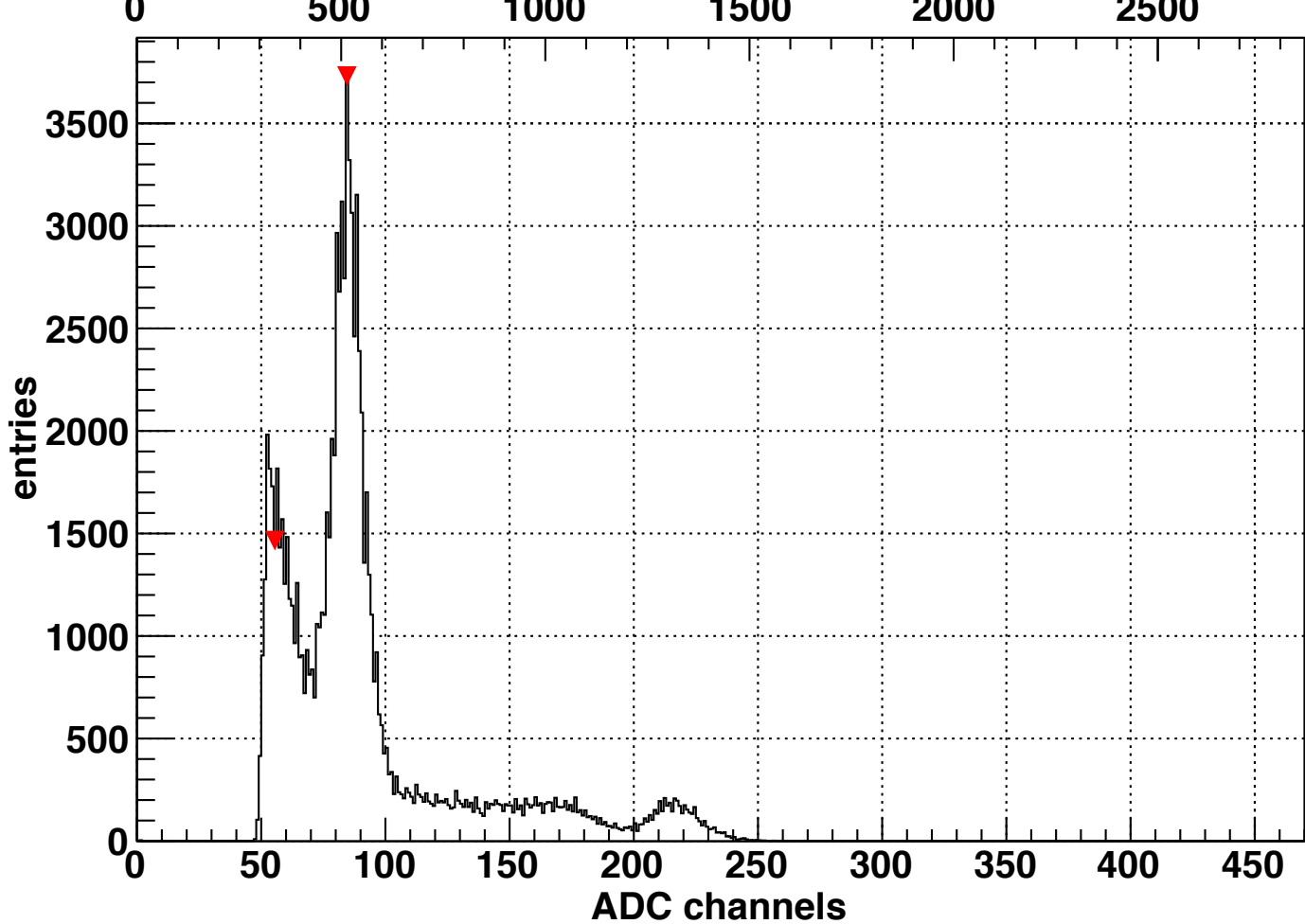
channel 15, peak at 36

energy in keV



channel 16, peak at 84

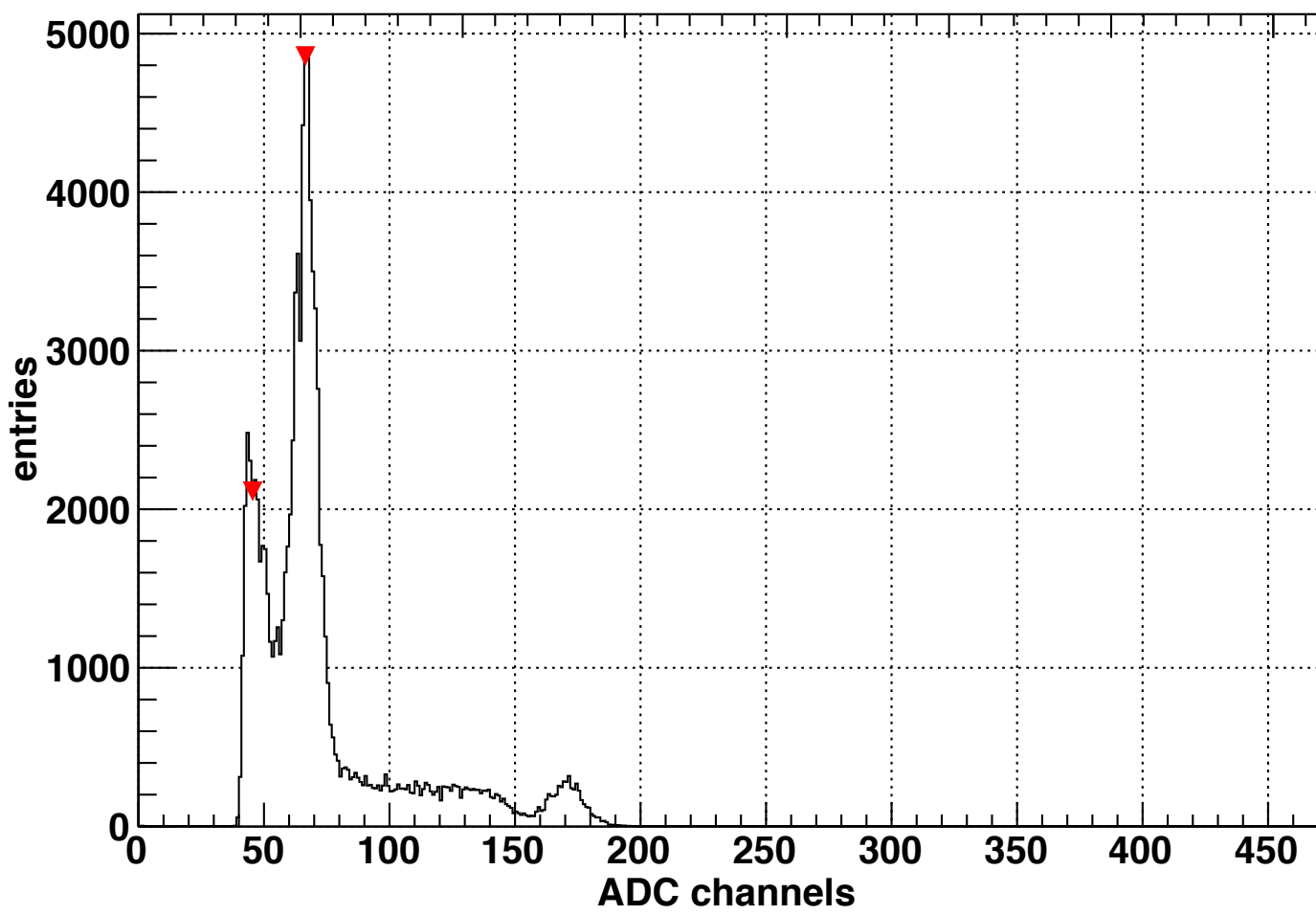
energy in keV



channel 17, peak at 66

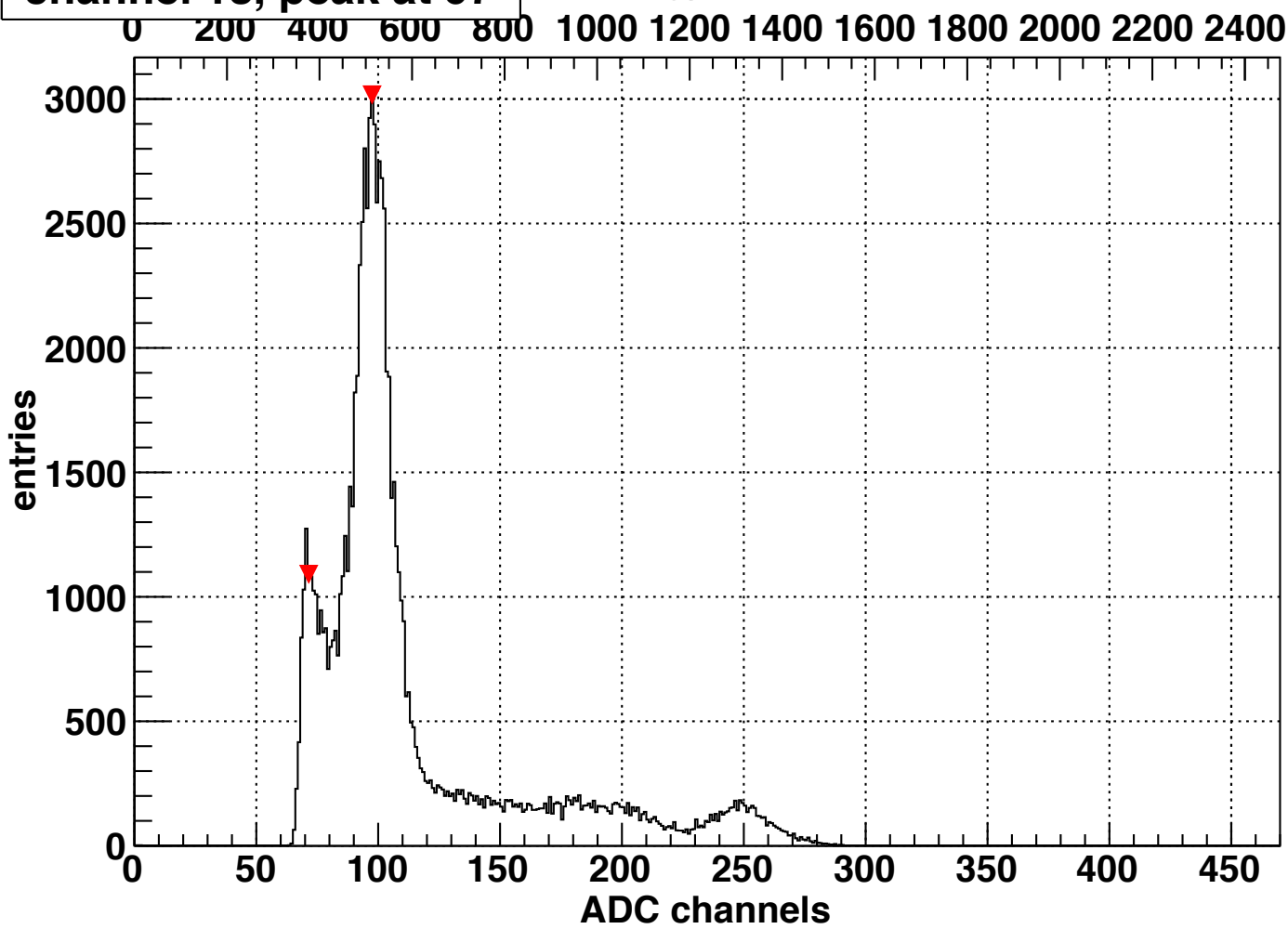
energy in keV

0 500 1000 1500 2000 2500 3000 3500



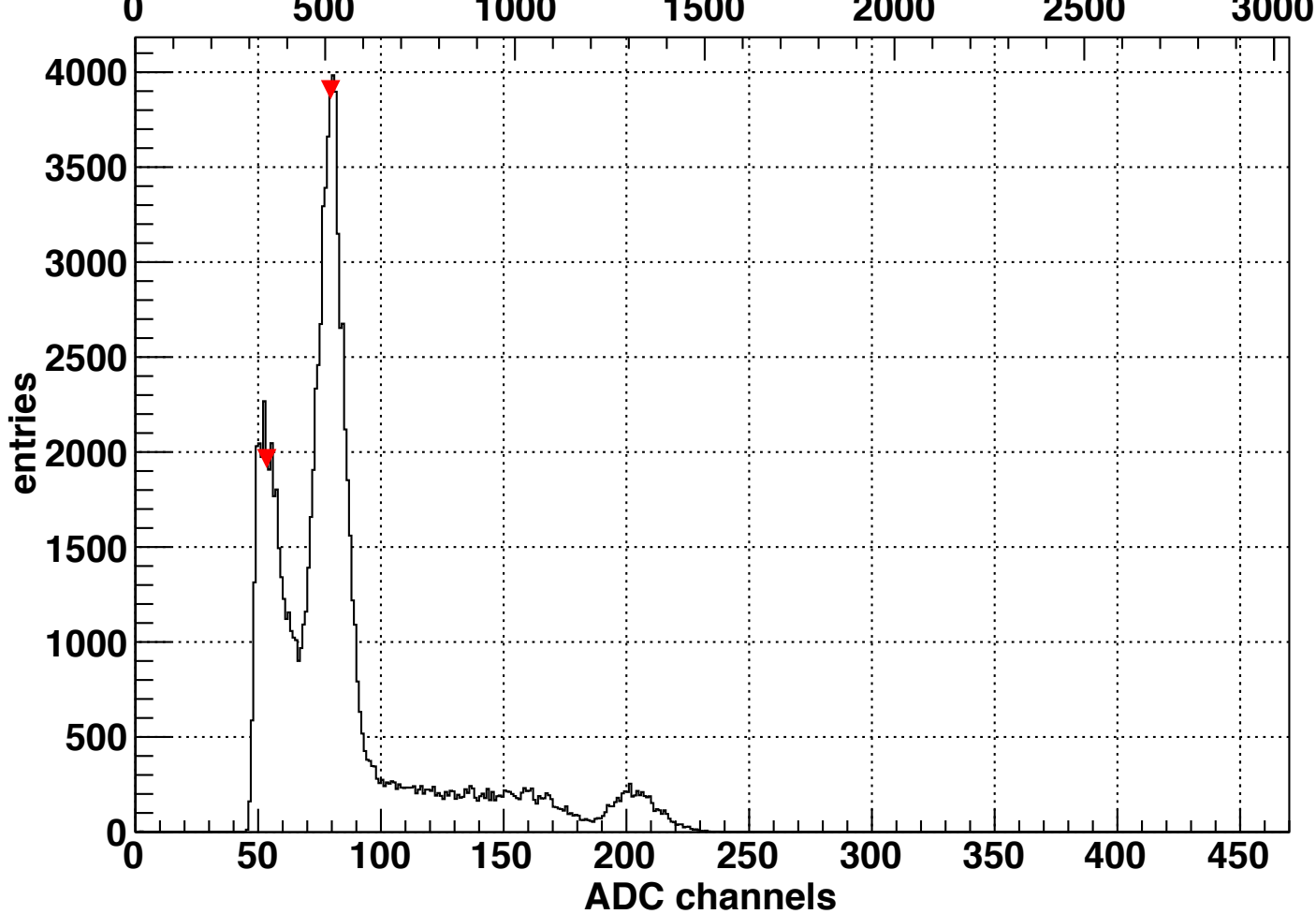
channel 18, peak at 97

energy in keV



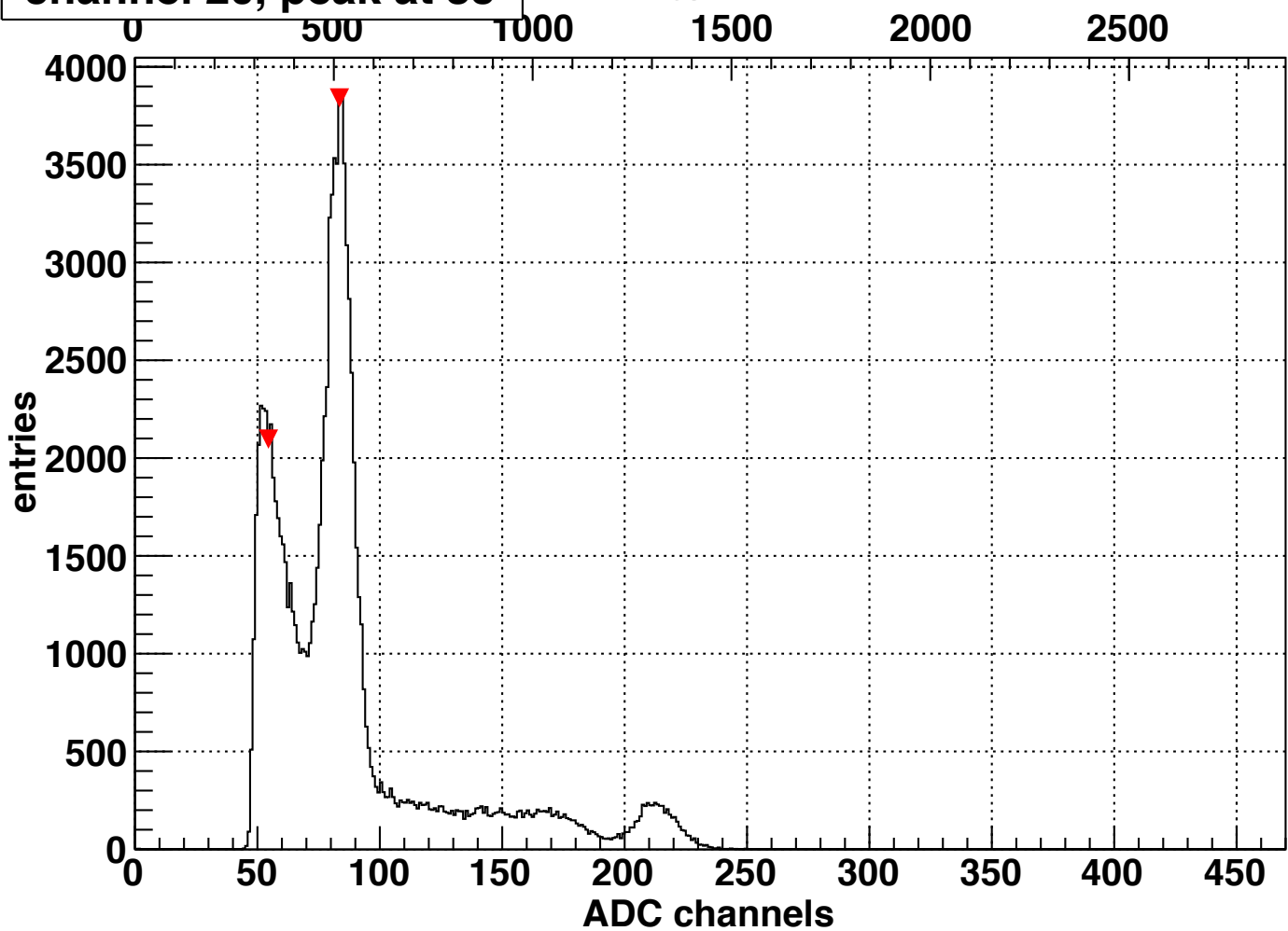
channel 19, peak at 79

energy in keV



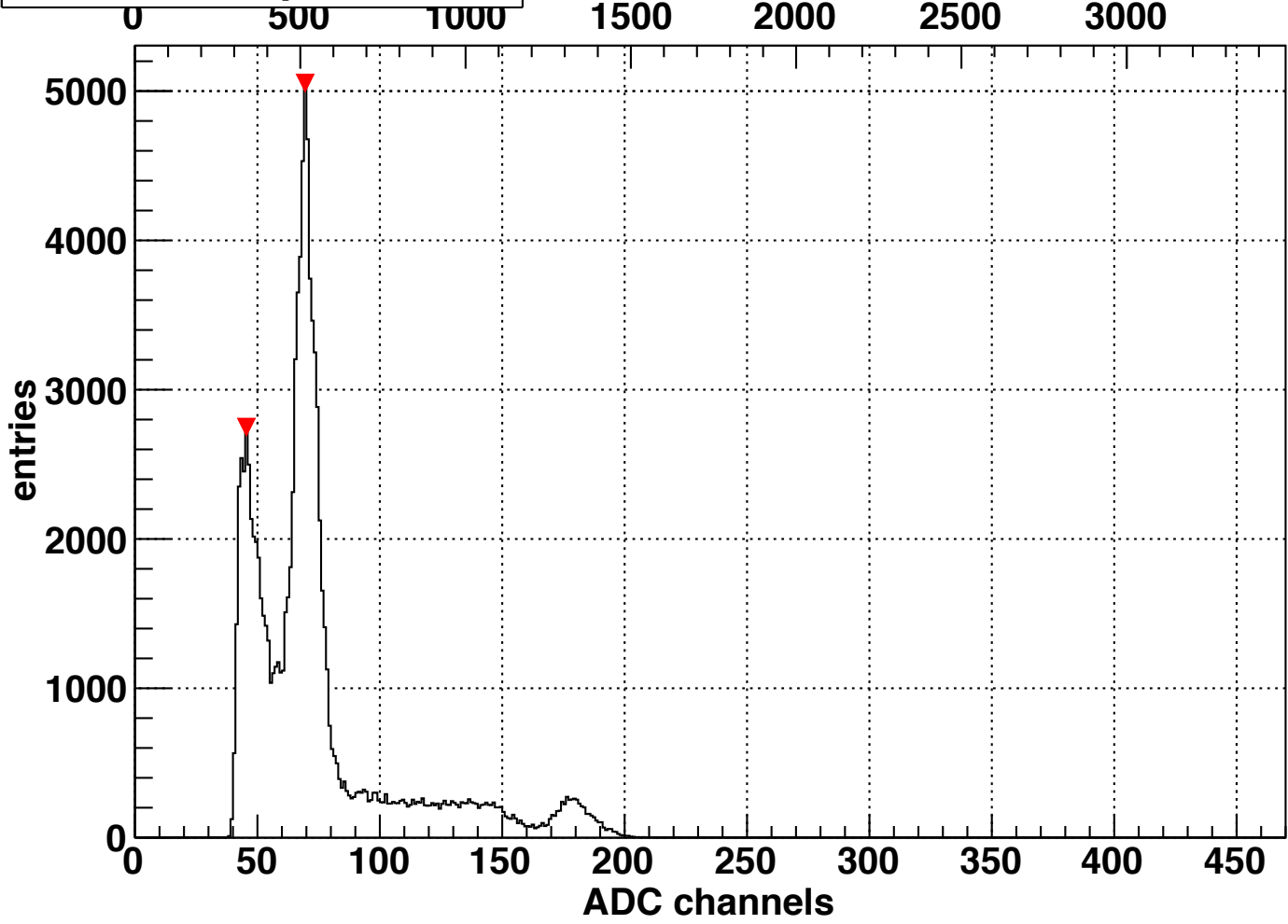
channel 20, peak at 83

energy in keV

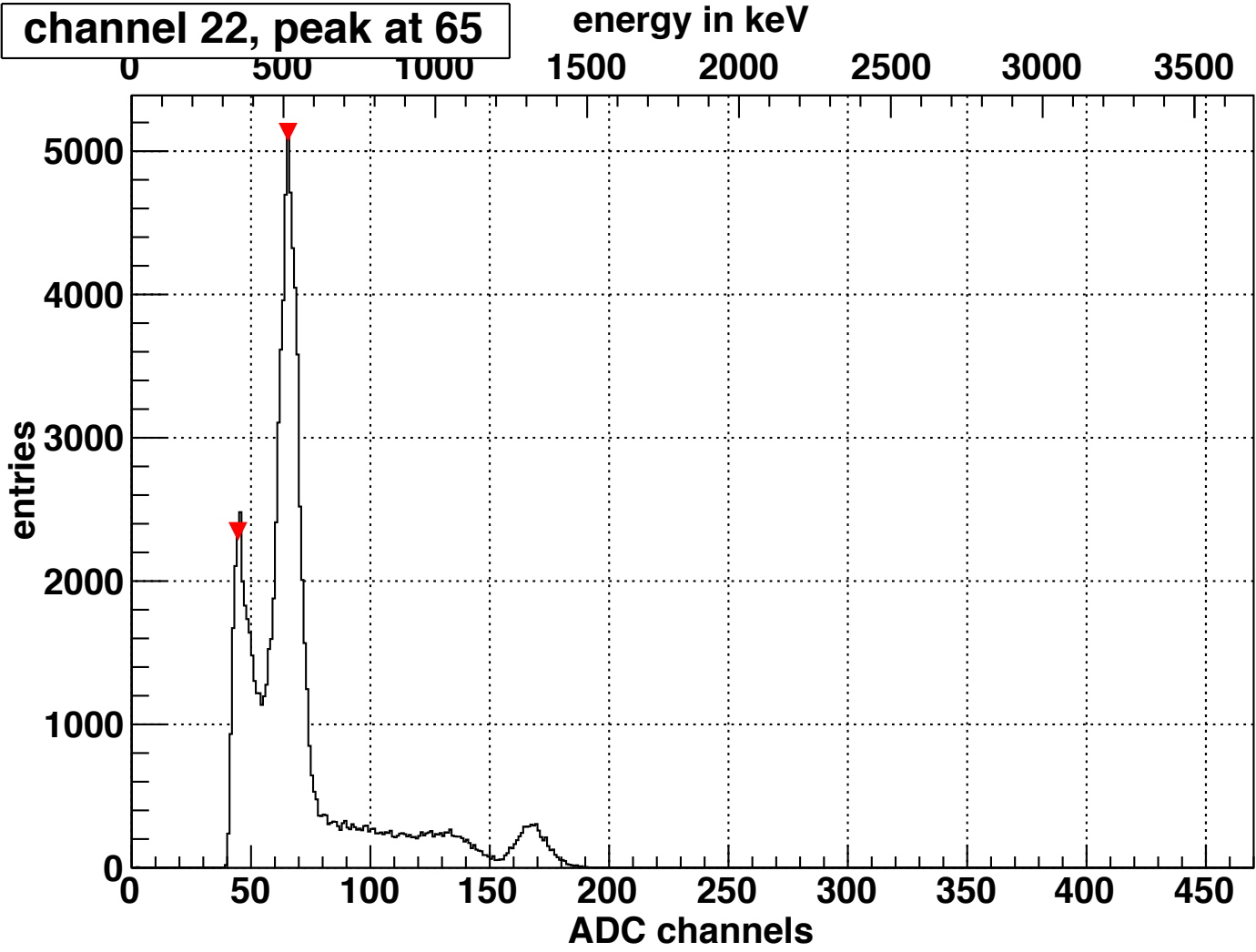


channel 21, peak at 69

energy in keV

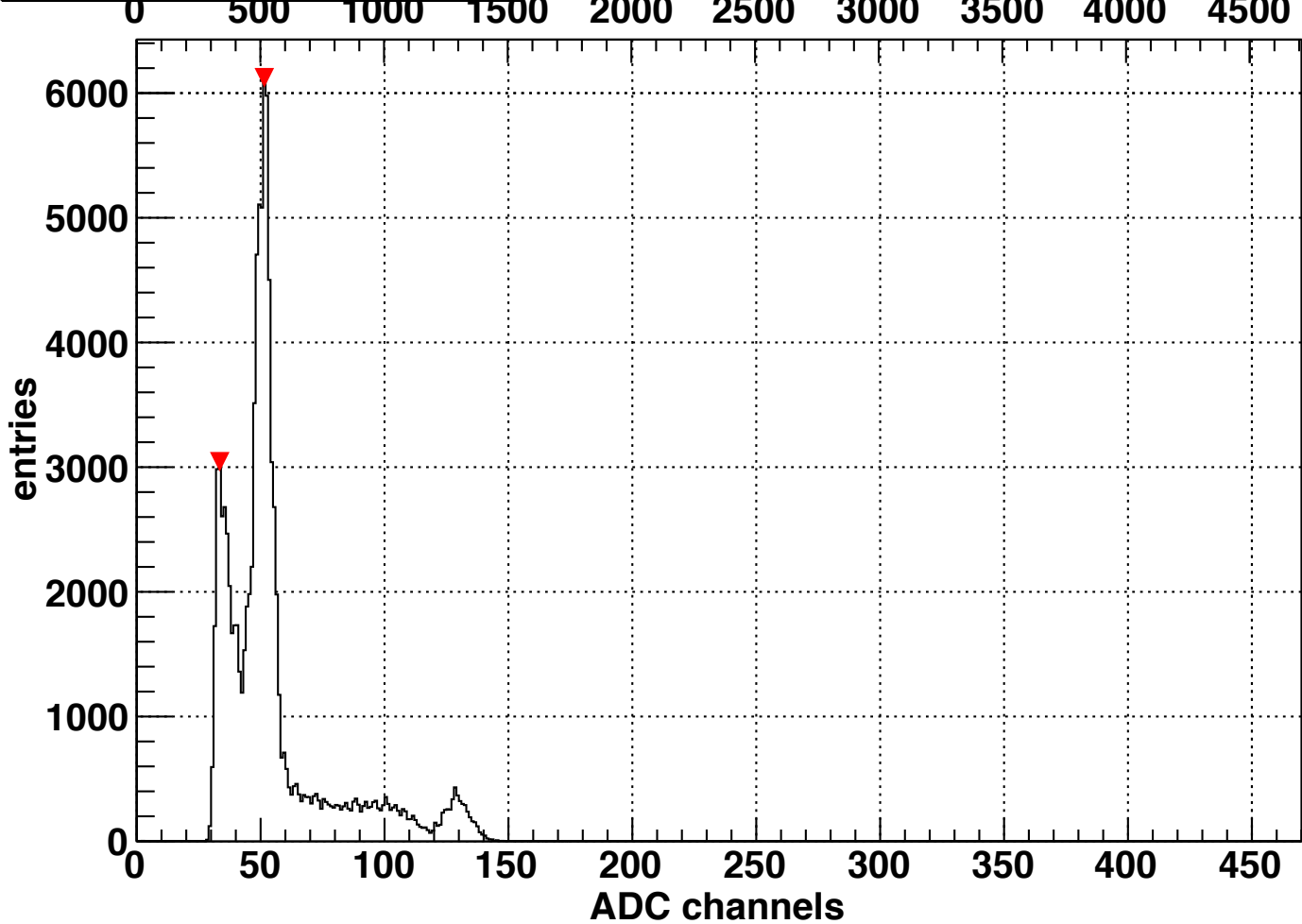


channel 22, peak at 65



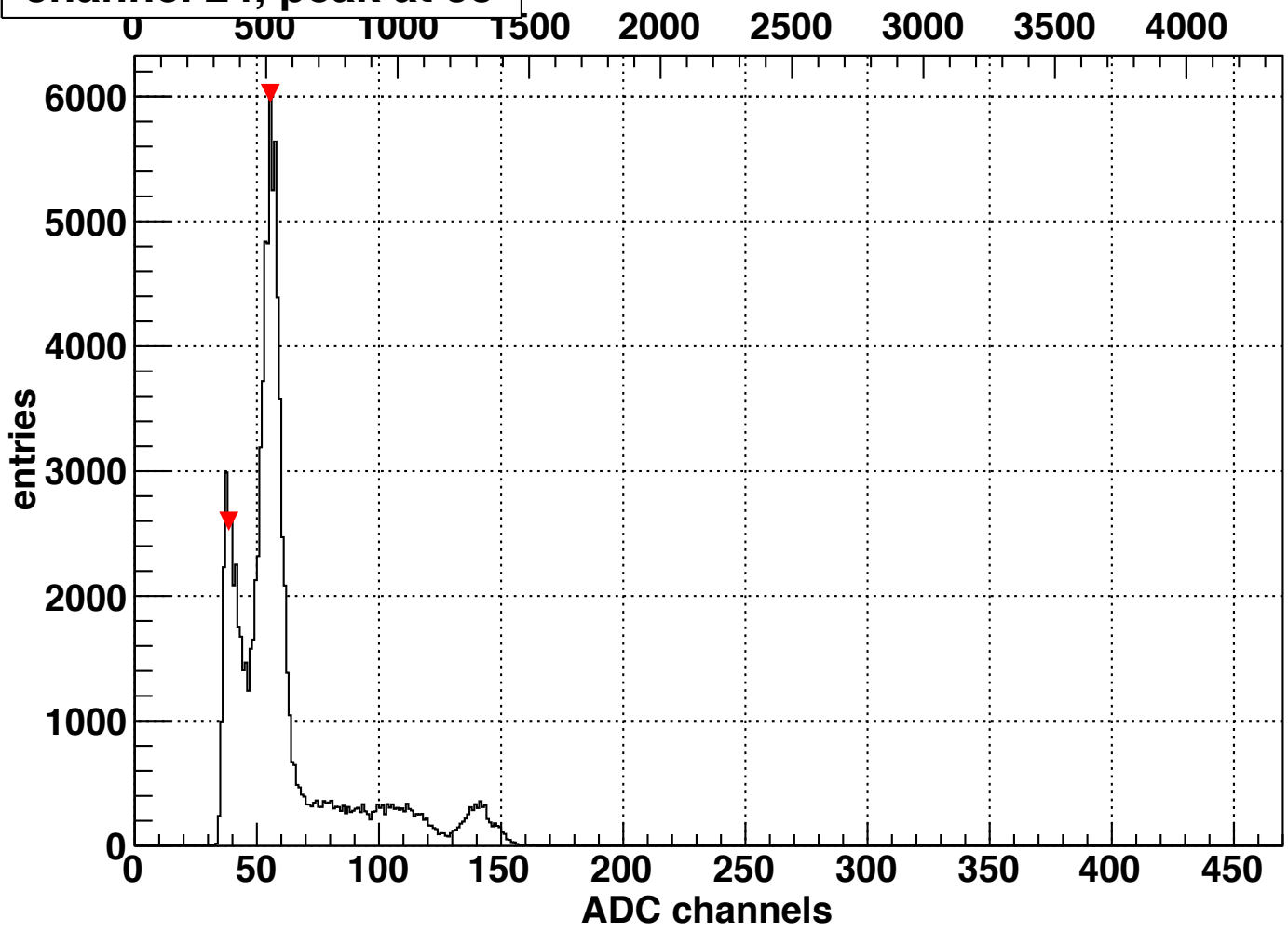
channel 23, peak at 51

energy in keV

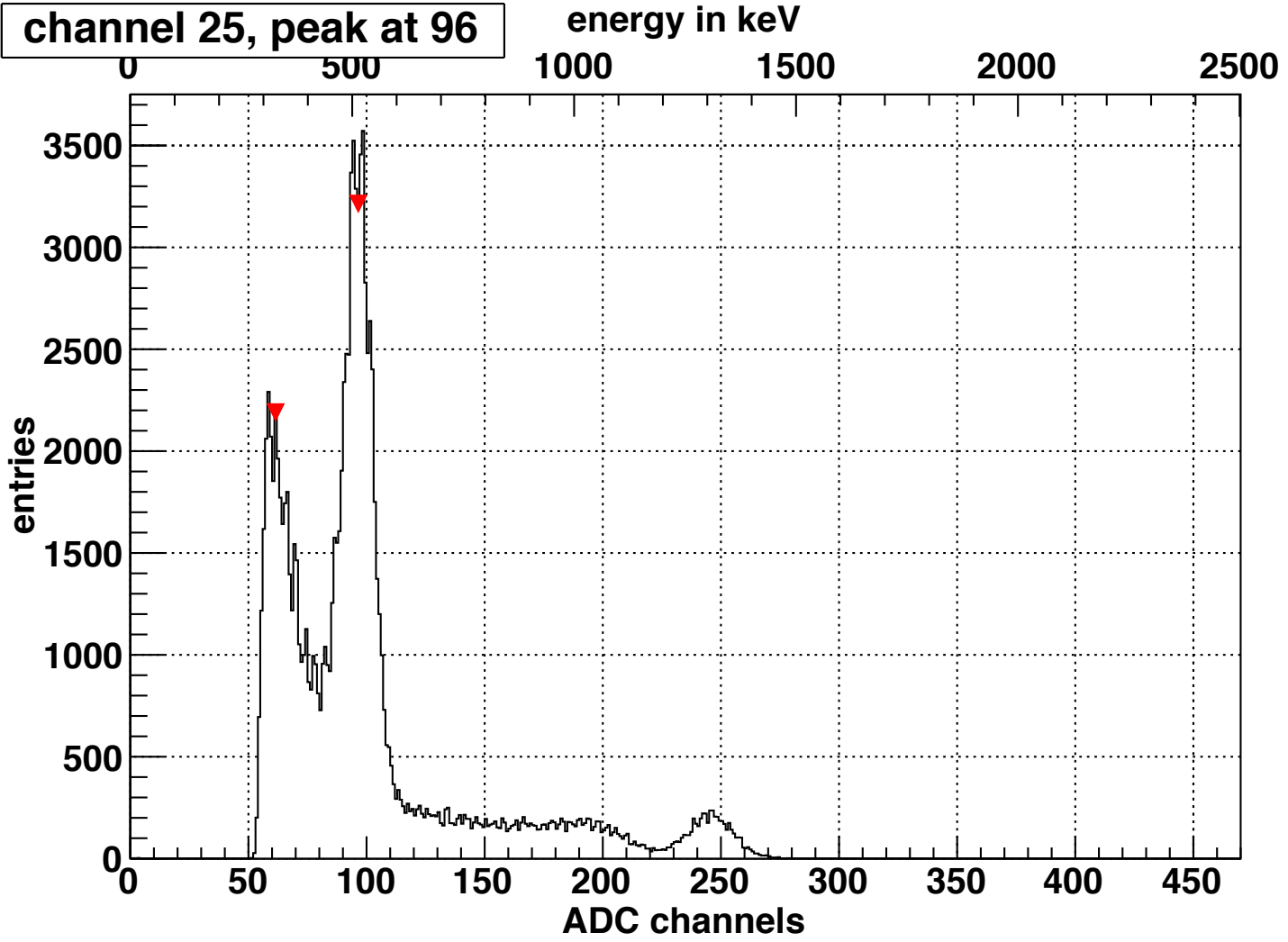


channel 24, peak at 55

energy in keV

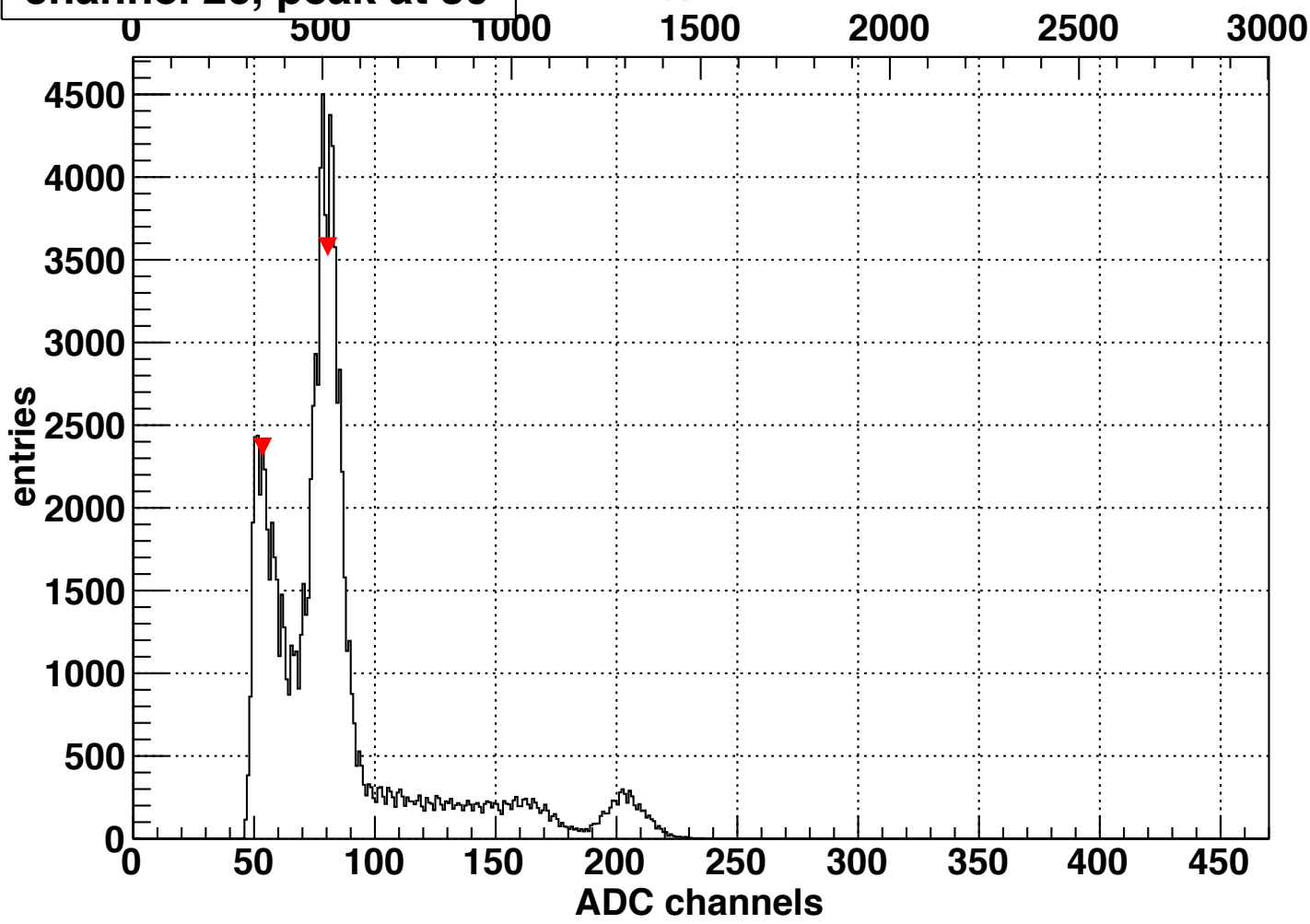


channel 25, peak at 96

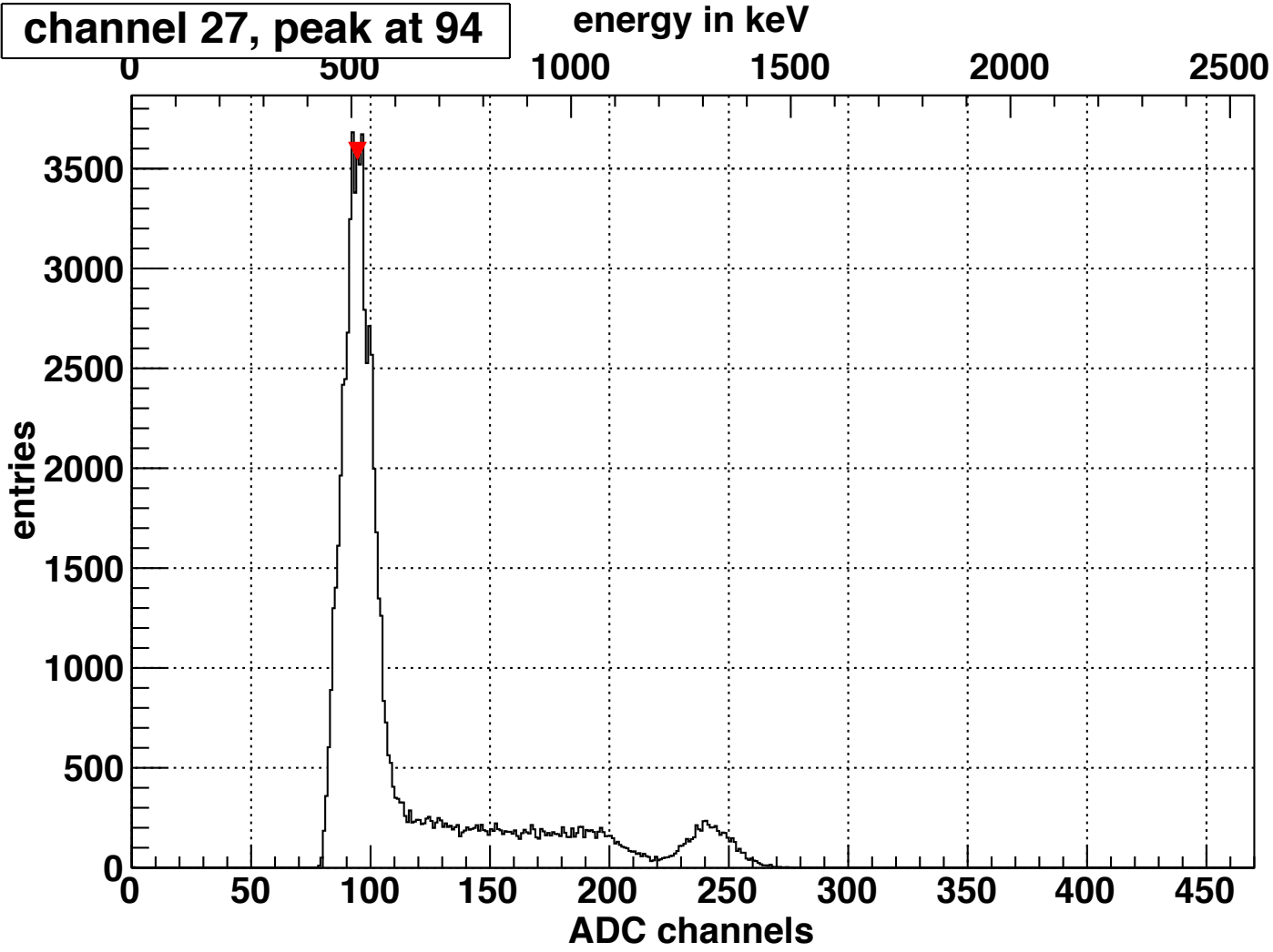


channel 26, peak at 80

energy in keV



channel 27, peak at 94



channel 28, peak at 69

energy in keV

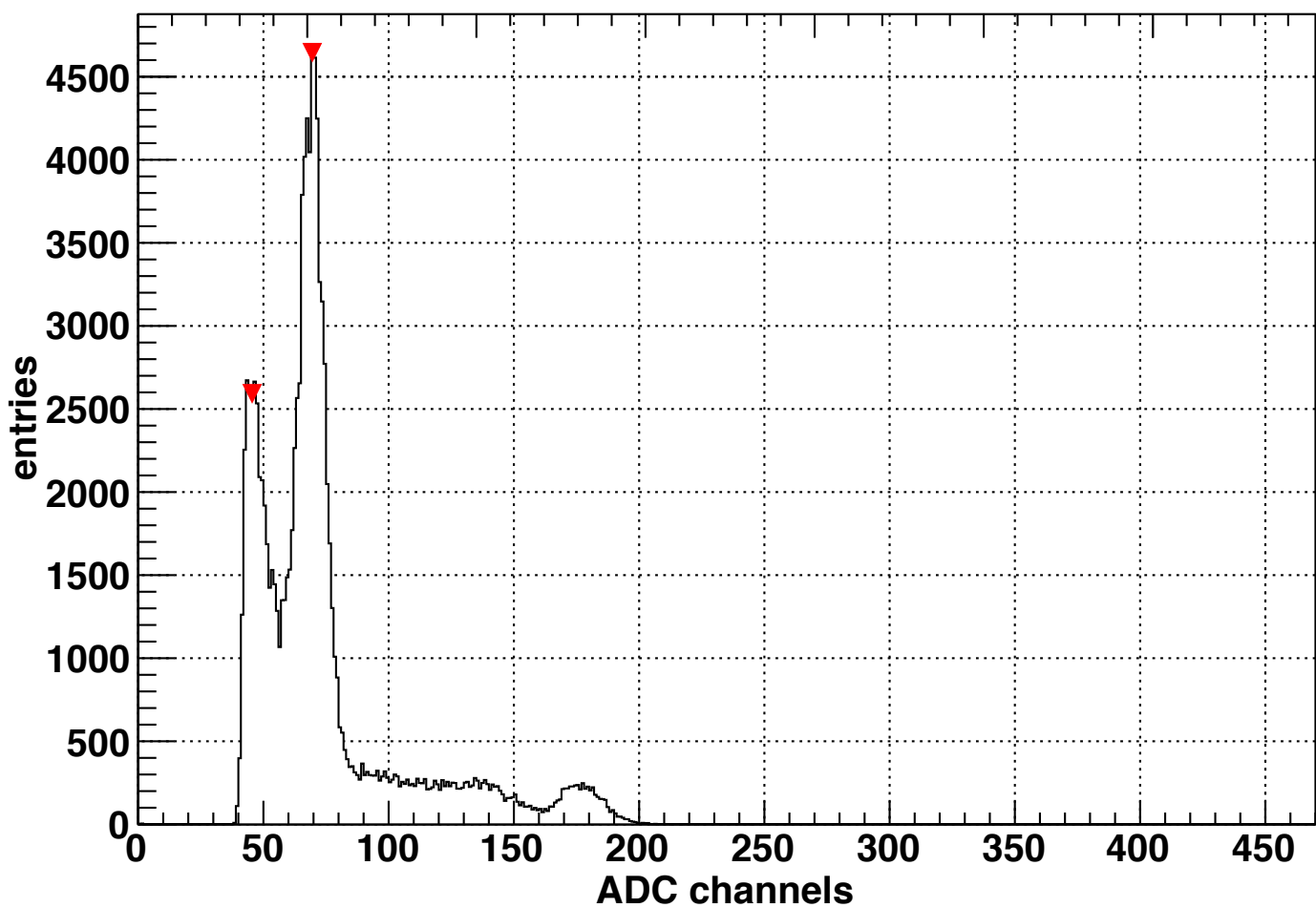
0 500 1000

1500

2000

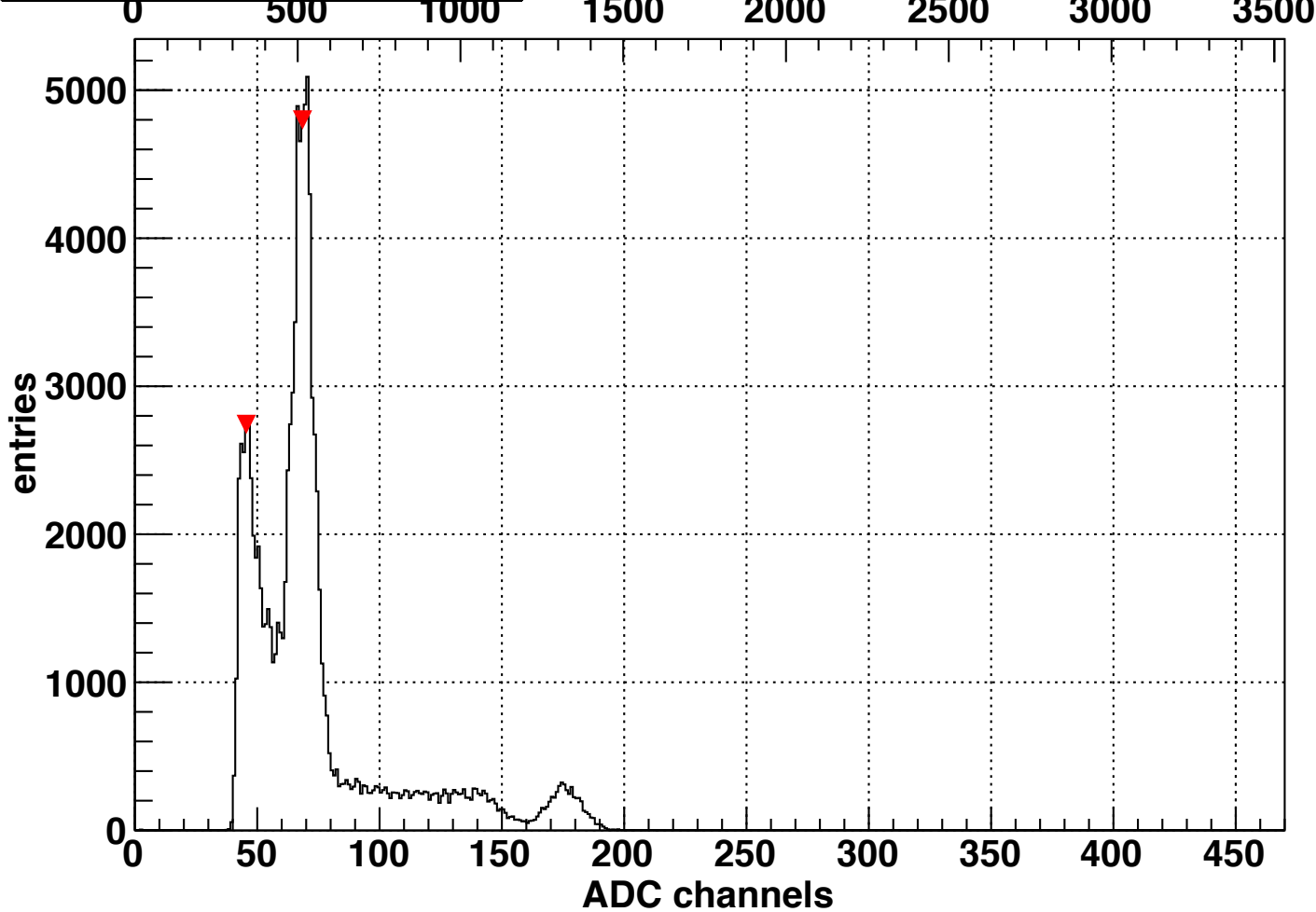
2500

3000



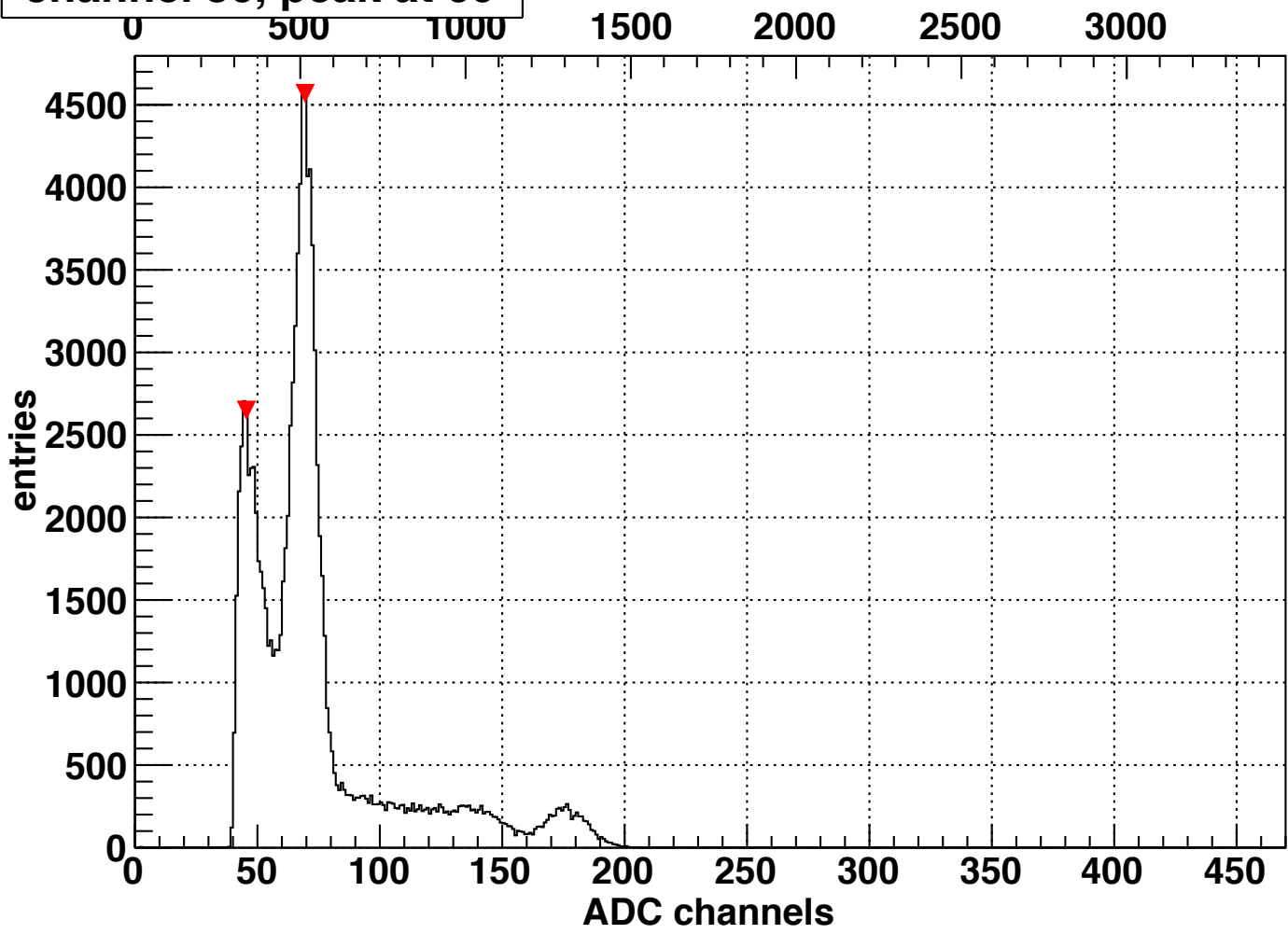
channel 29, peak at 68

energy in keV



channel 30, peak at 69

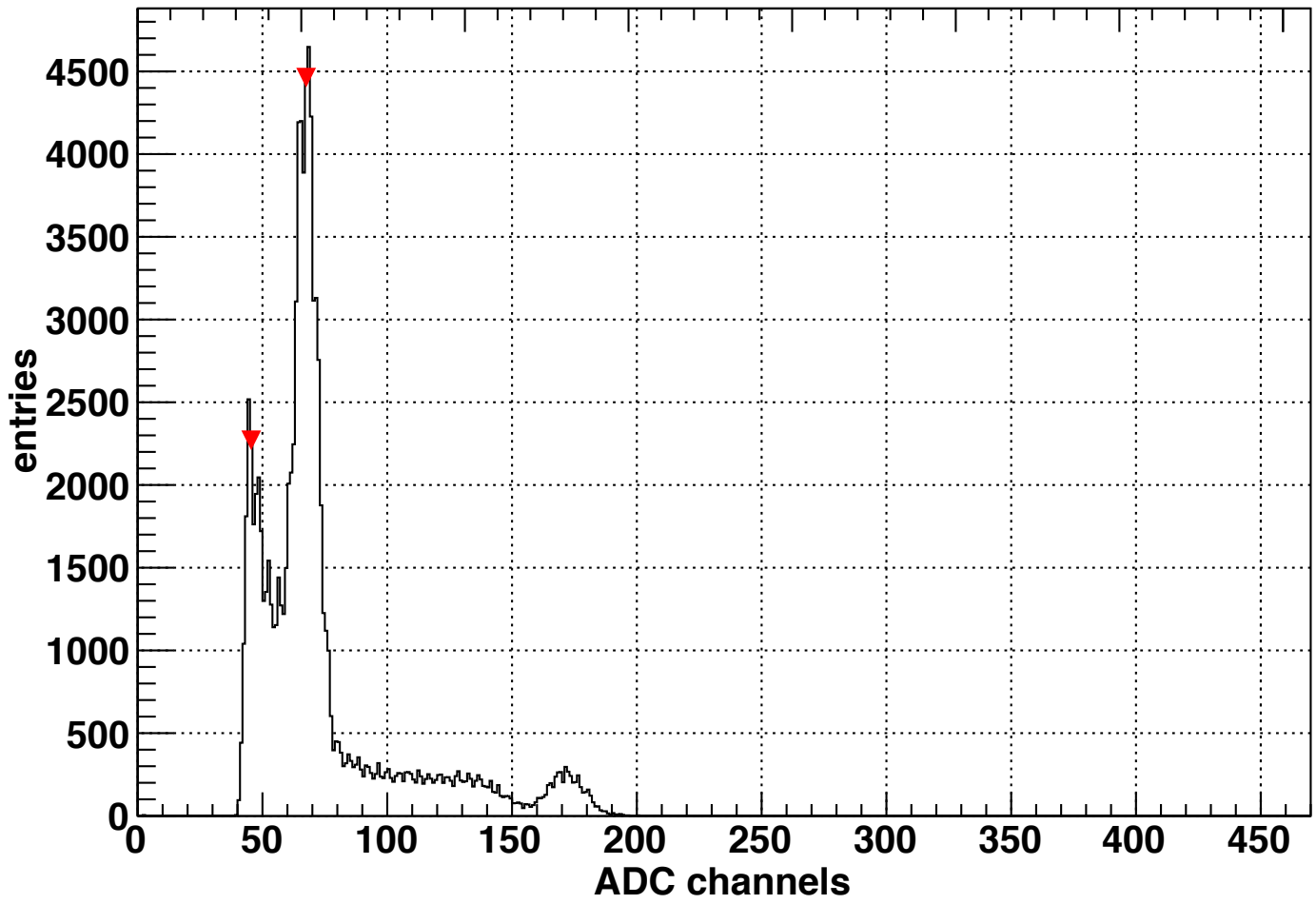
energy in keV



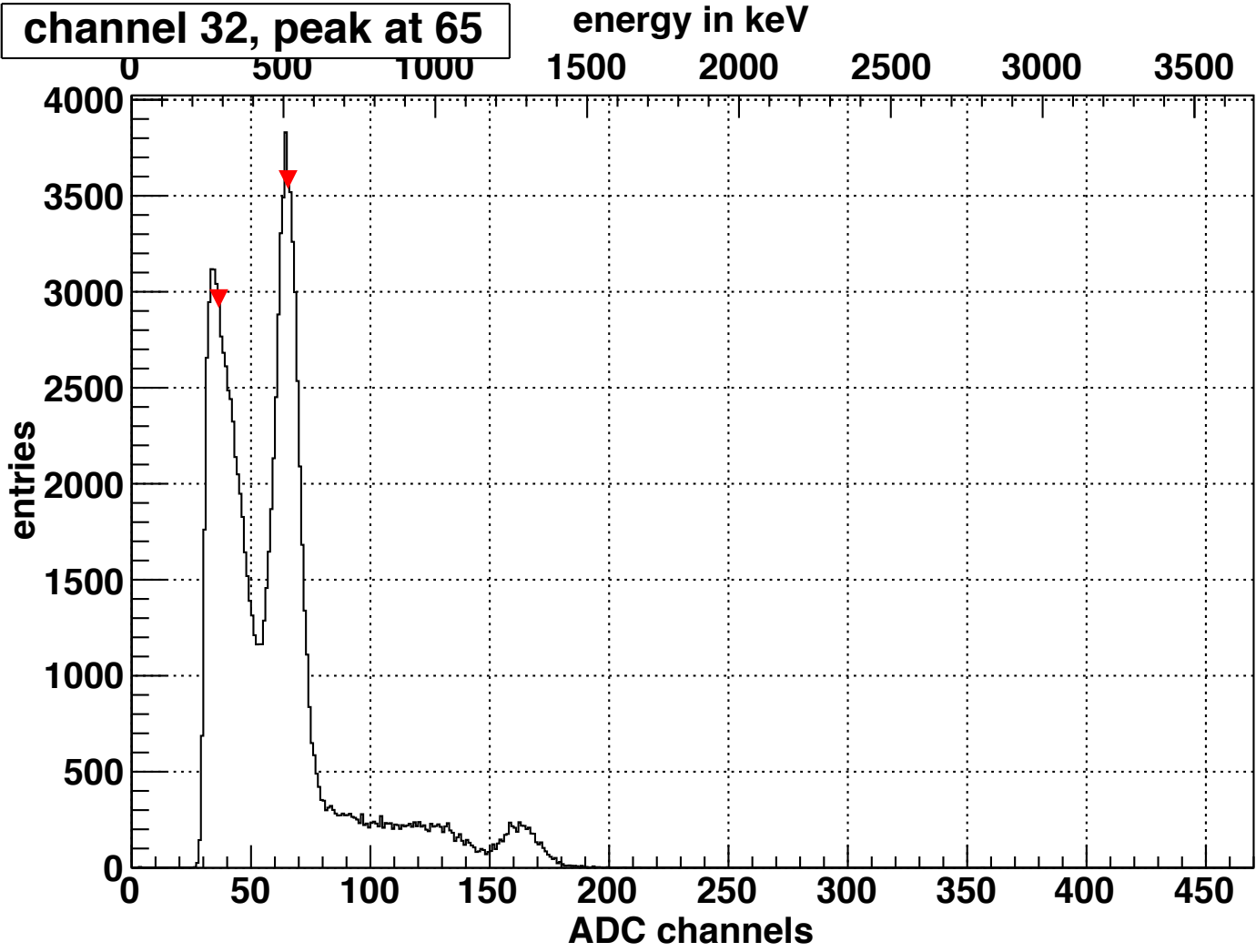
channel 31, peak at 67

energy in keV

0 500 1000 1500 2000 2500 3000 3500

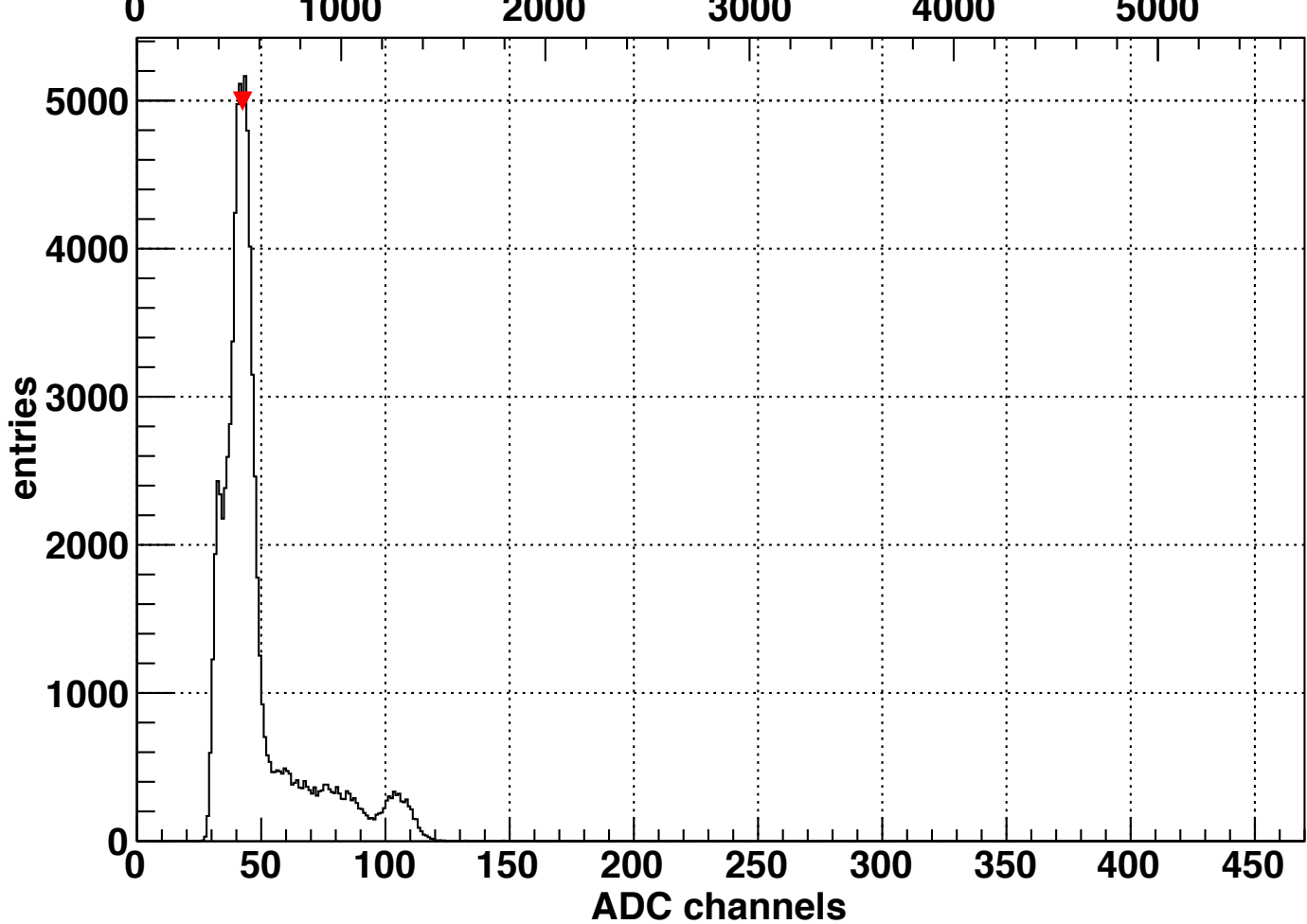


channel 32, peak at 65



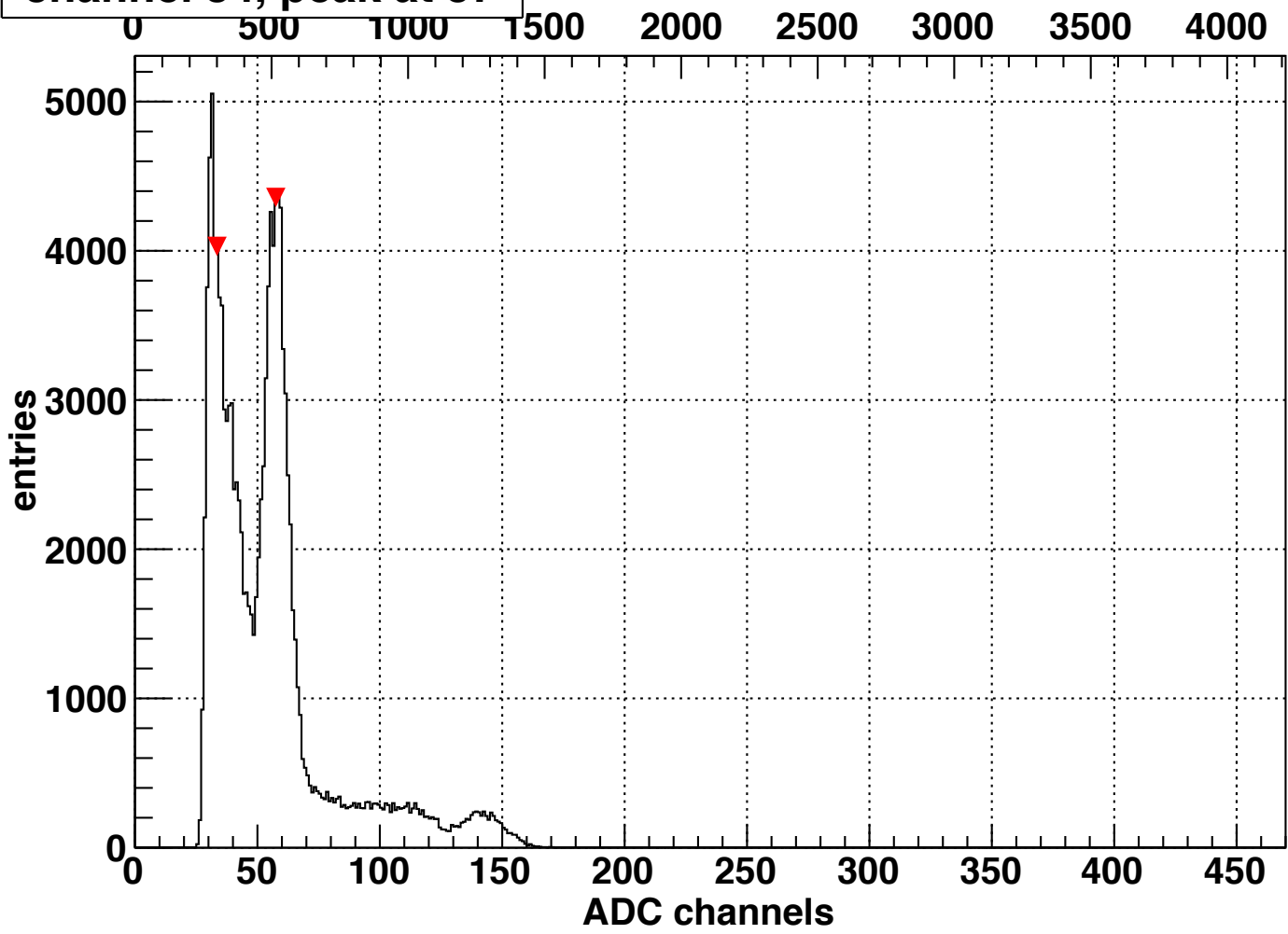
channel 33, peak at 42

energy in keV

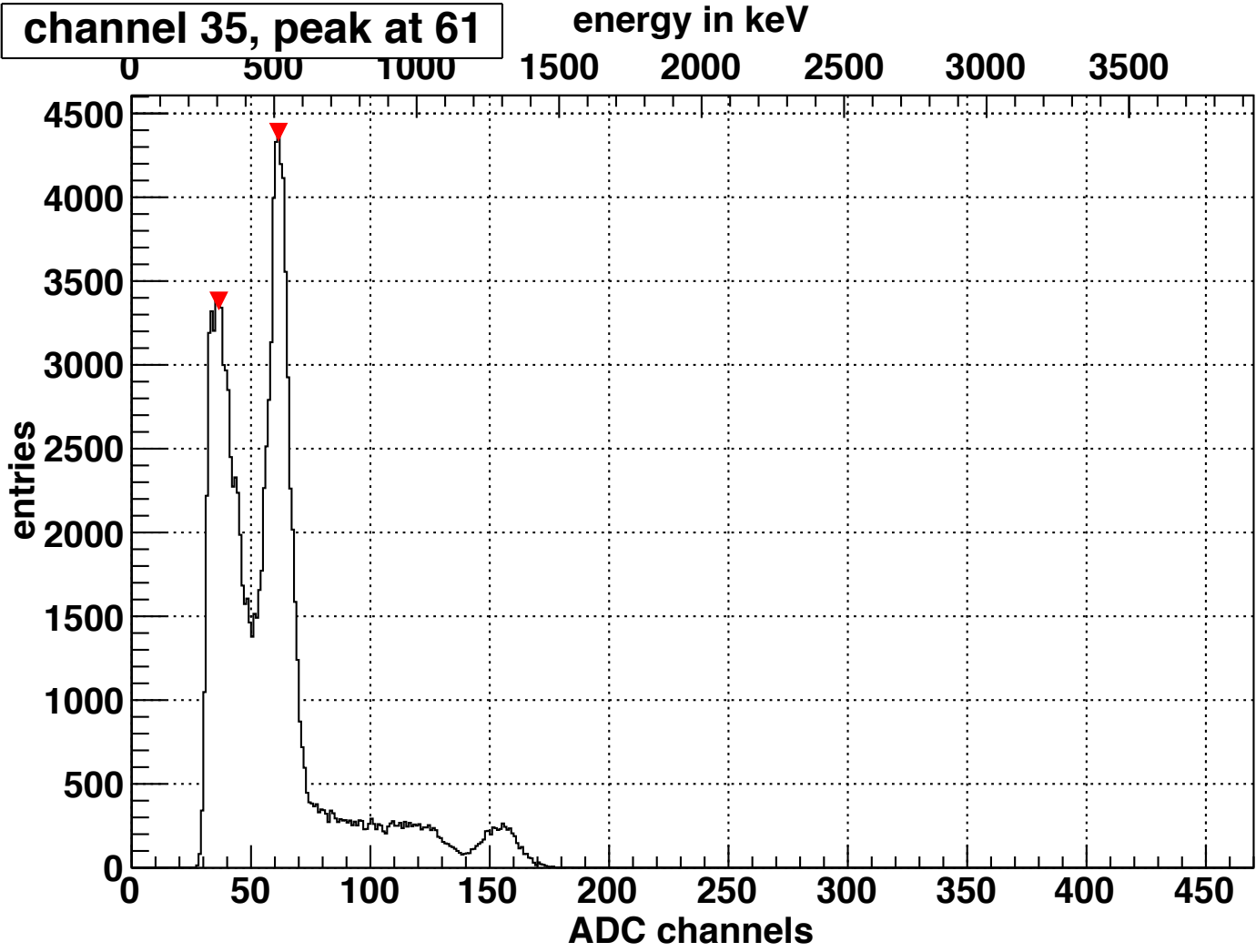


channel 34, peak at 57

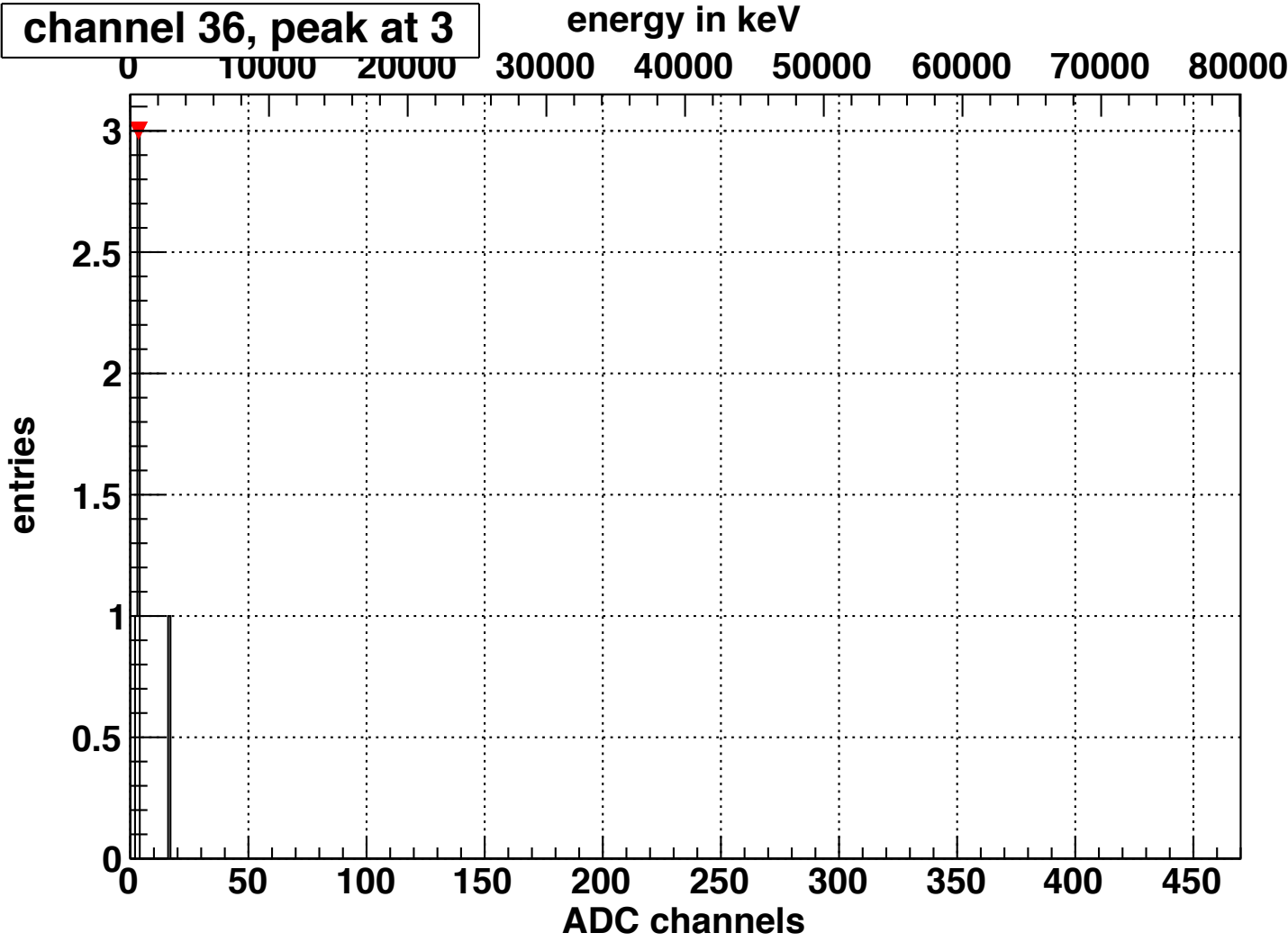
energy in keV



channel 35, peak at 61

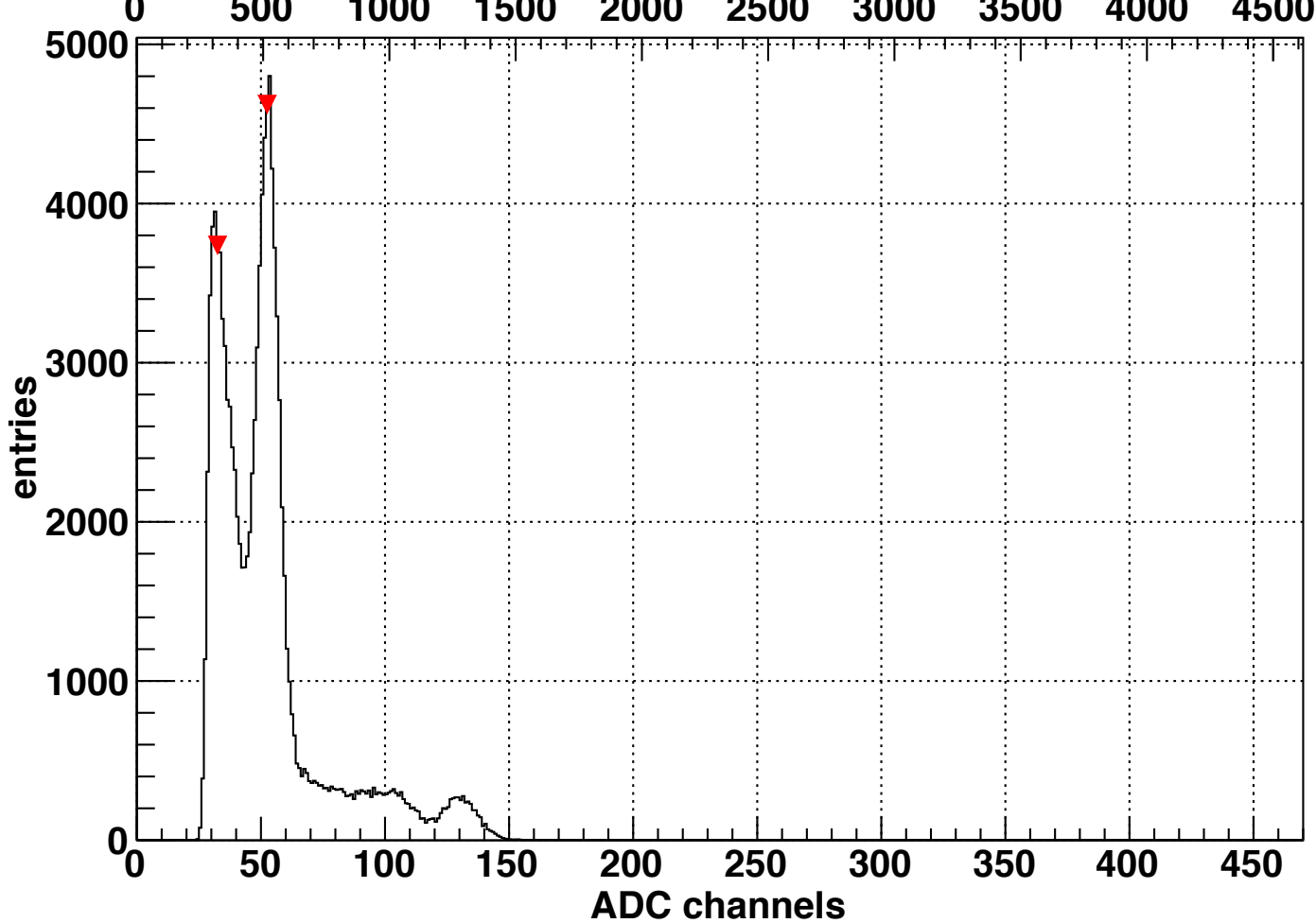


channel 36, peak at 3



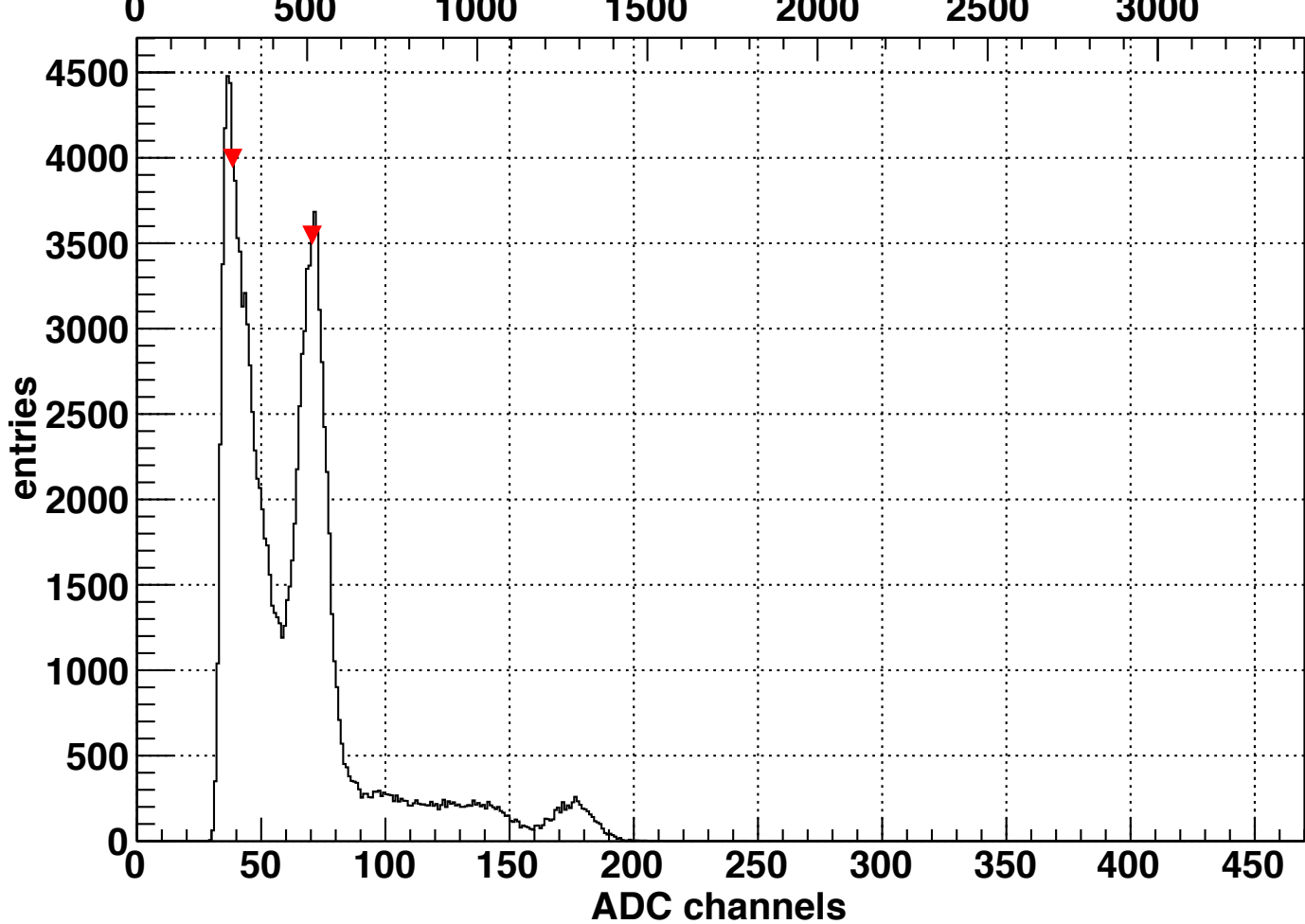
channel 37, peak at 52

energy in keV



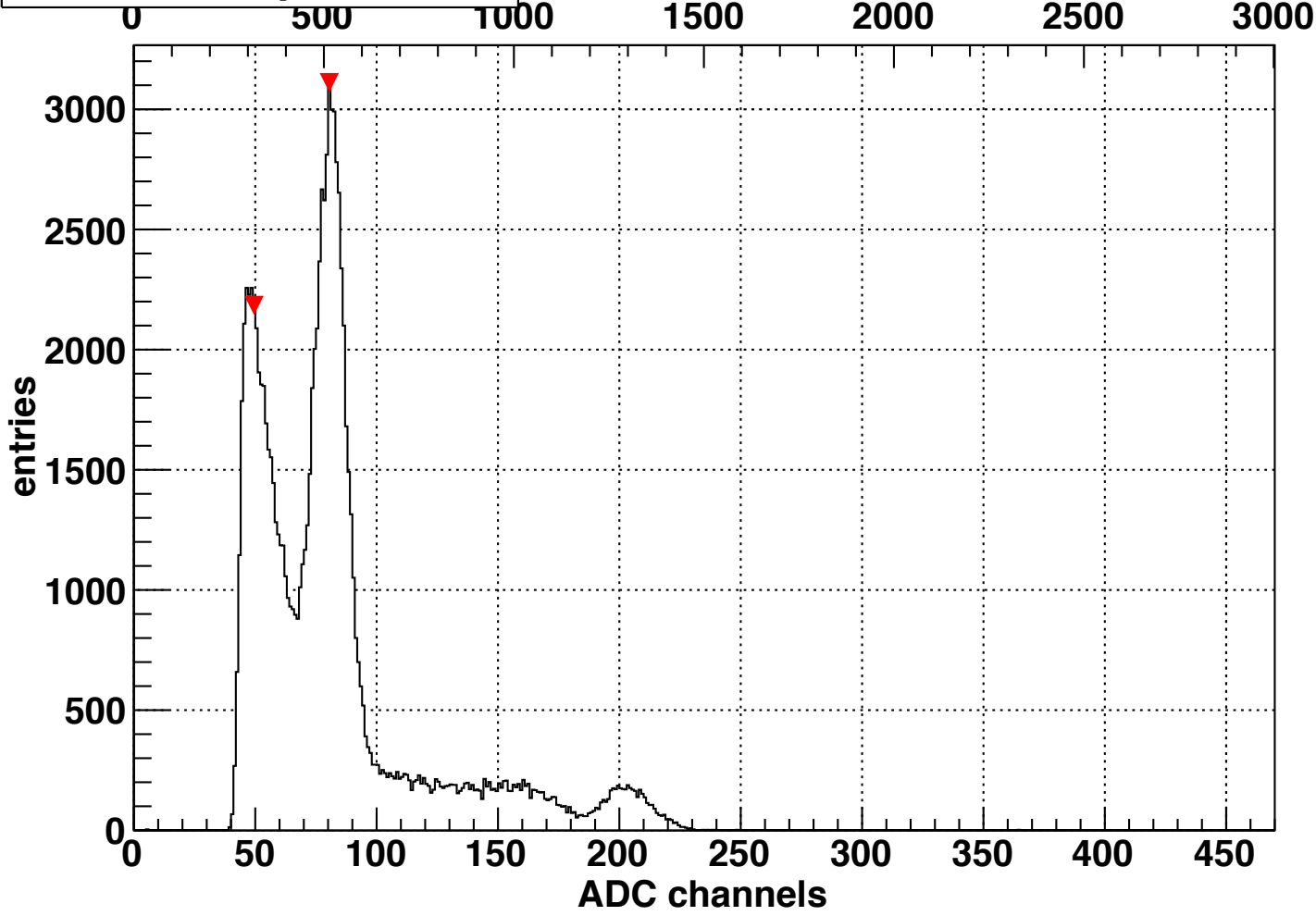
channel 38, peak at 70

energy in keV



channel 39, peak at 80

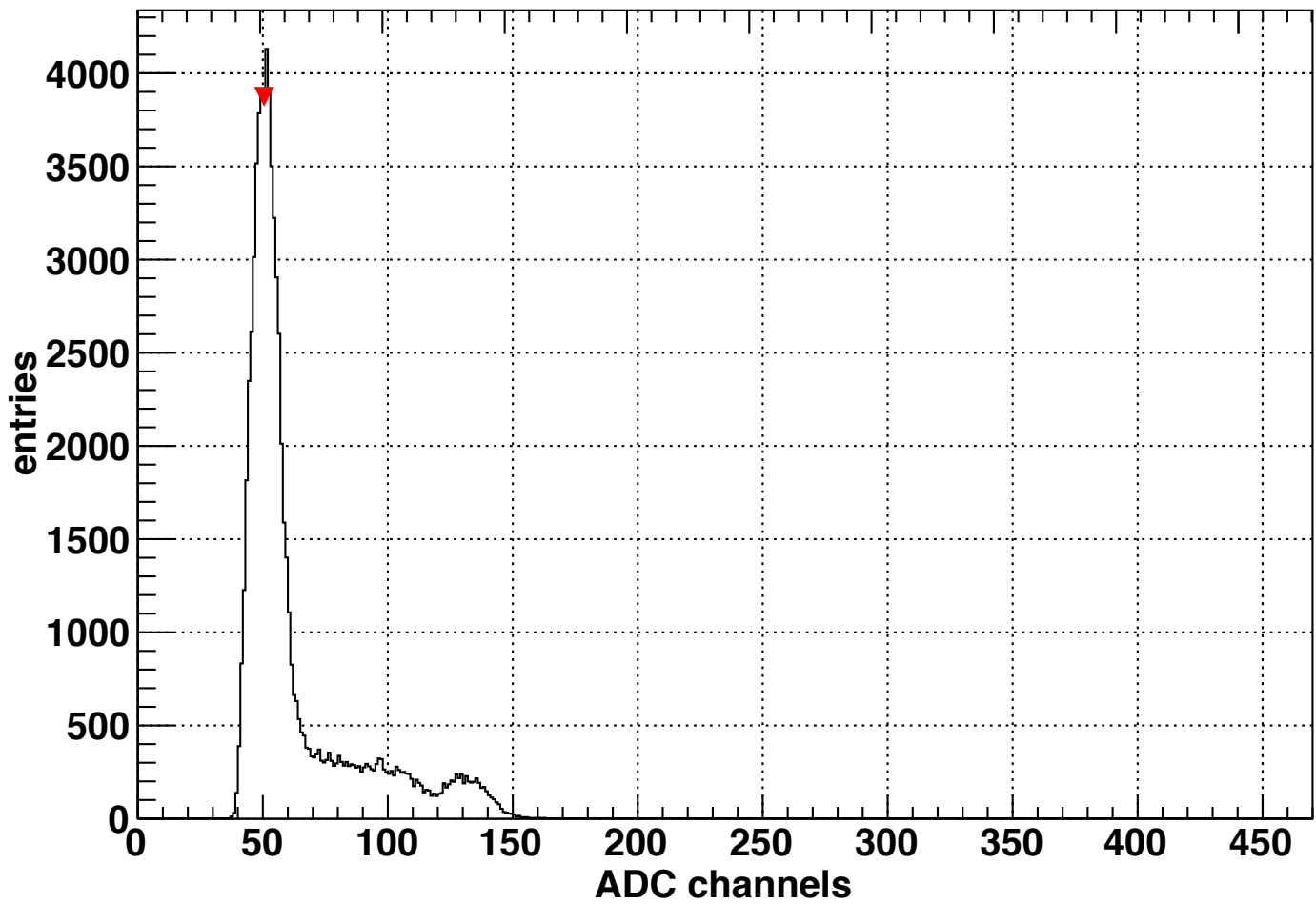
energy in keV



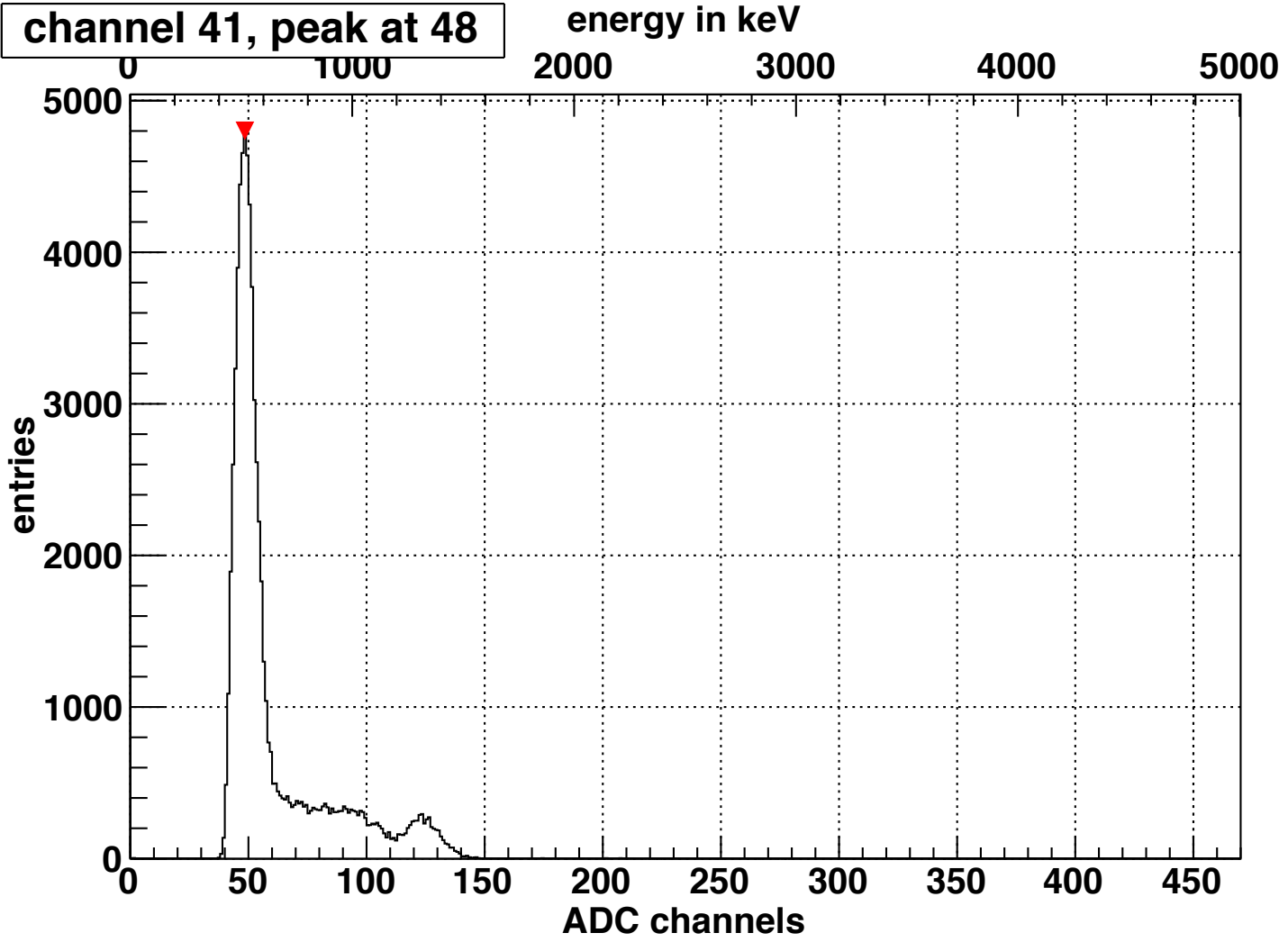
channel 40, peak at 50

energy in keV

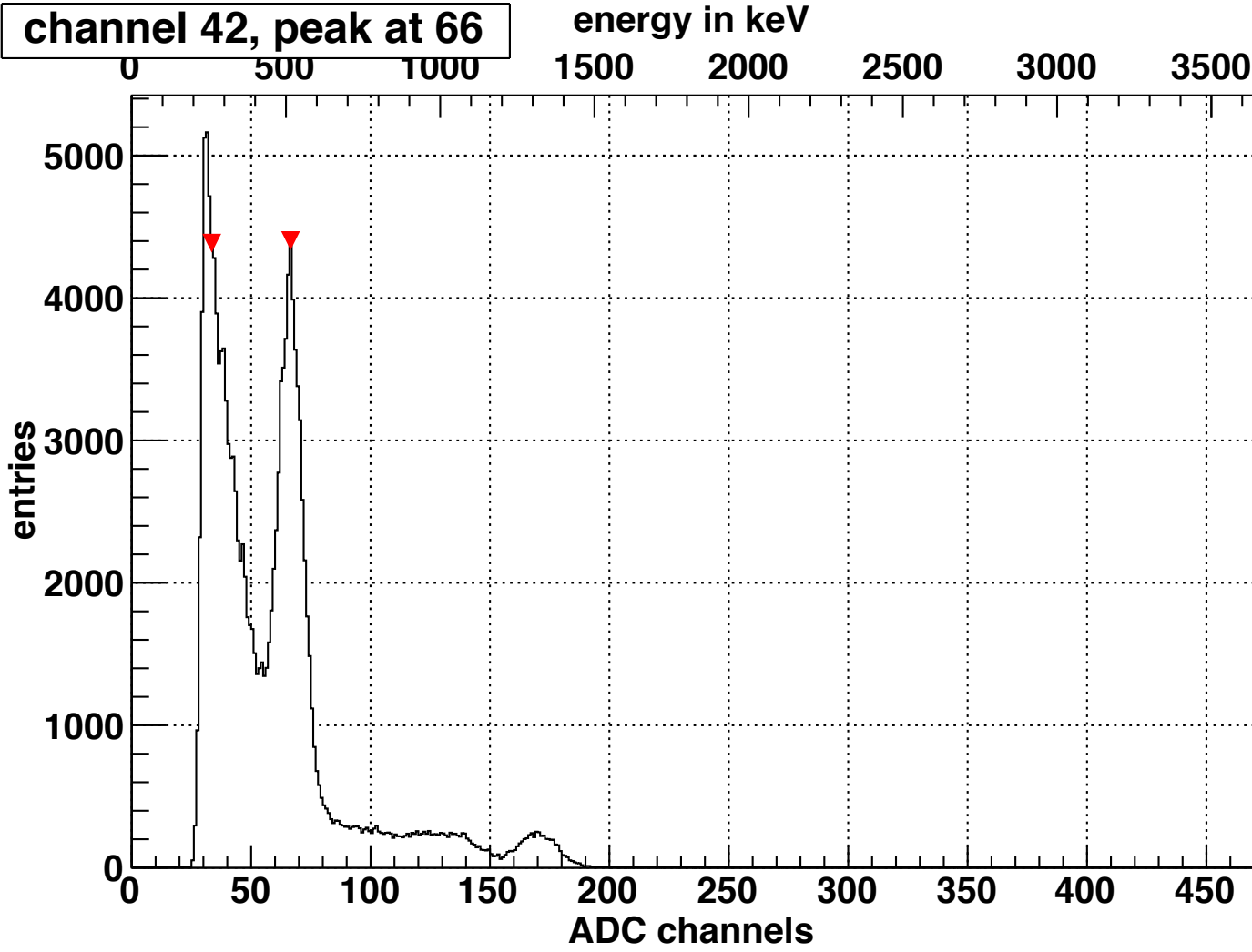
0 500 1000 1500 2000 2500 3000 3500 4000 4500



channel 41, peak at 48

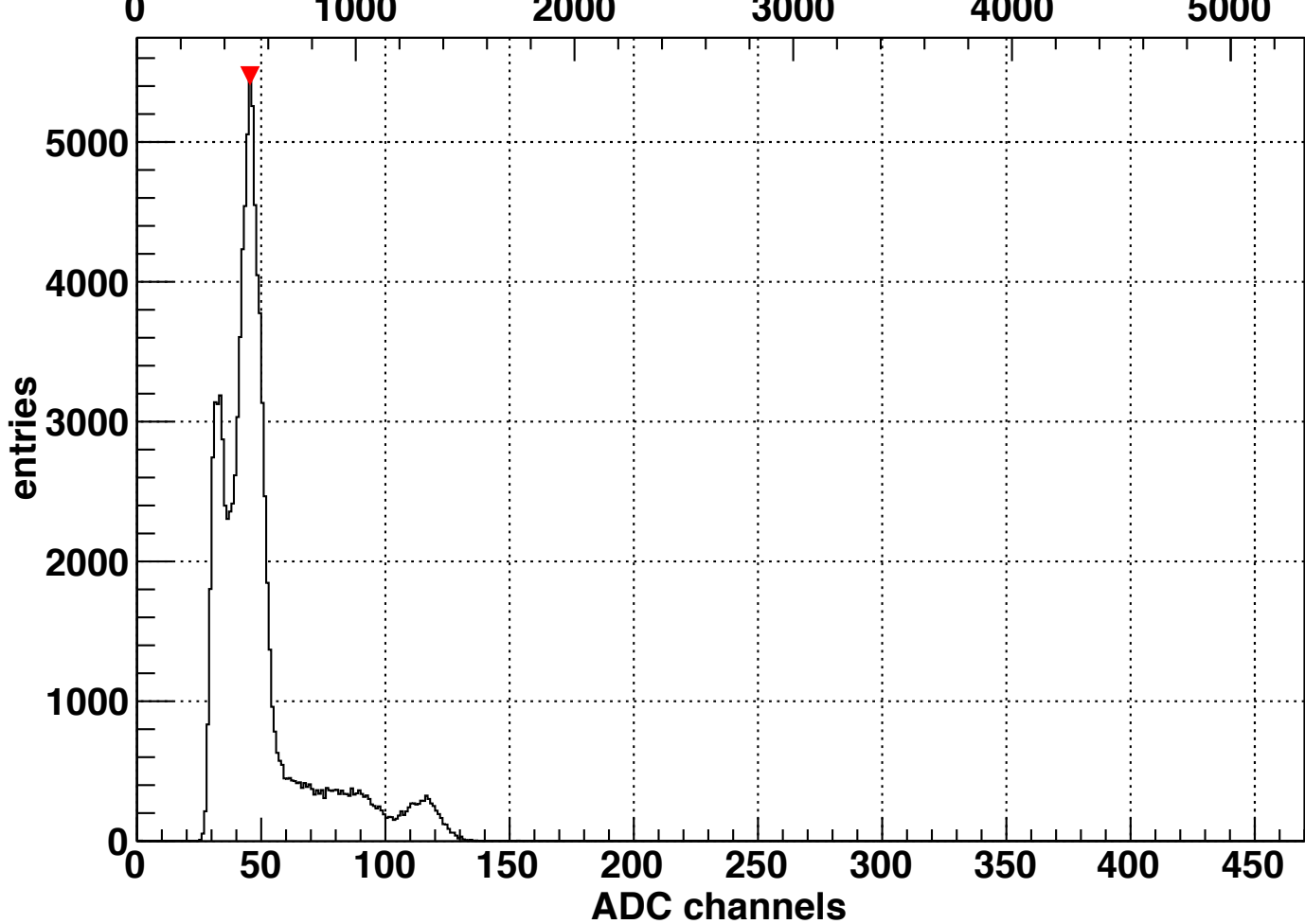


channel 42, peak at 66

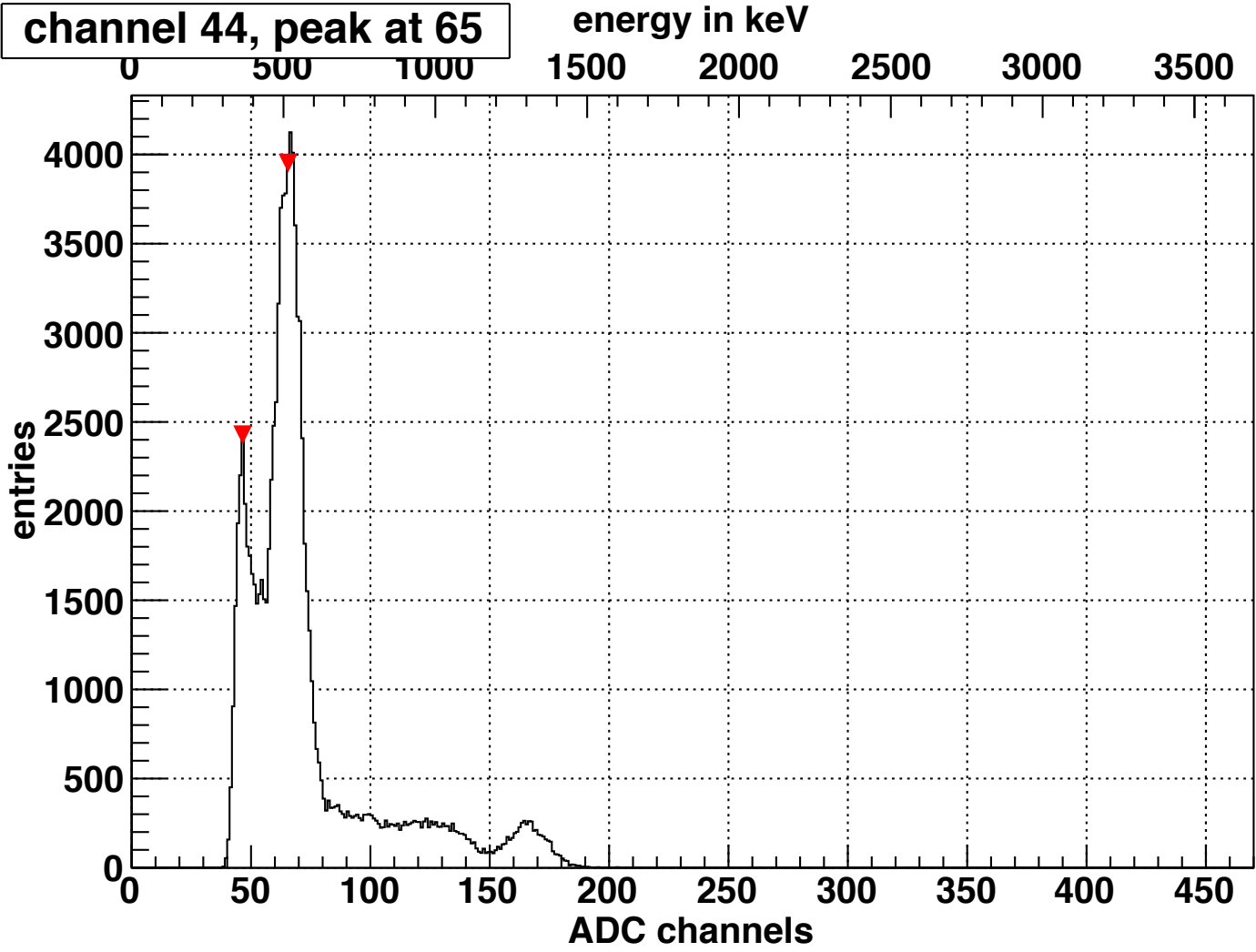


channel 43, peak at 45

energy in keV

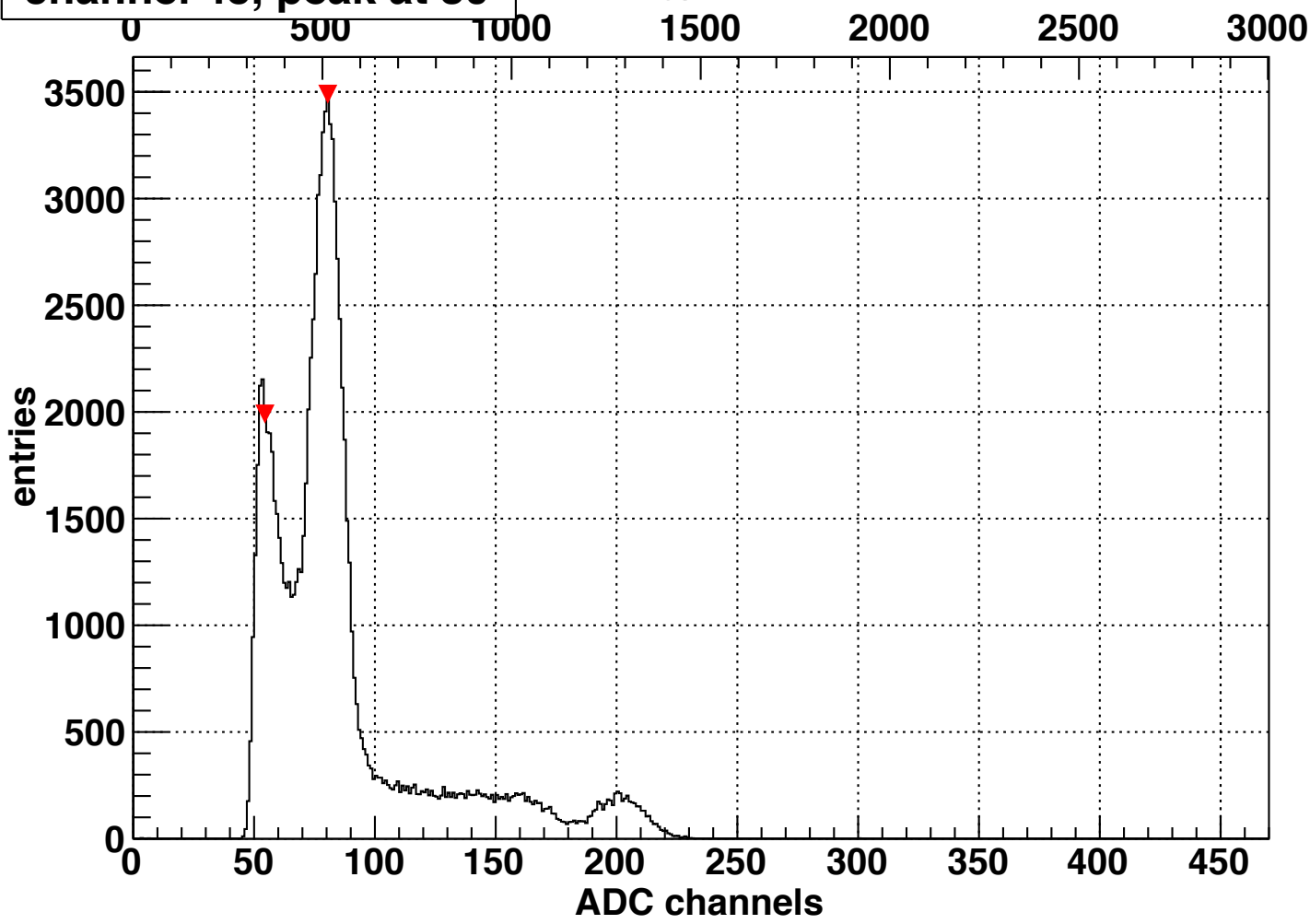


channel 44, peak at 65



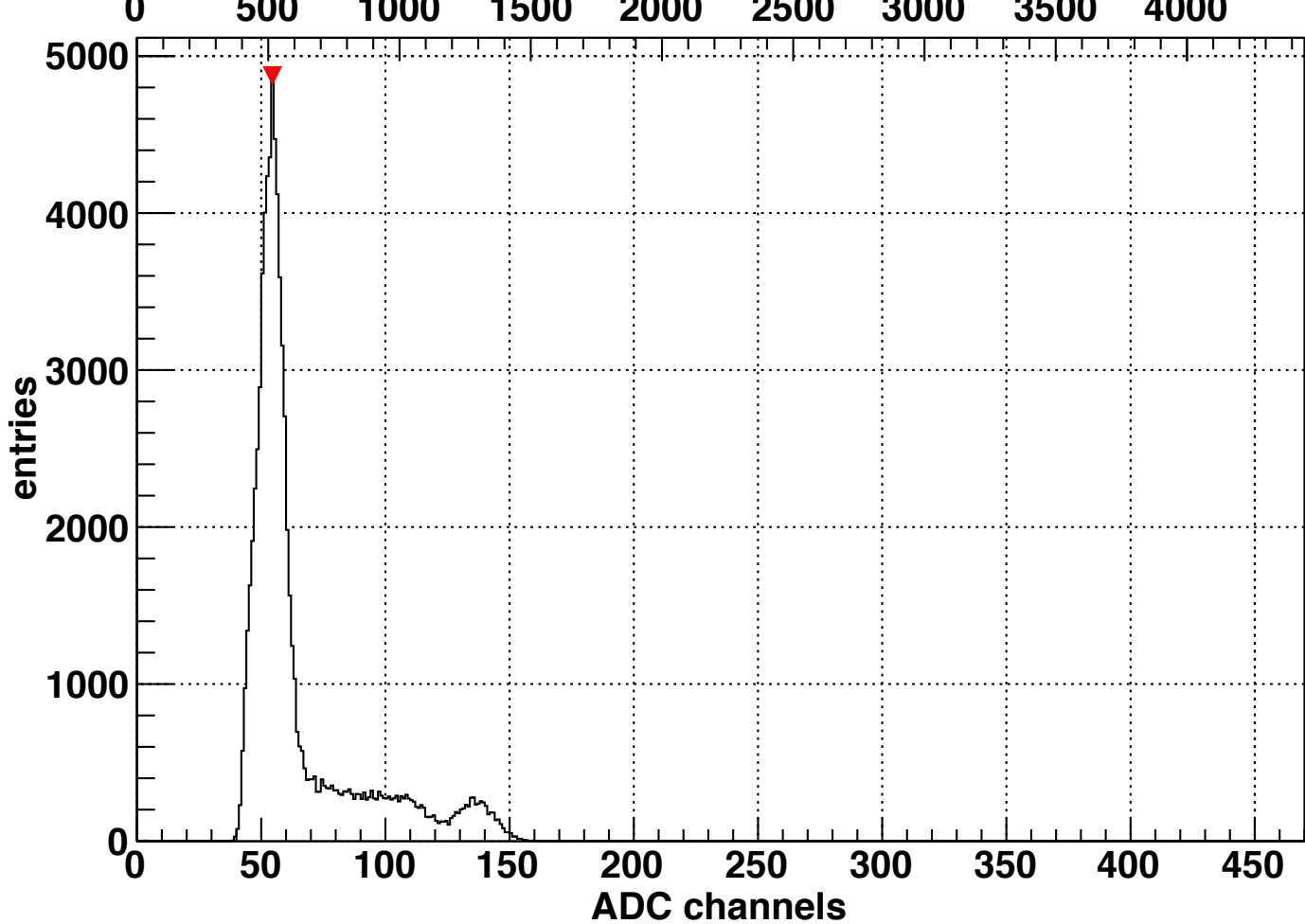
channel 45, peak at 80

energy in keV



channel 46, peak at 54

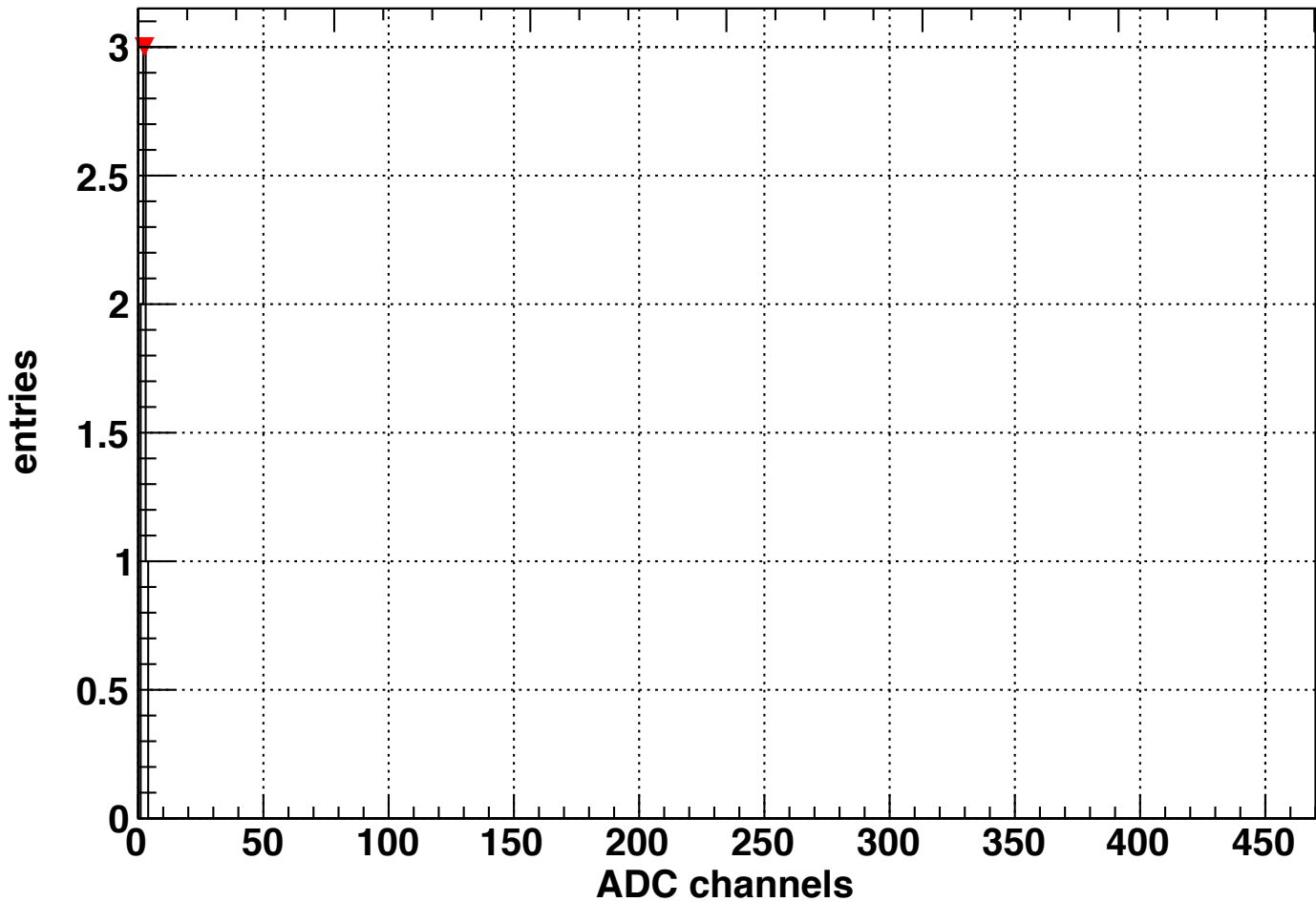
energy in keV



channel 47, peak at 2

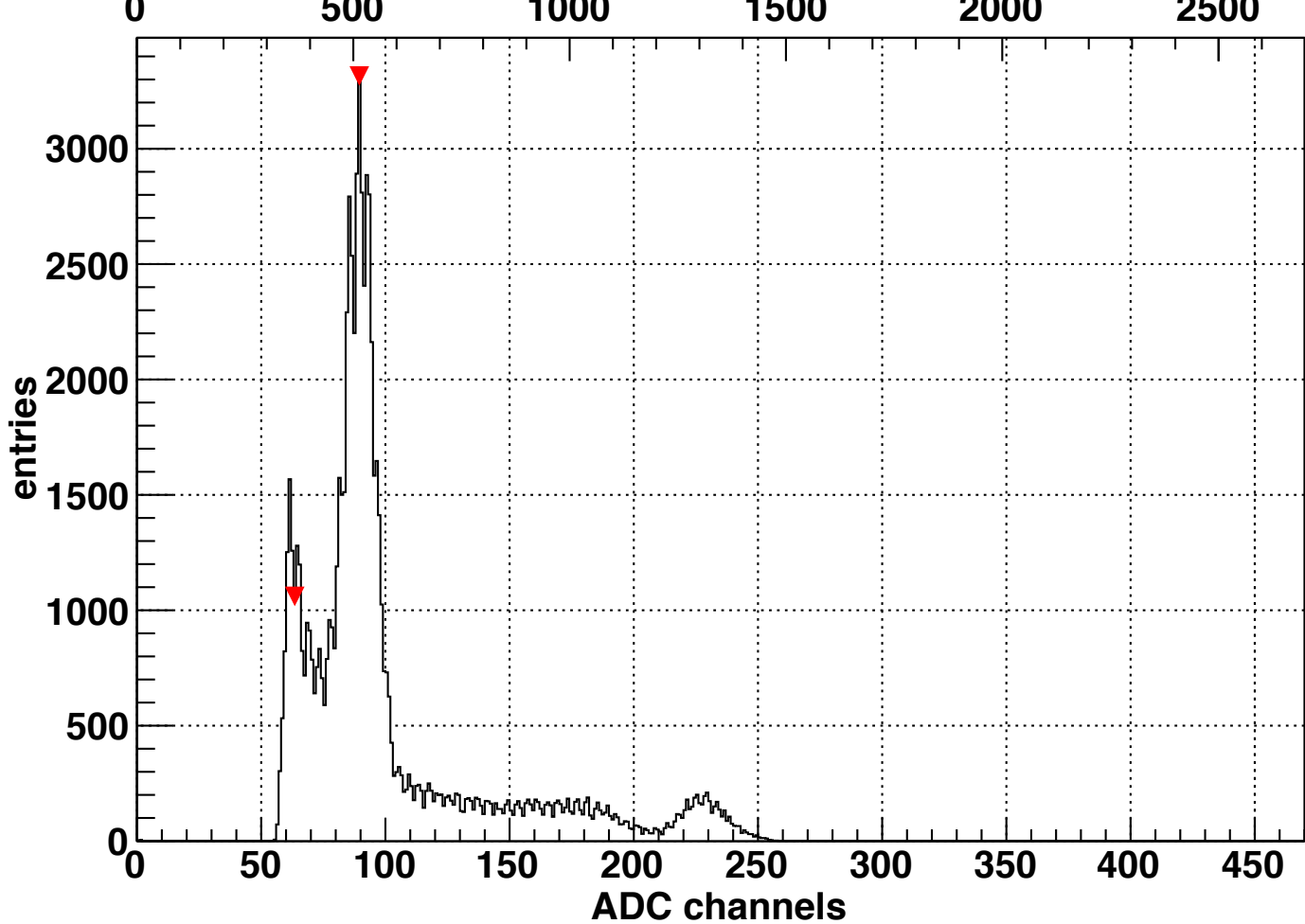
energy in keV

$\times 10^3$



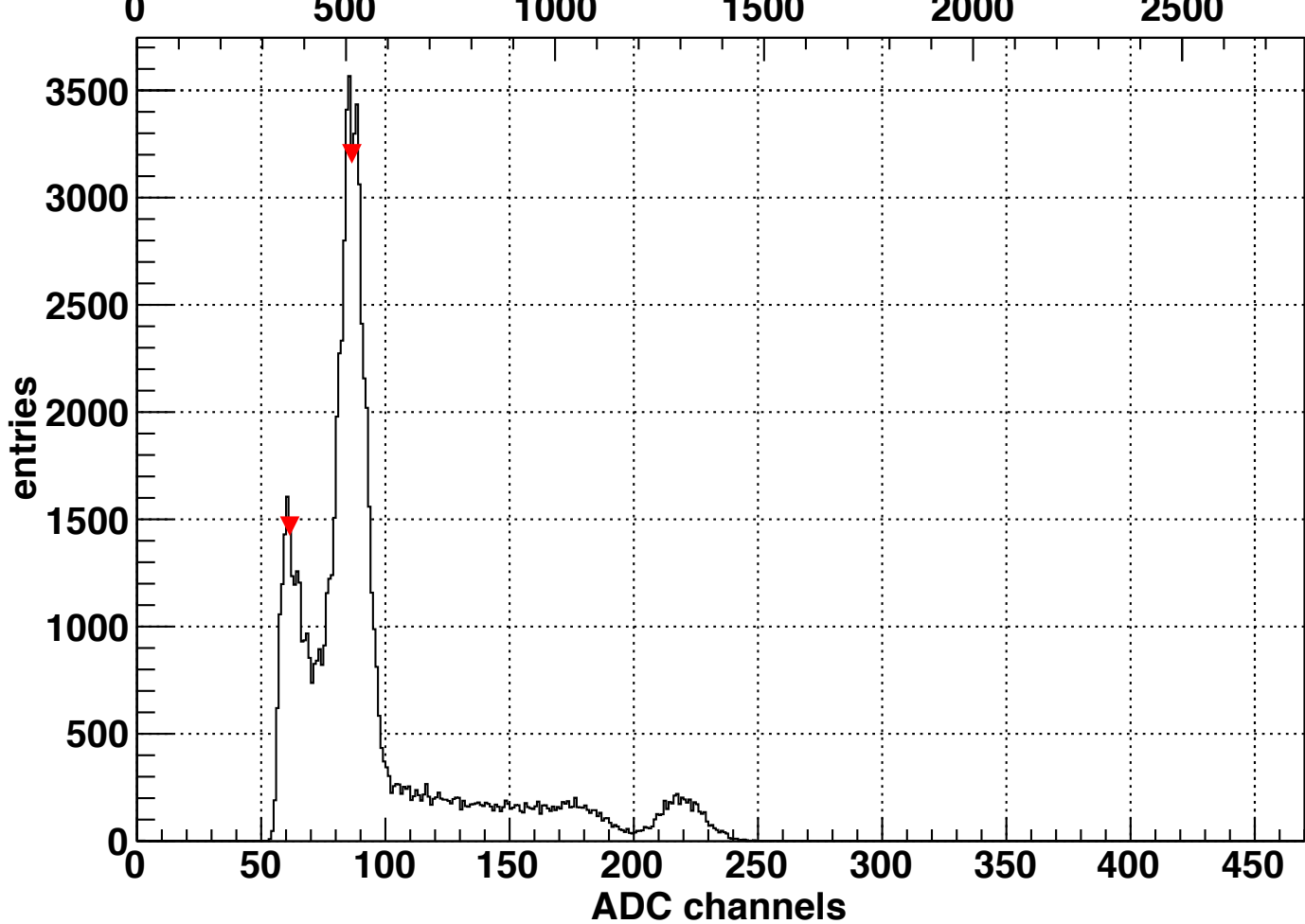
channel 48, peak at 89

energy in keV

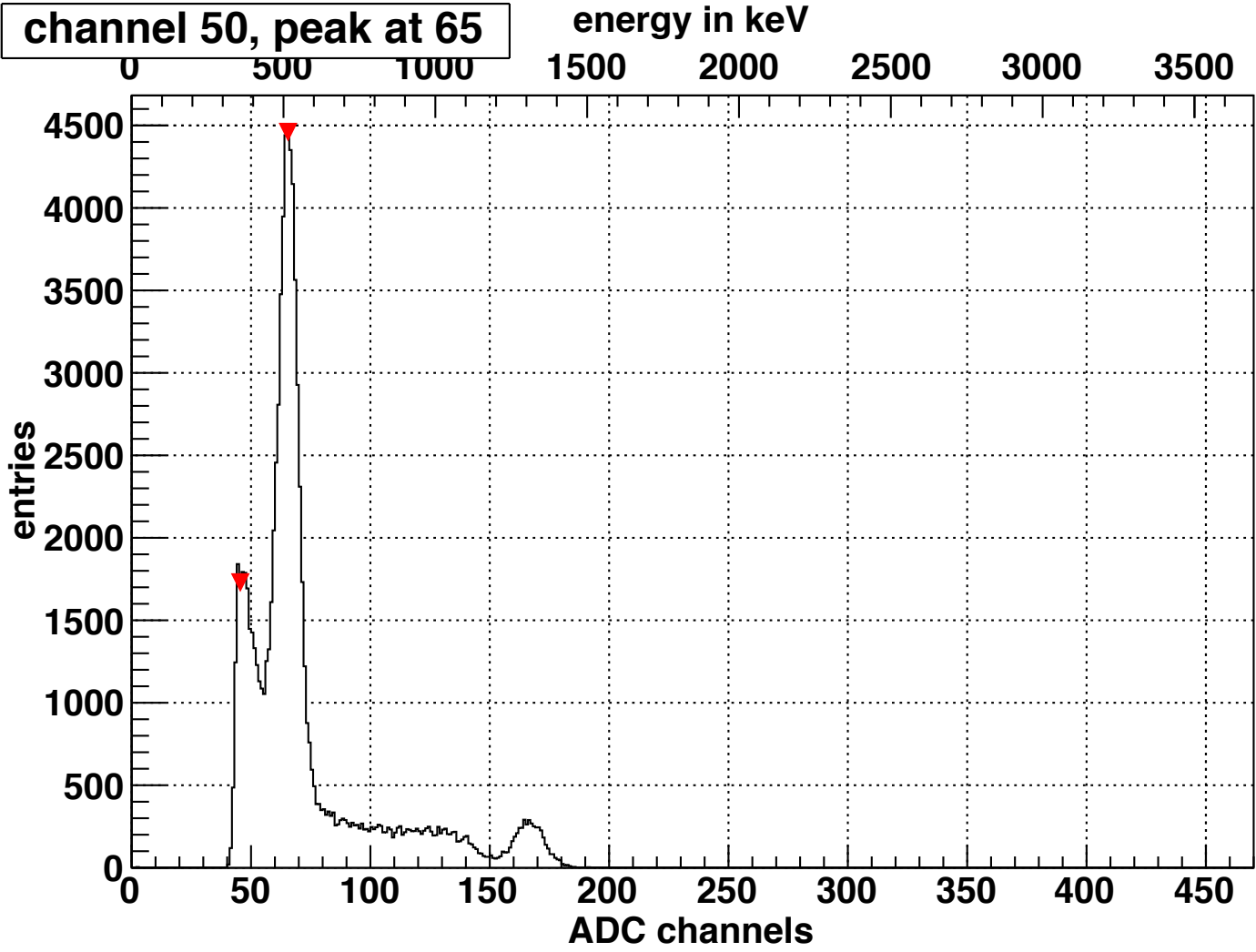


channel 49, peak at 86

energy in keV

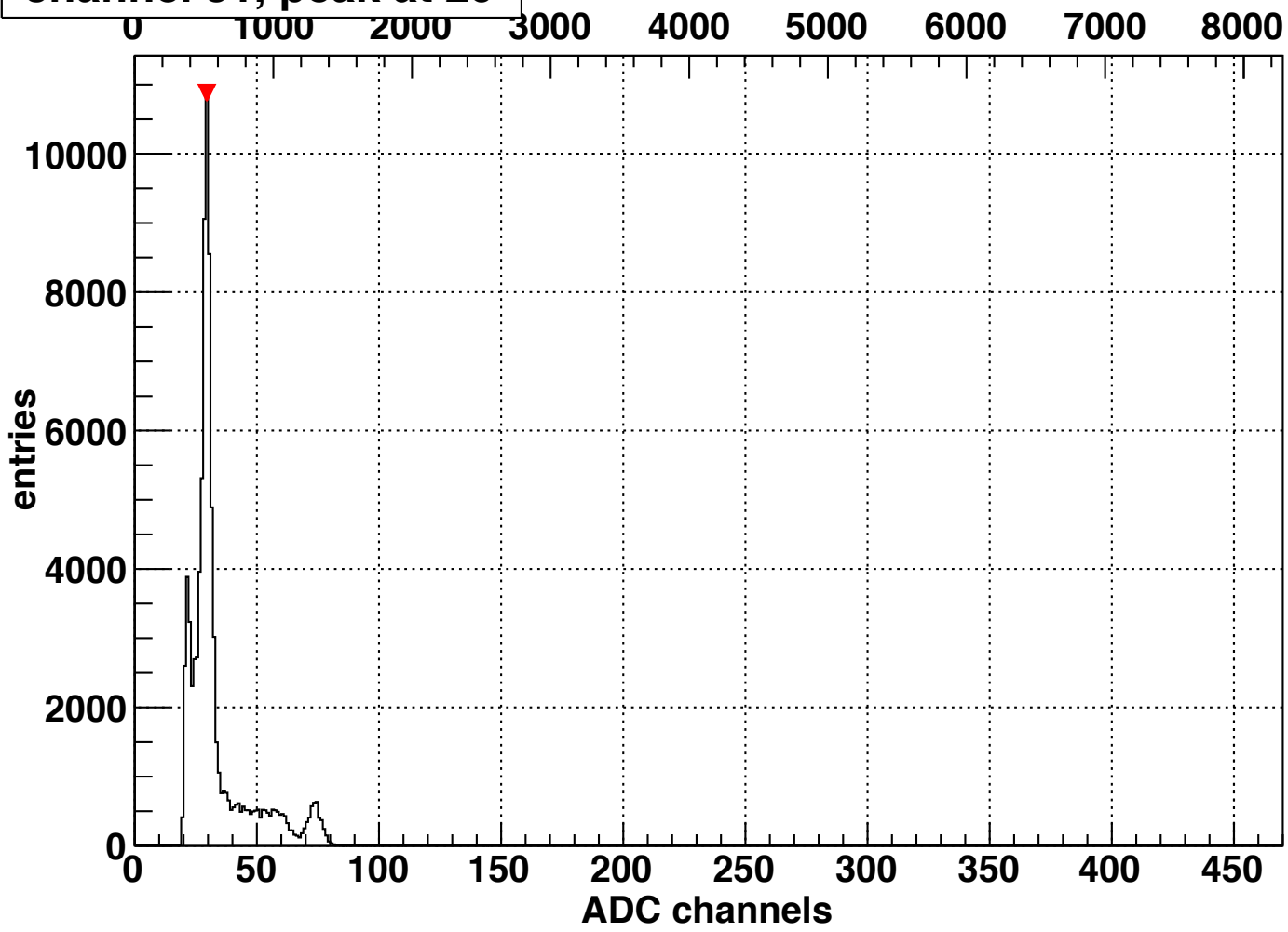


channel 50, peak at 65



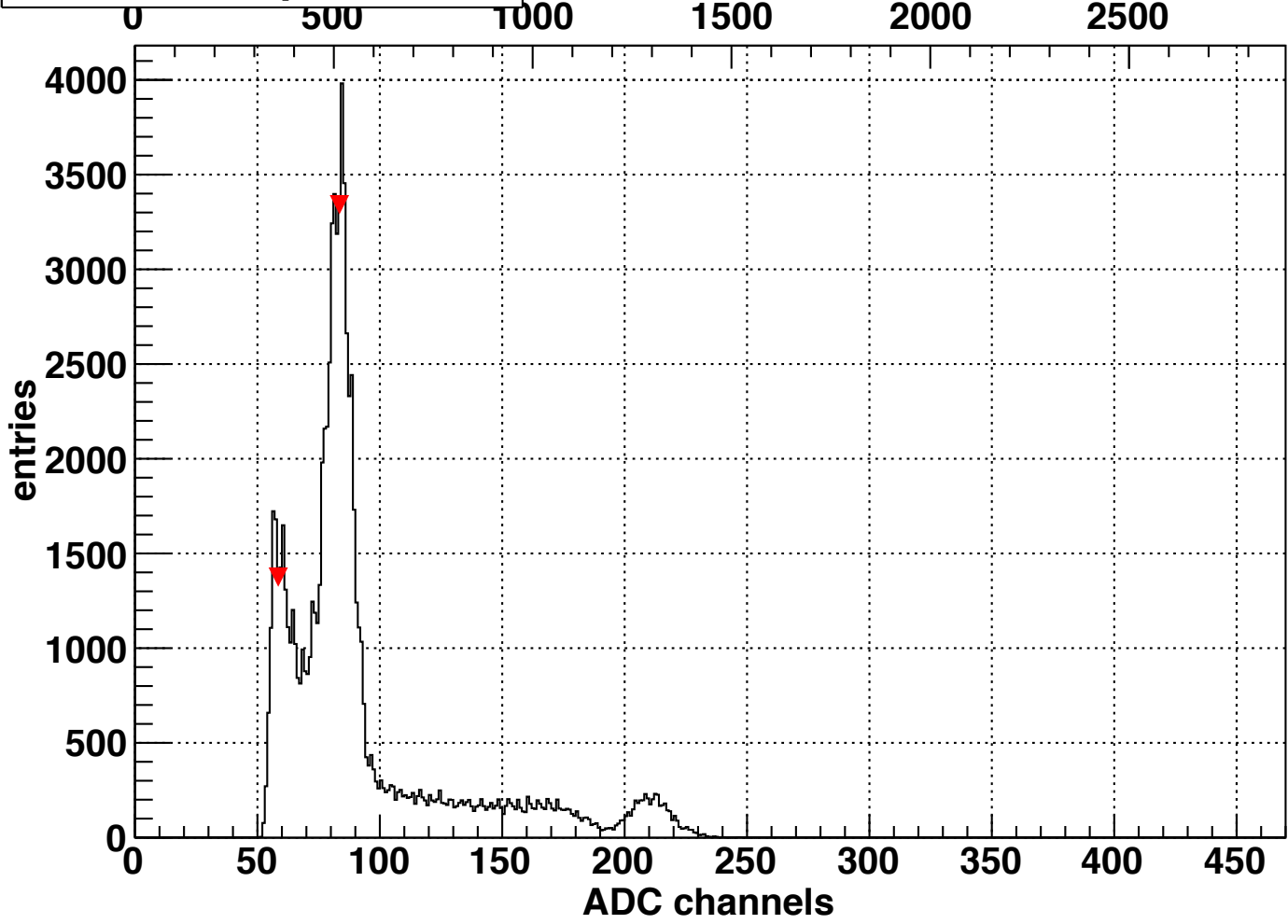
channel 51, peak at 29

energy in keV



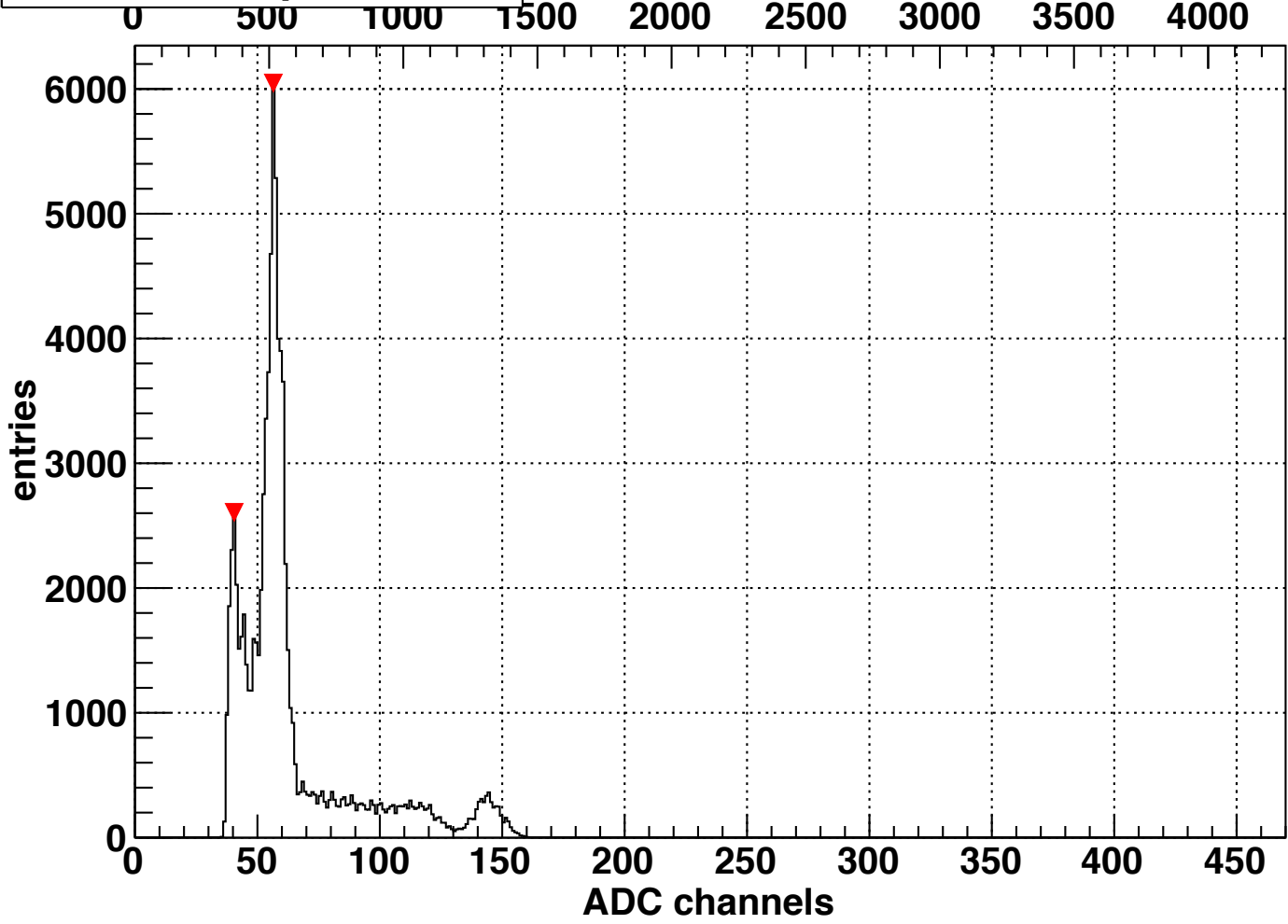
channel 52, peak at 83

energy in keV

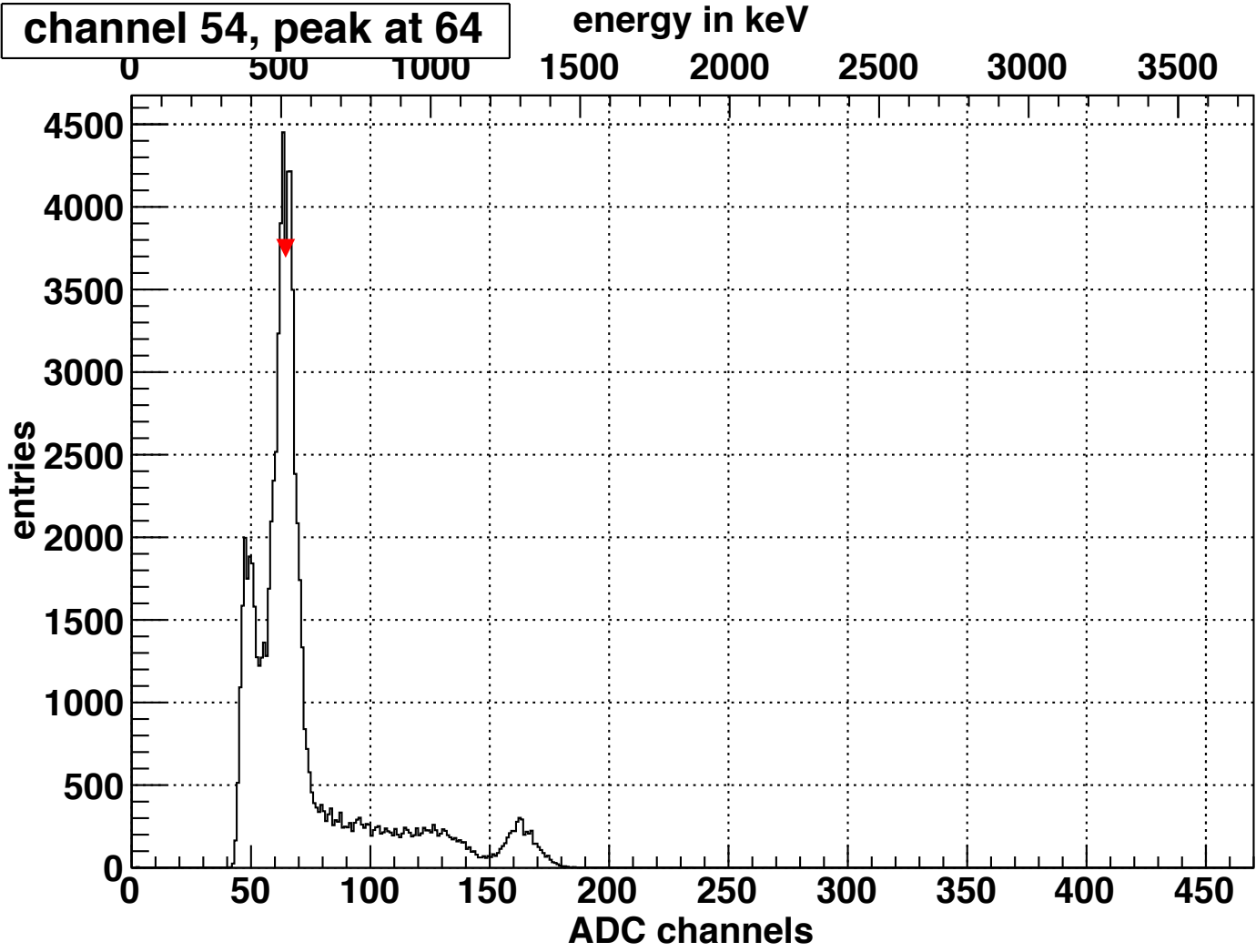


channel 53, peak at 56

energy in keV



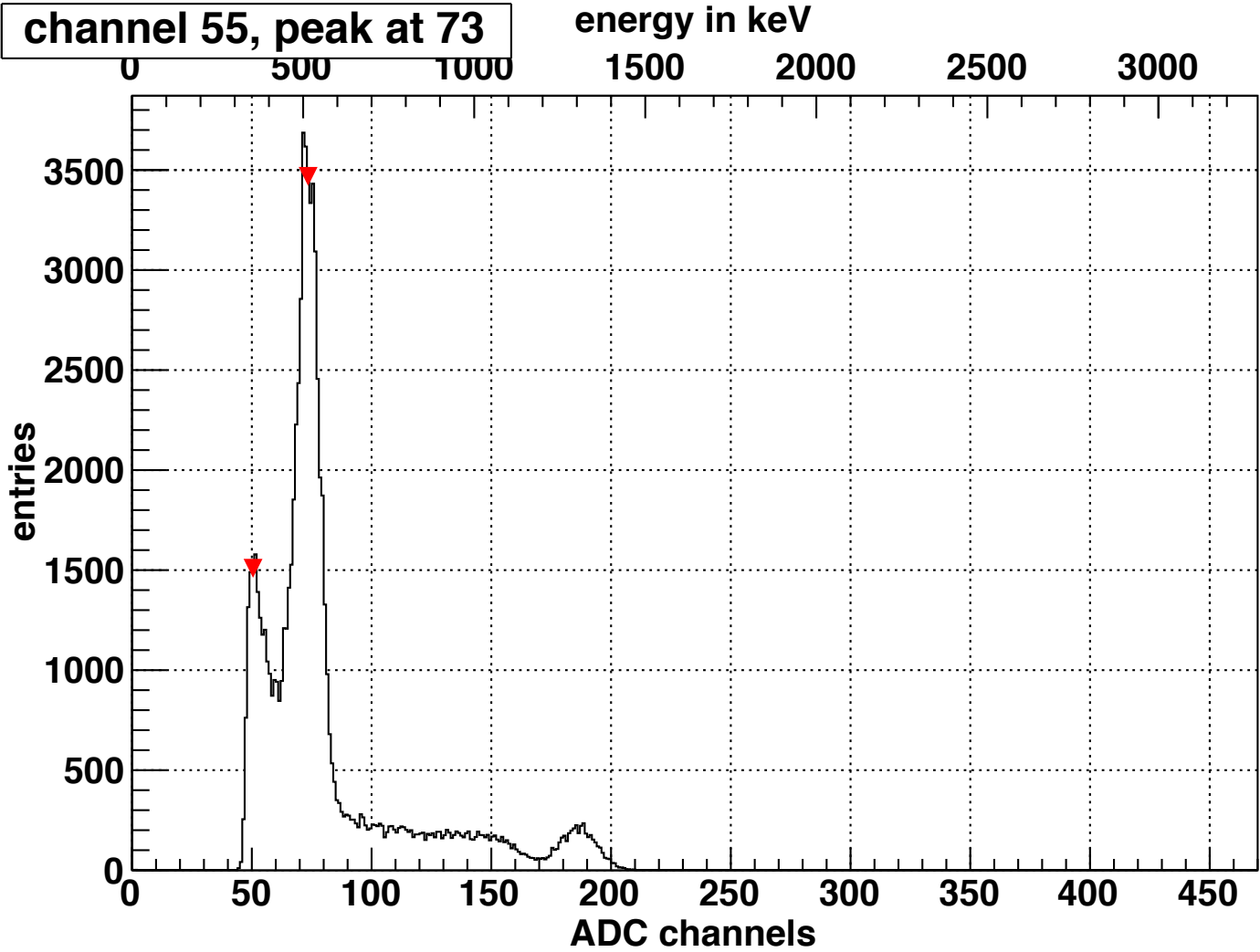
channel 54, peak at 64



energy in keV

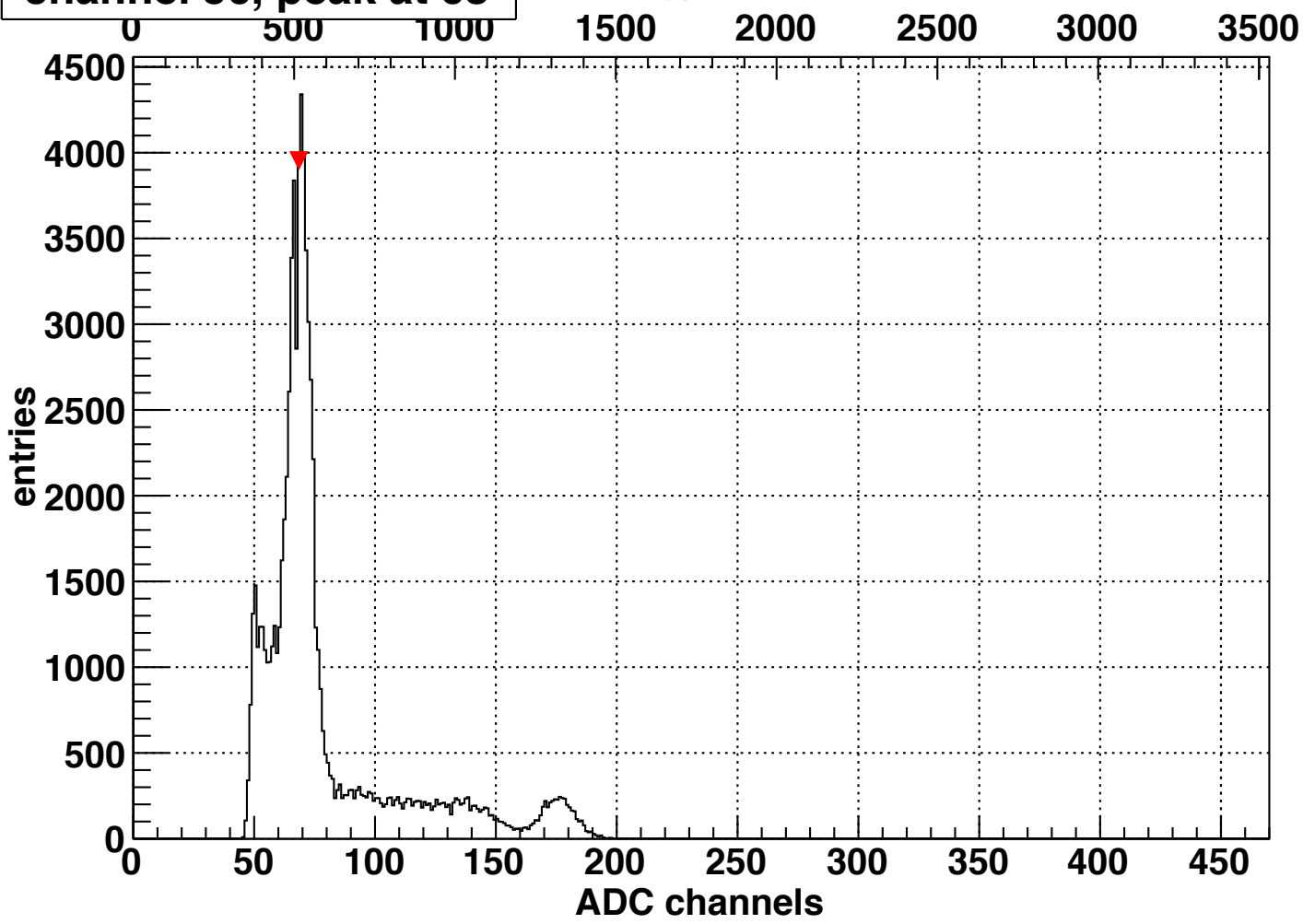
0 500 1000 1500 2000 2500 3000 3500

channel 55, peak at 73



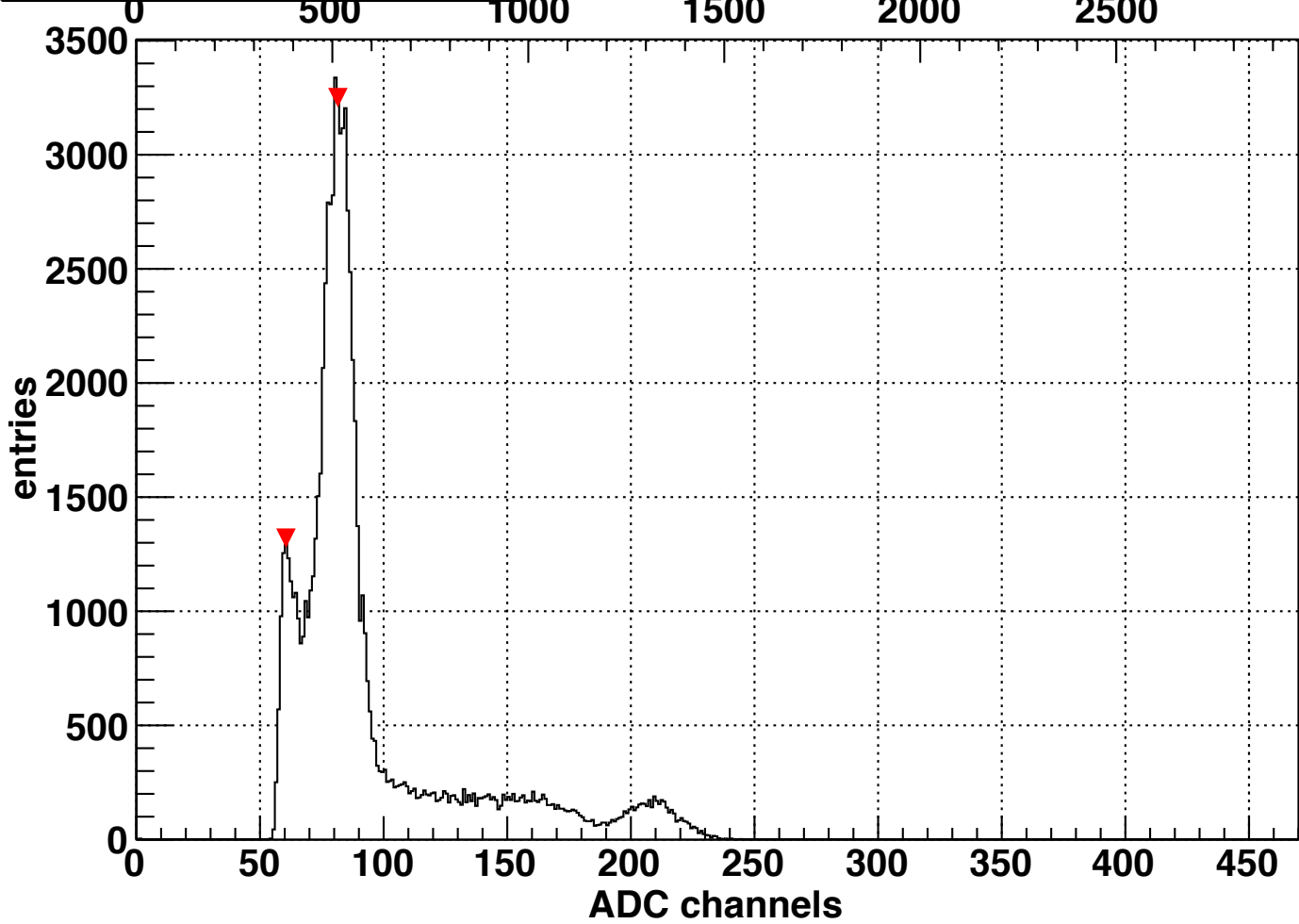
channel 56, peak at 68

energy in keV



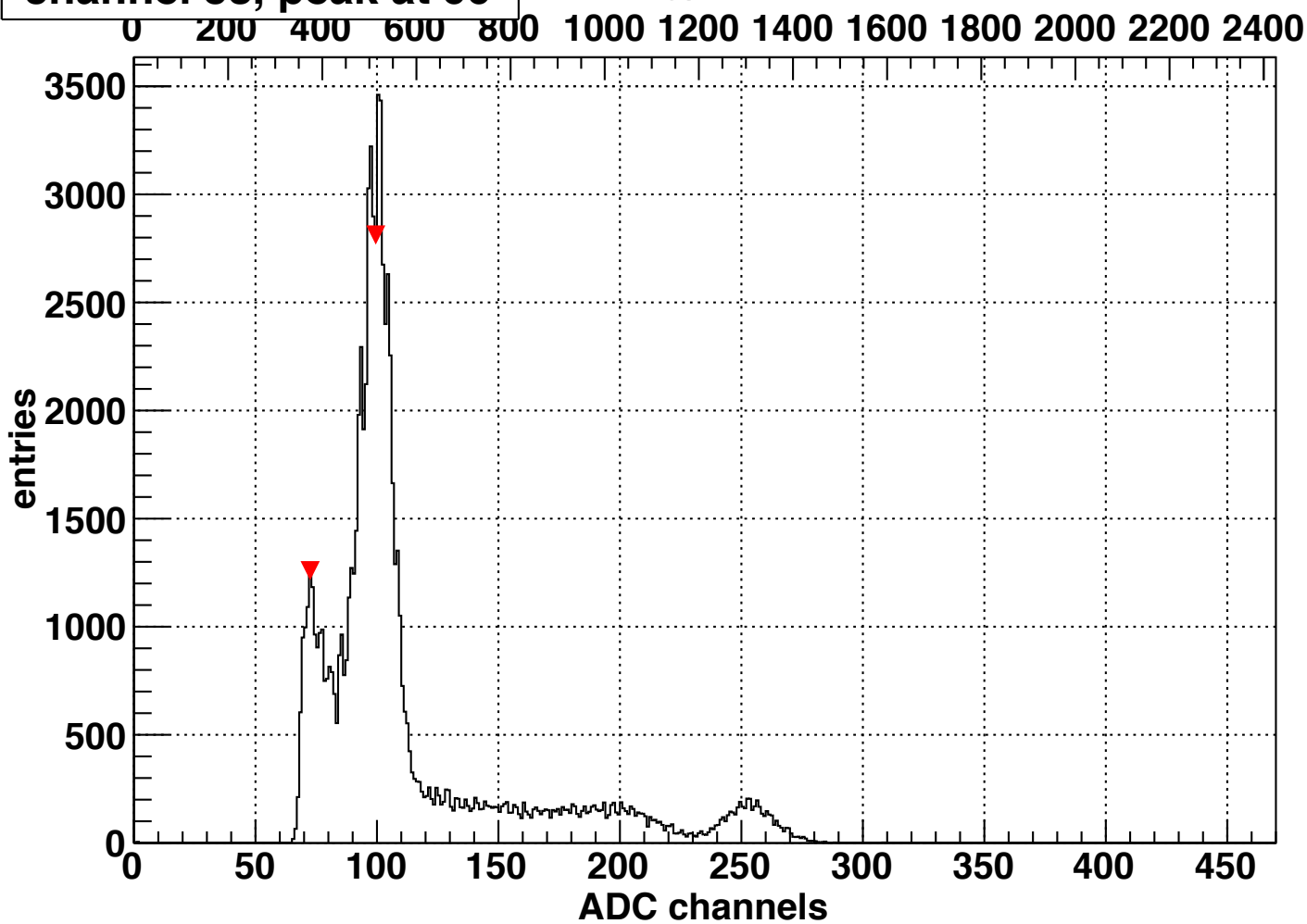
channel 57, peak at 81

energy in keV

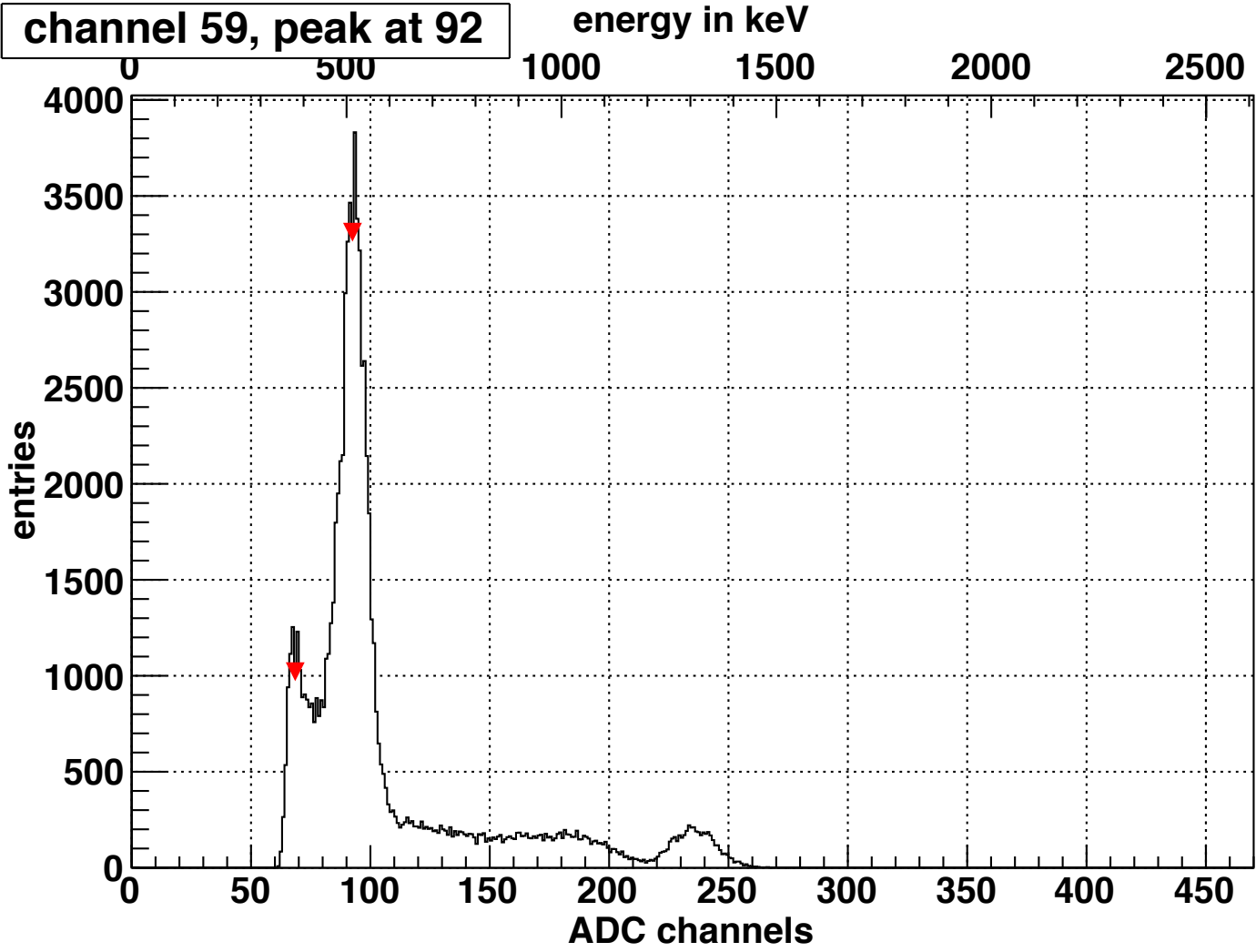


channel 58, peak at 99

energy in keV

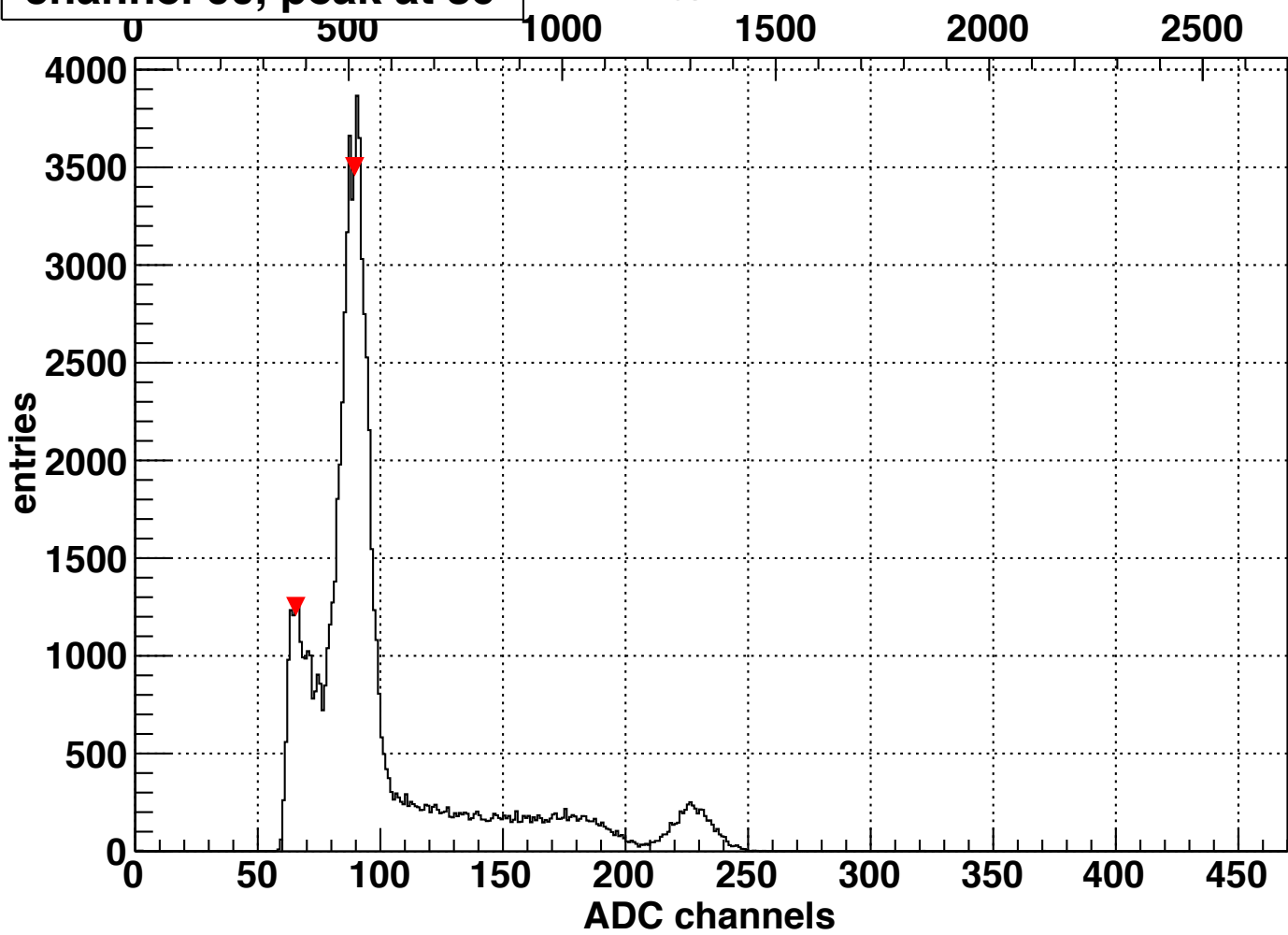


channel 59, peak at 92



channel 60, peak at 89

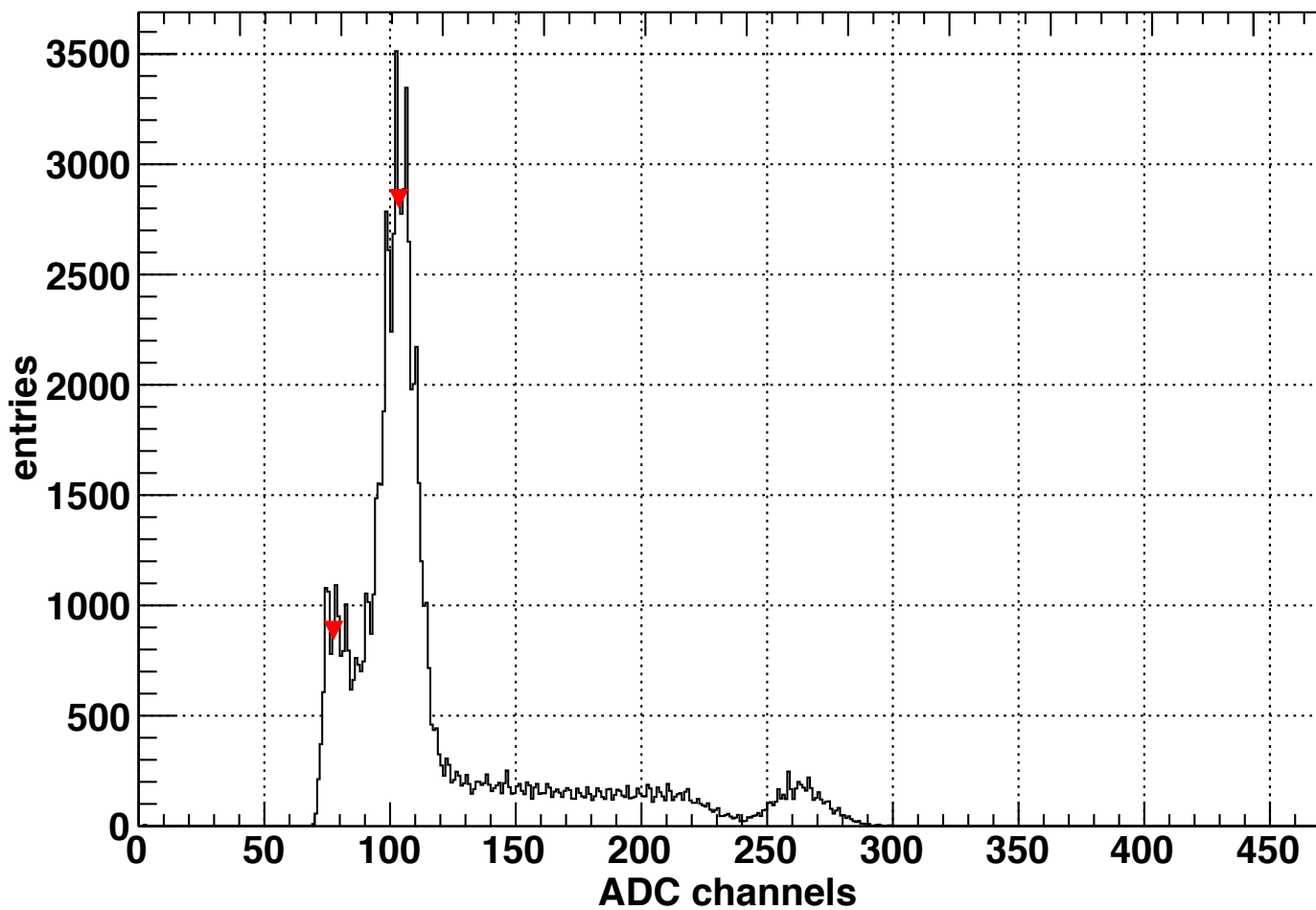
energy in keV



channel 61, peak at 103

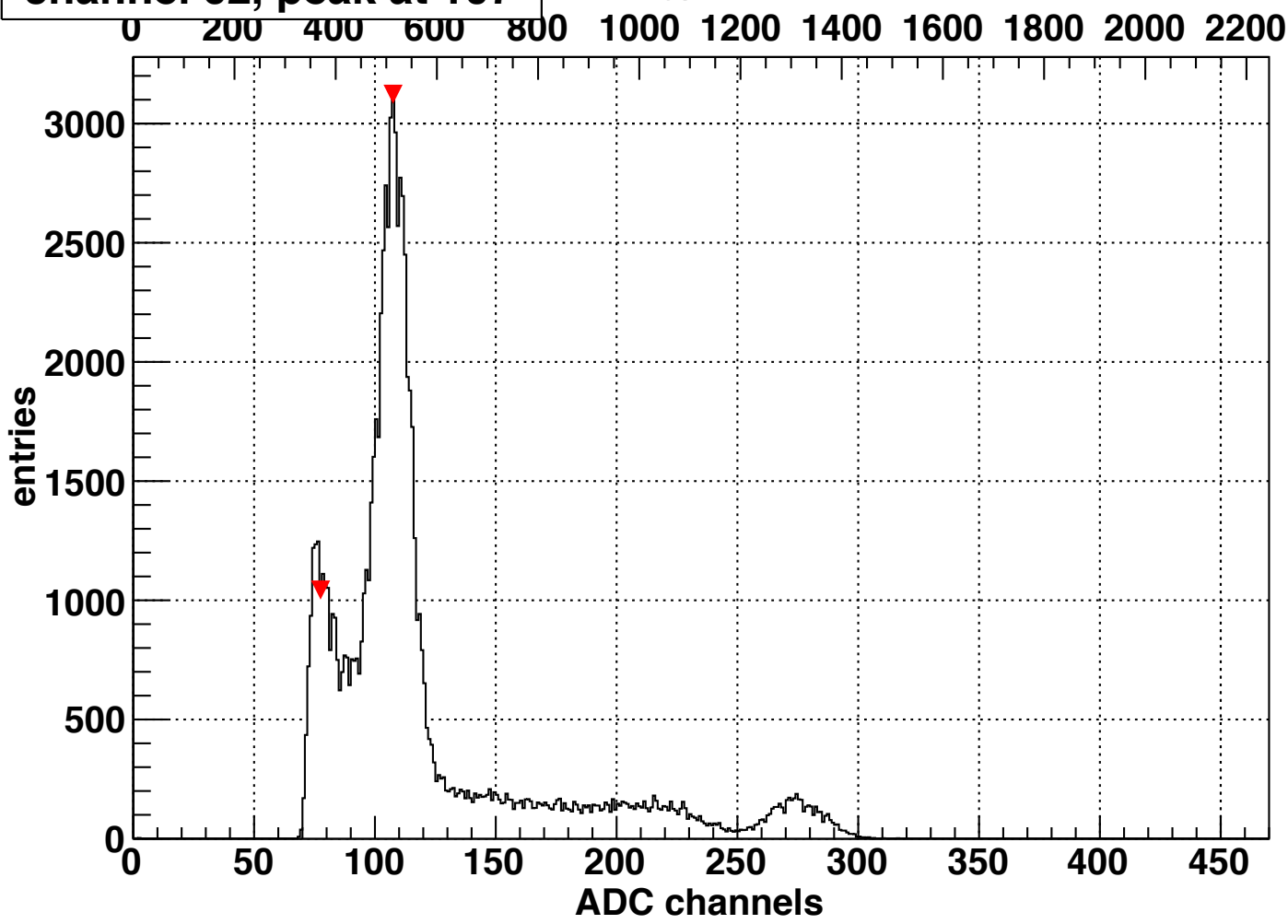
energy in keV

0 200 400 600 800 1000 1200 1400 1600 1800 2000 2200

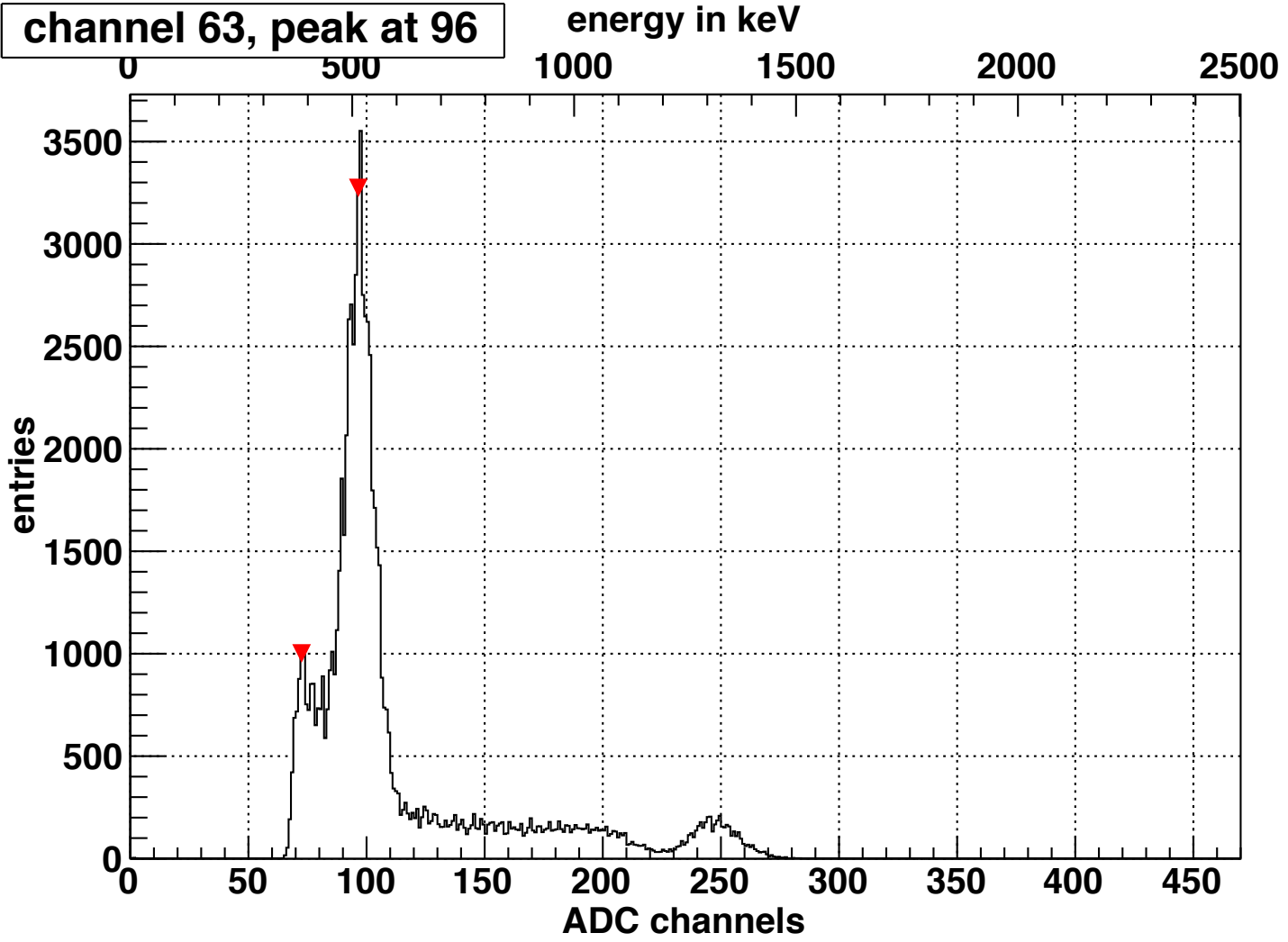


channel 62, peak at 107

energy in keV

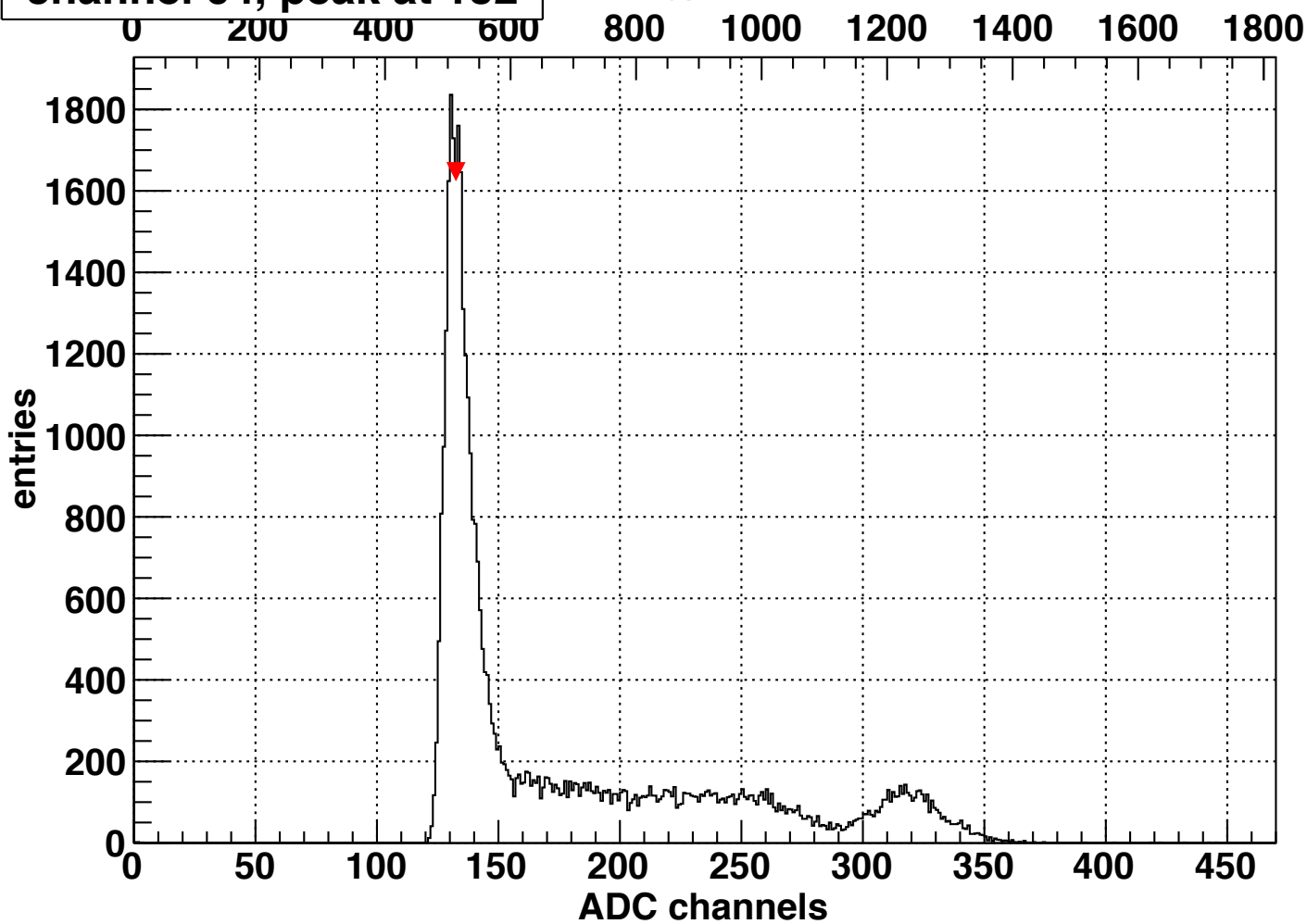


channel 63, peak at 96



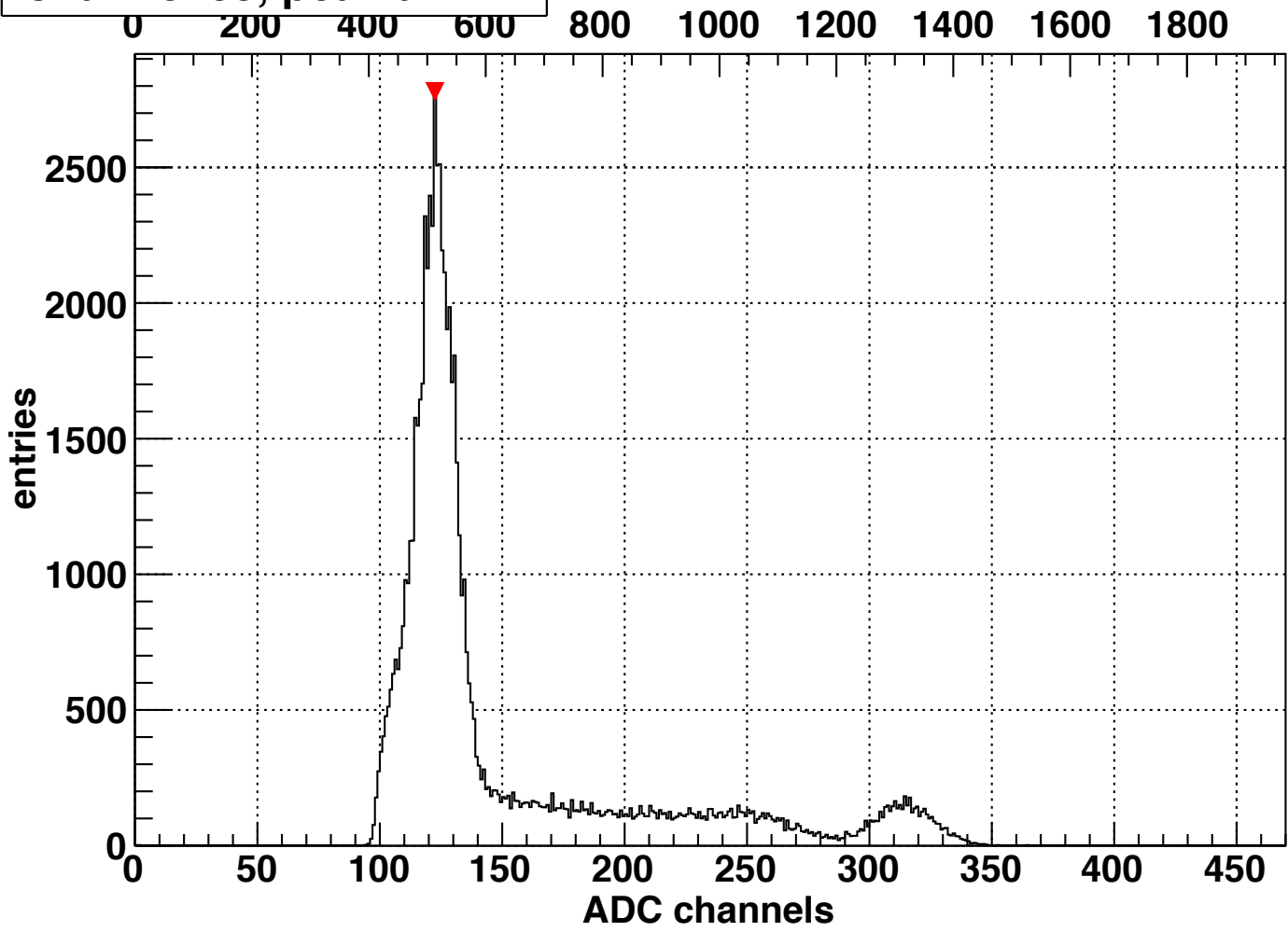
channel 64, peak at 132

energy in keV



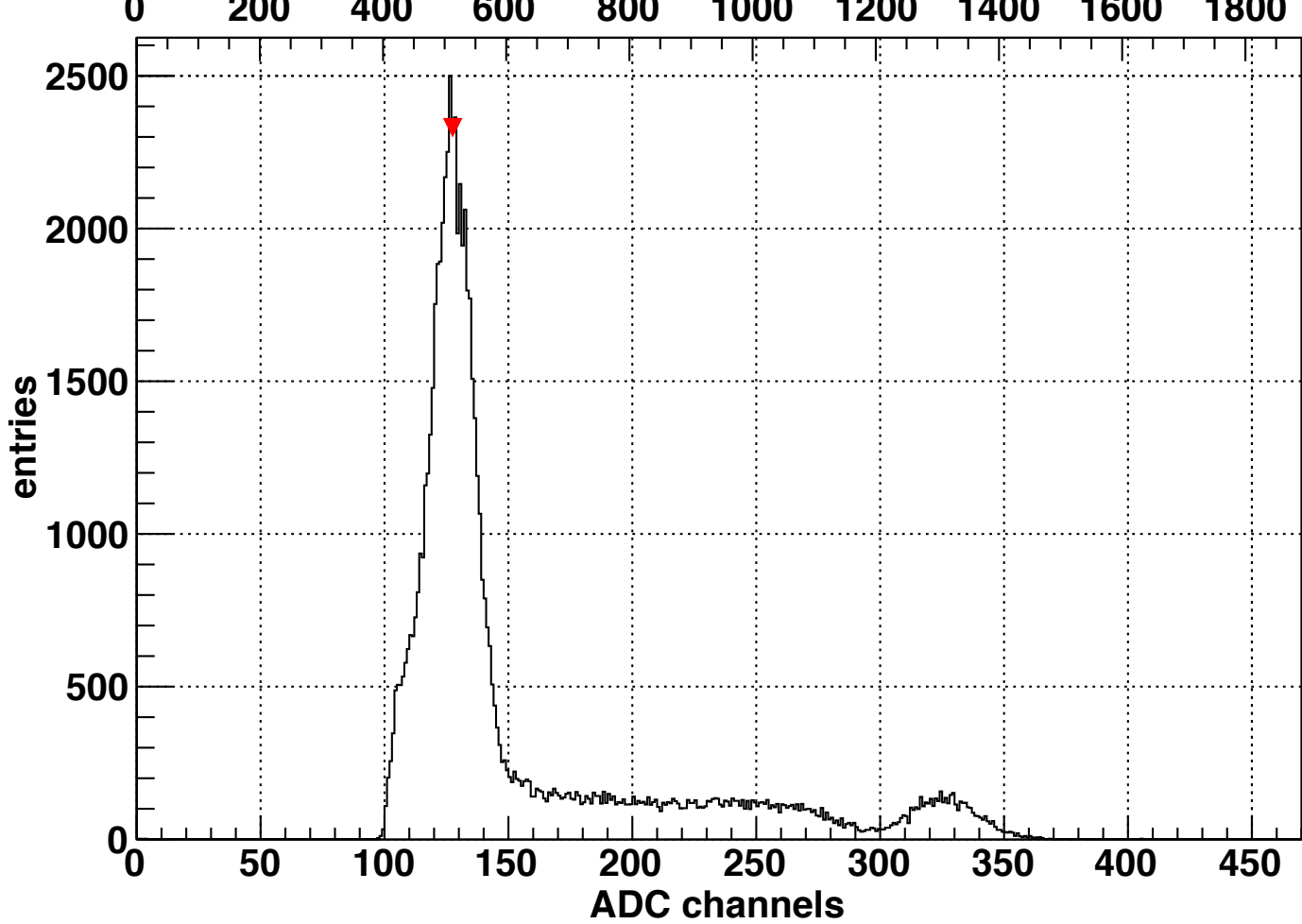
channel 65, peak at 122

energy in keV



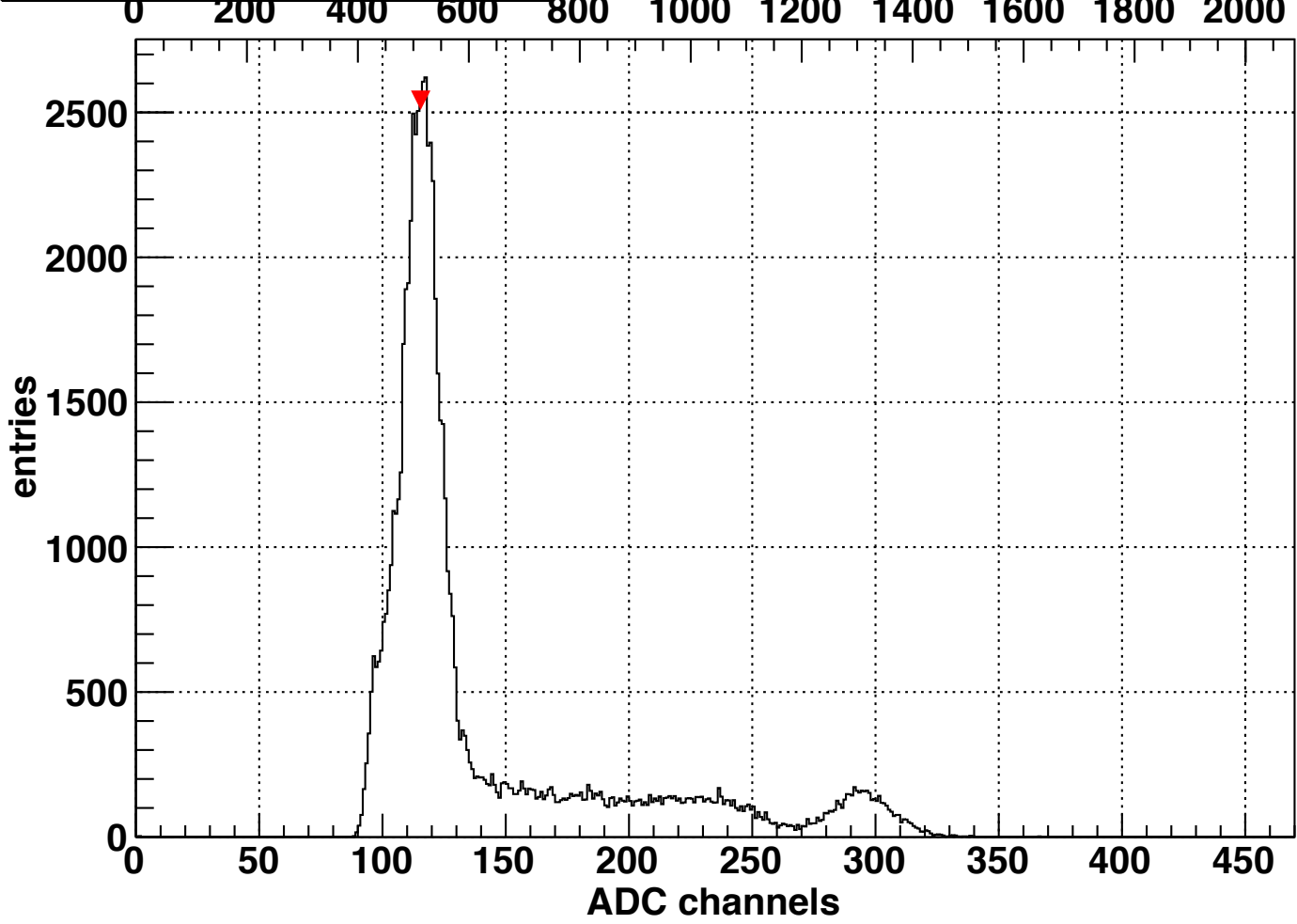
channel 66, peak at 127

energy in keV



channel 67, peak at 115

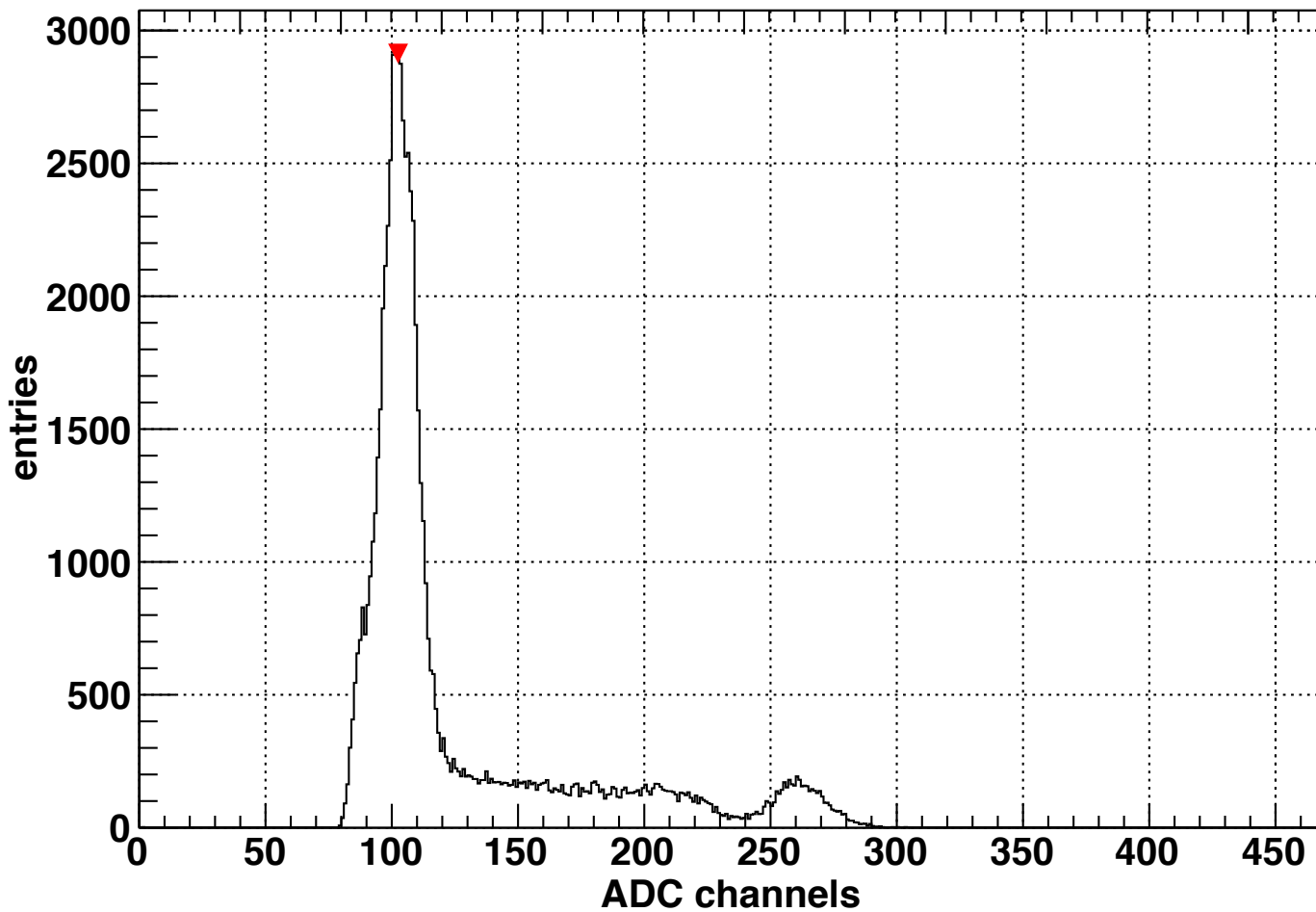
energy in keV



channel 68, peak at 102

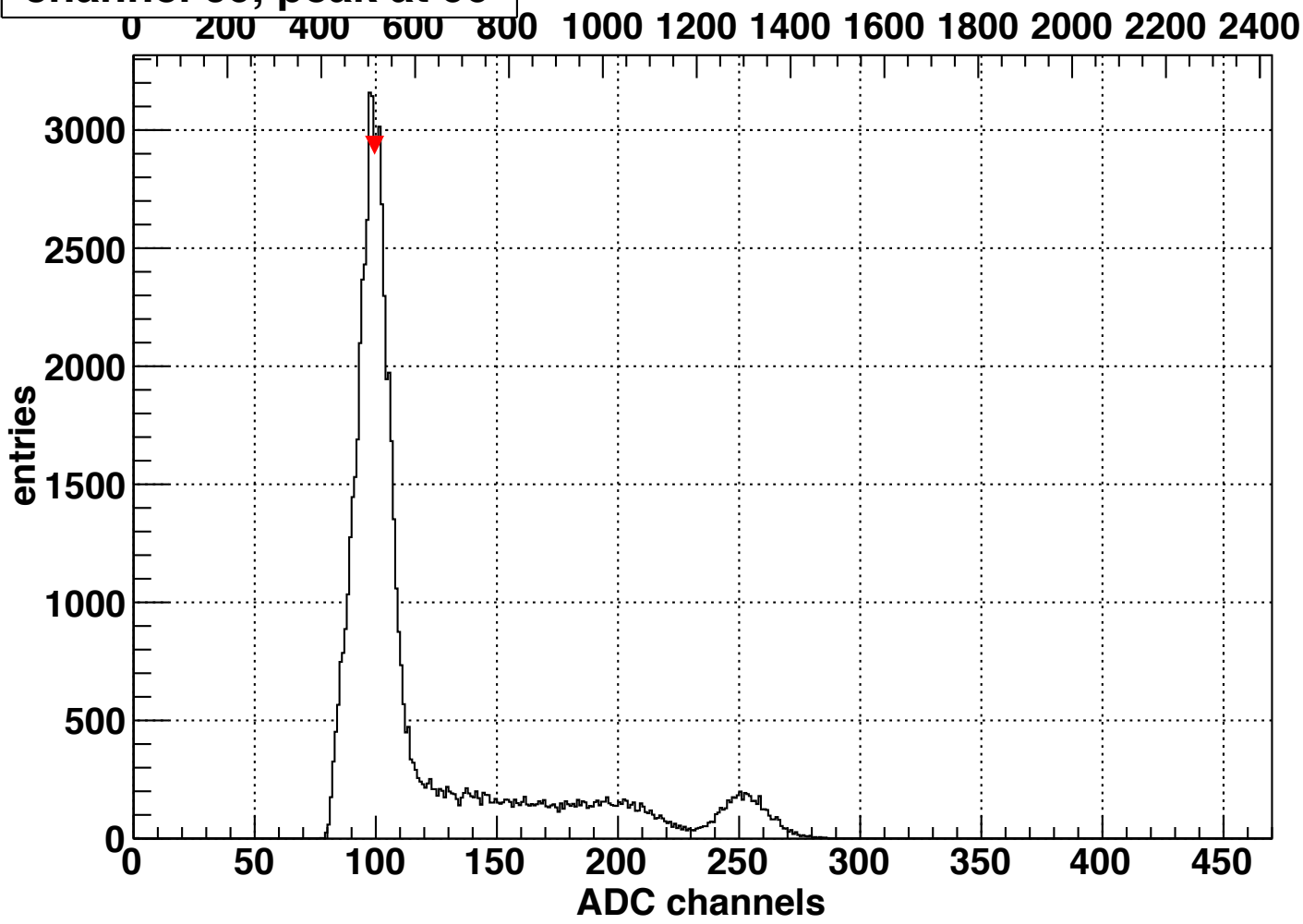
energy in keV

0 200 400 600 800 1000 1200 1400 1600 1800 2000 2200



channel 69, peak at 99

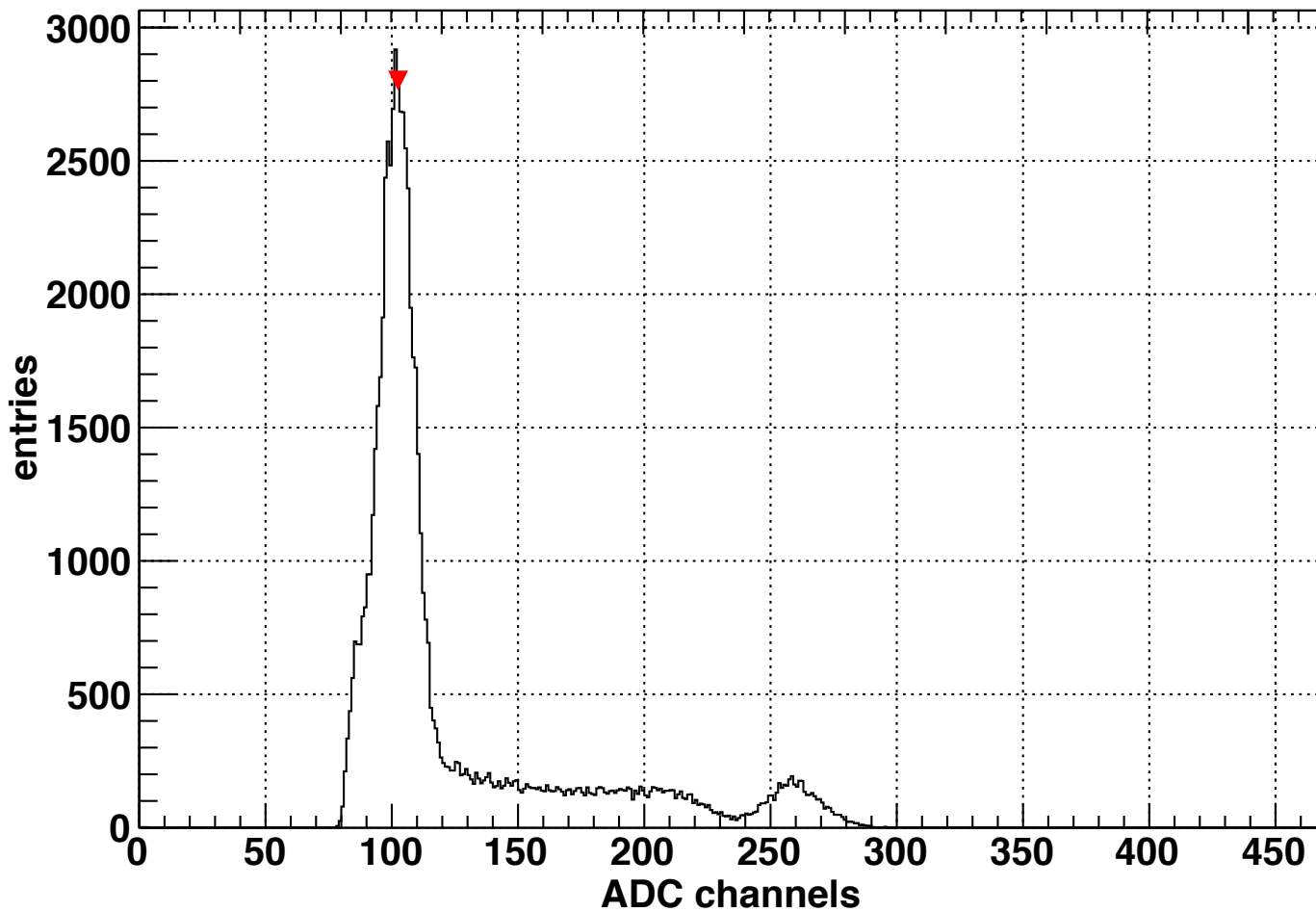
energy in keV



channel 70, peak at 102

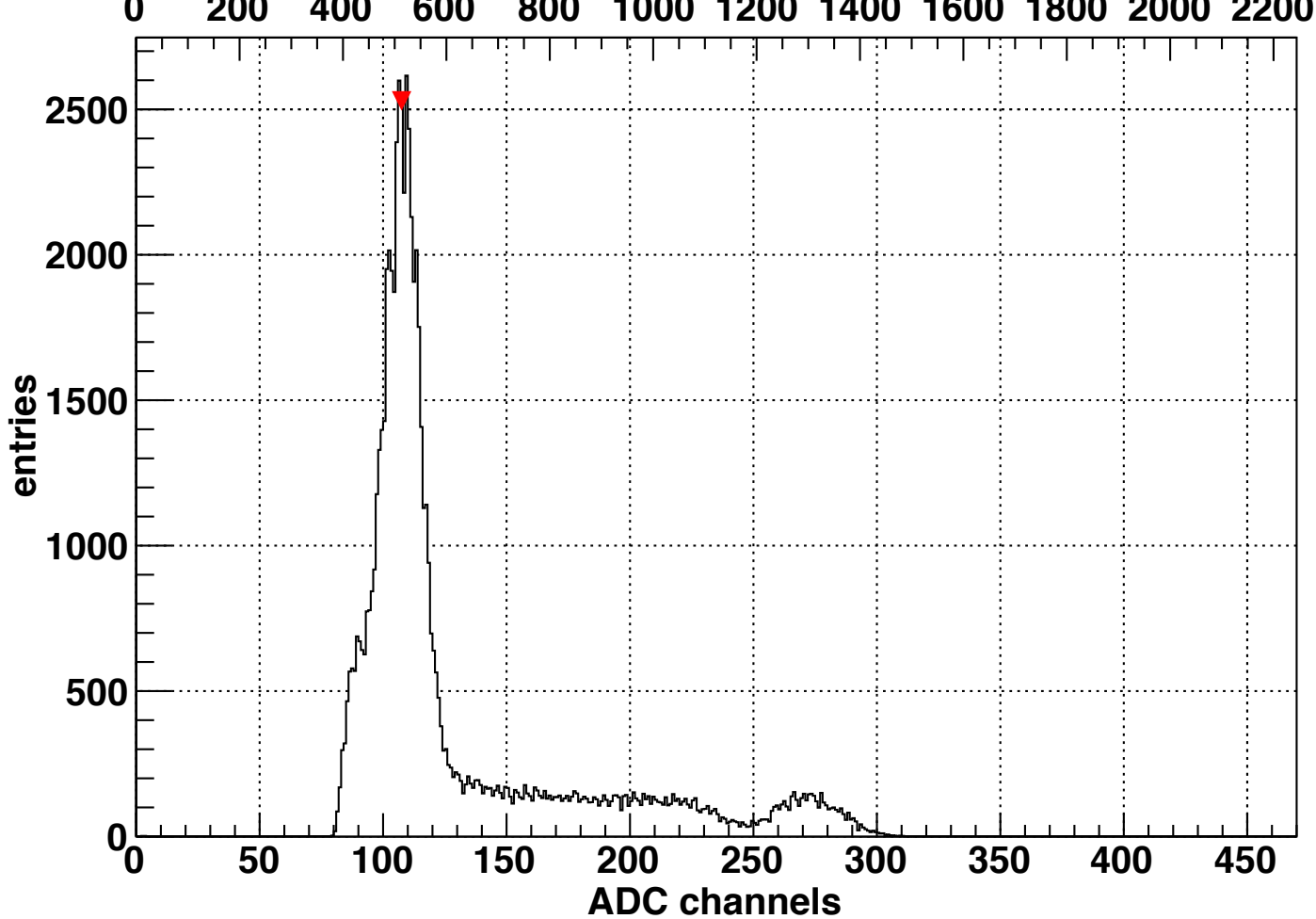
energy in keV

0 200 400 600 800 1000 1200 1400 1600 1800 2000 2200

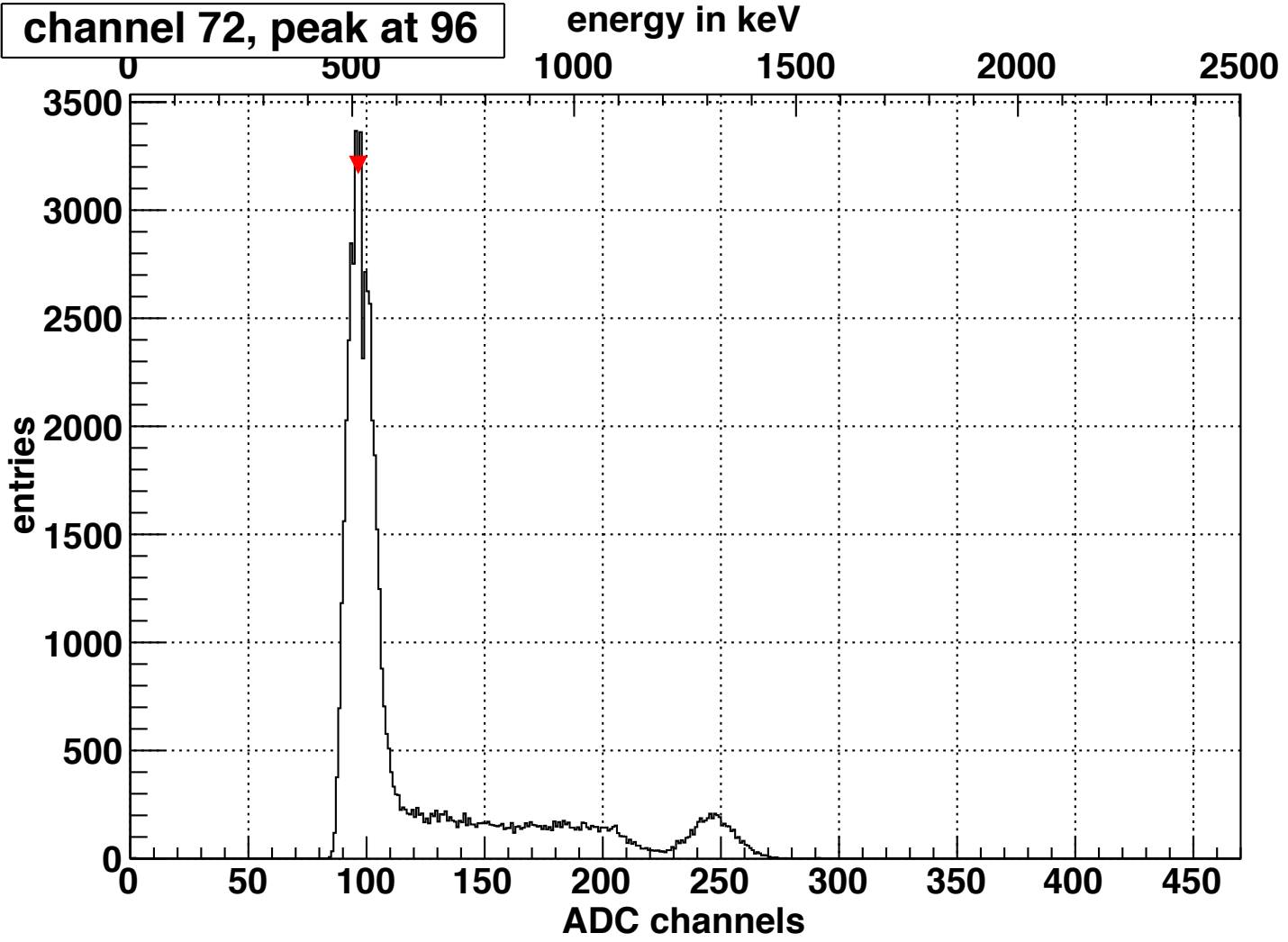


channel 71, peak at 107

energy in keV



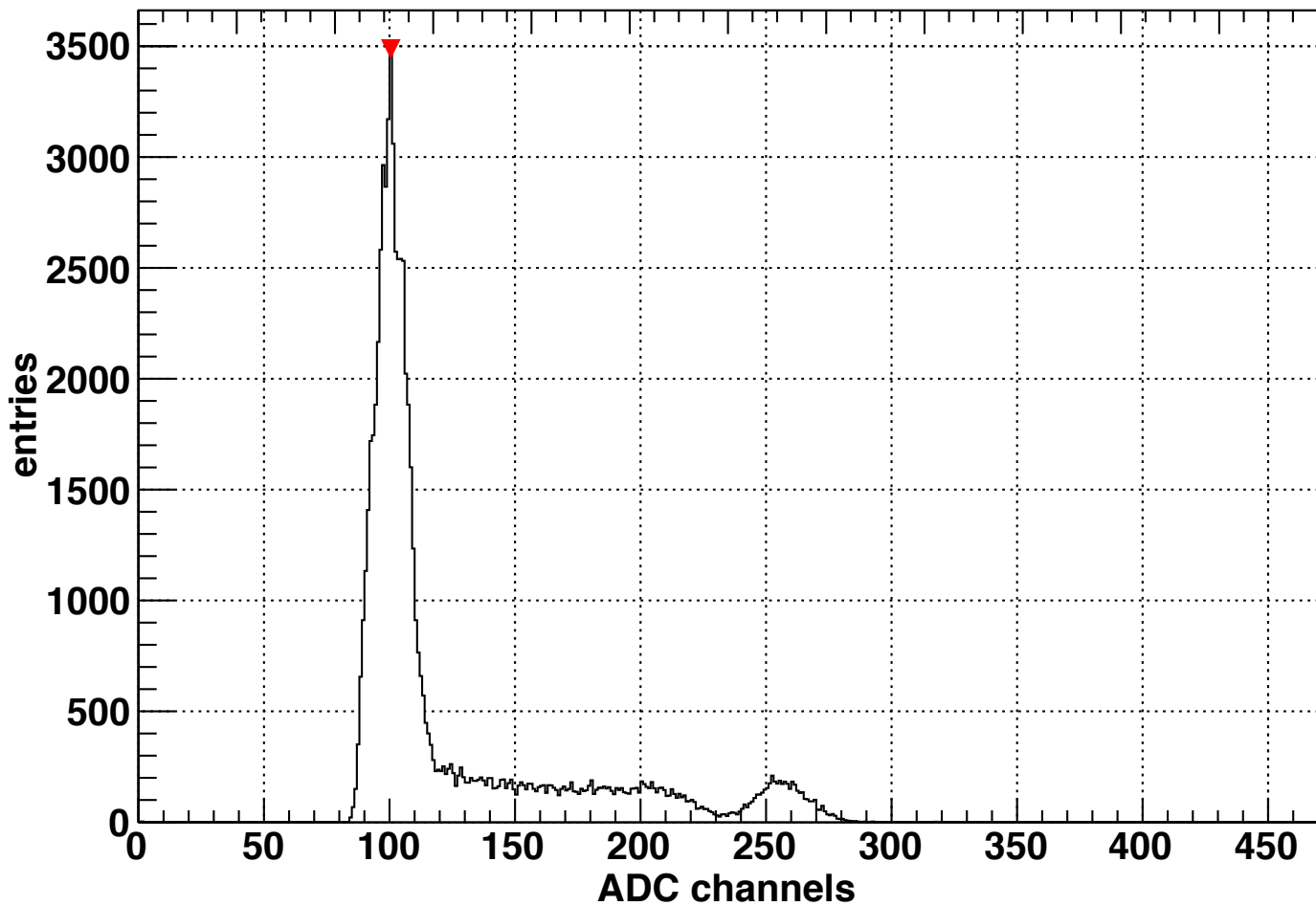
channel 72, peak at 96



channel 73, peak at 100

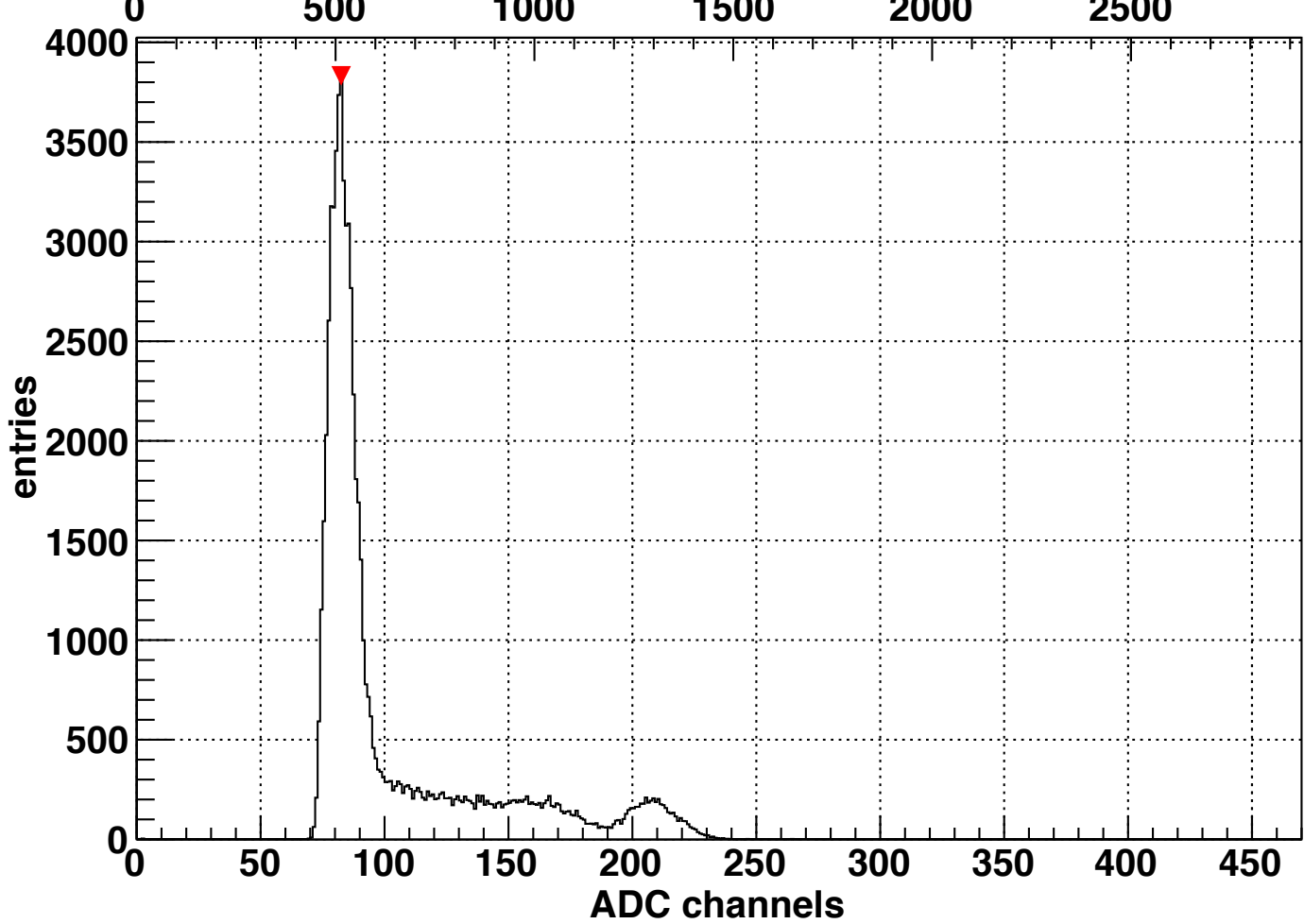
energy in keV

0 200 400 600 800 1000 1200 1400 1600 1800 2000 2200 2400



channel 74, peak at 82

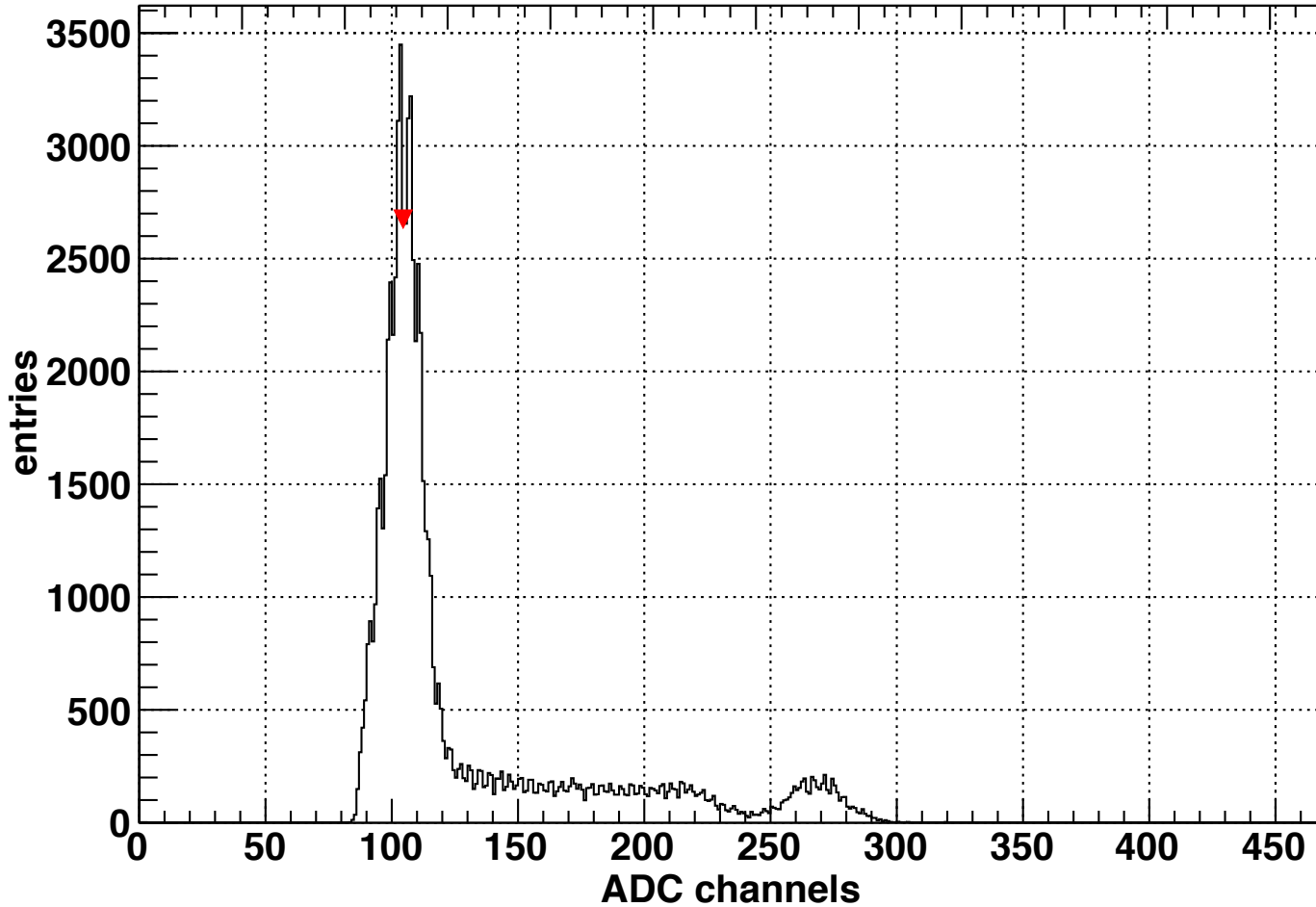
energy in keV



channel 75, peak at 104

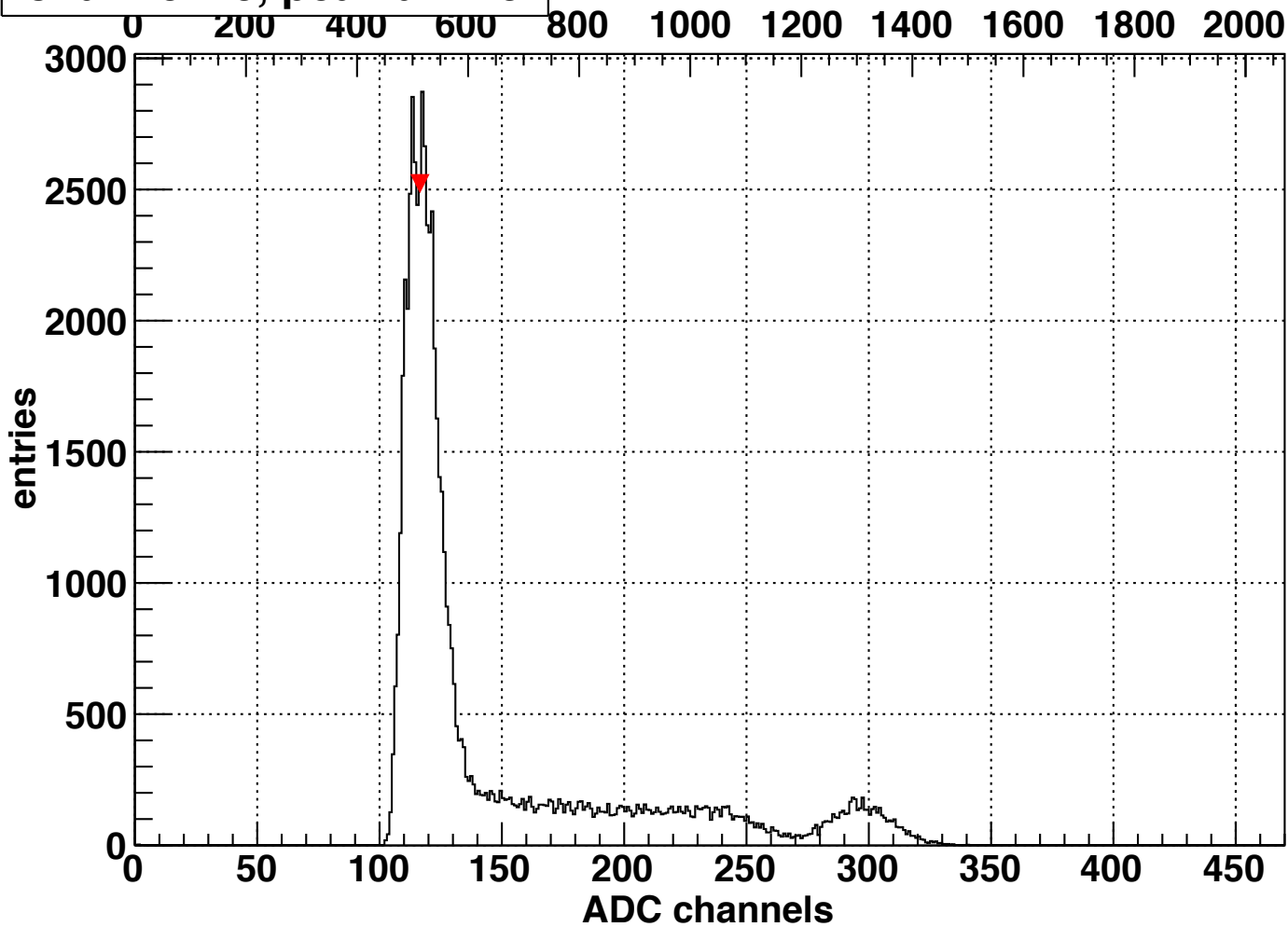
energy in keV

0 200 400 600 800 1000 1200 1400 1600 1800 2000 2200



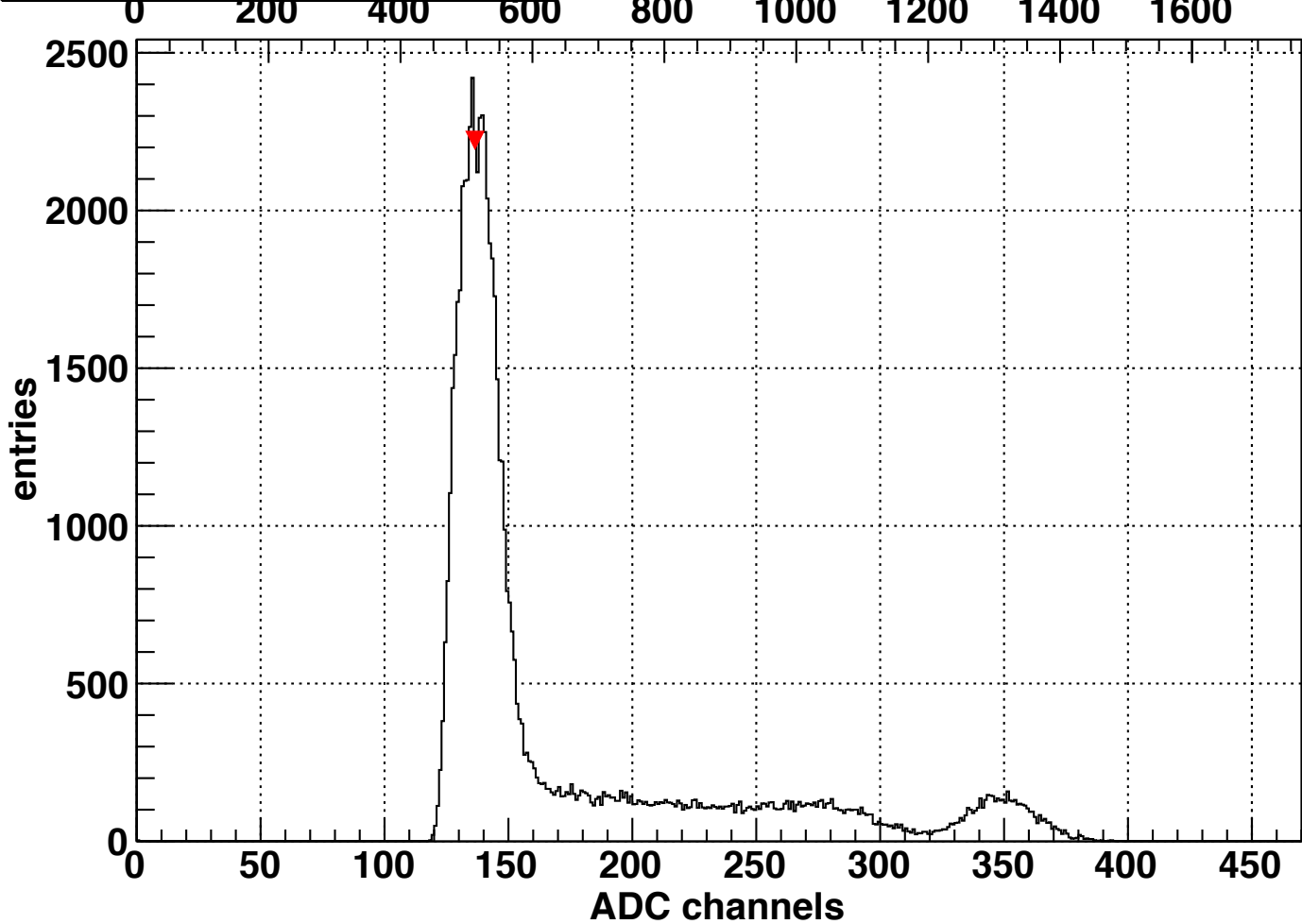
channel 76, peak at 116

energy in keV



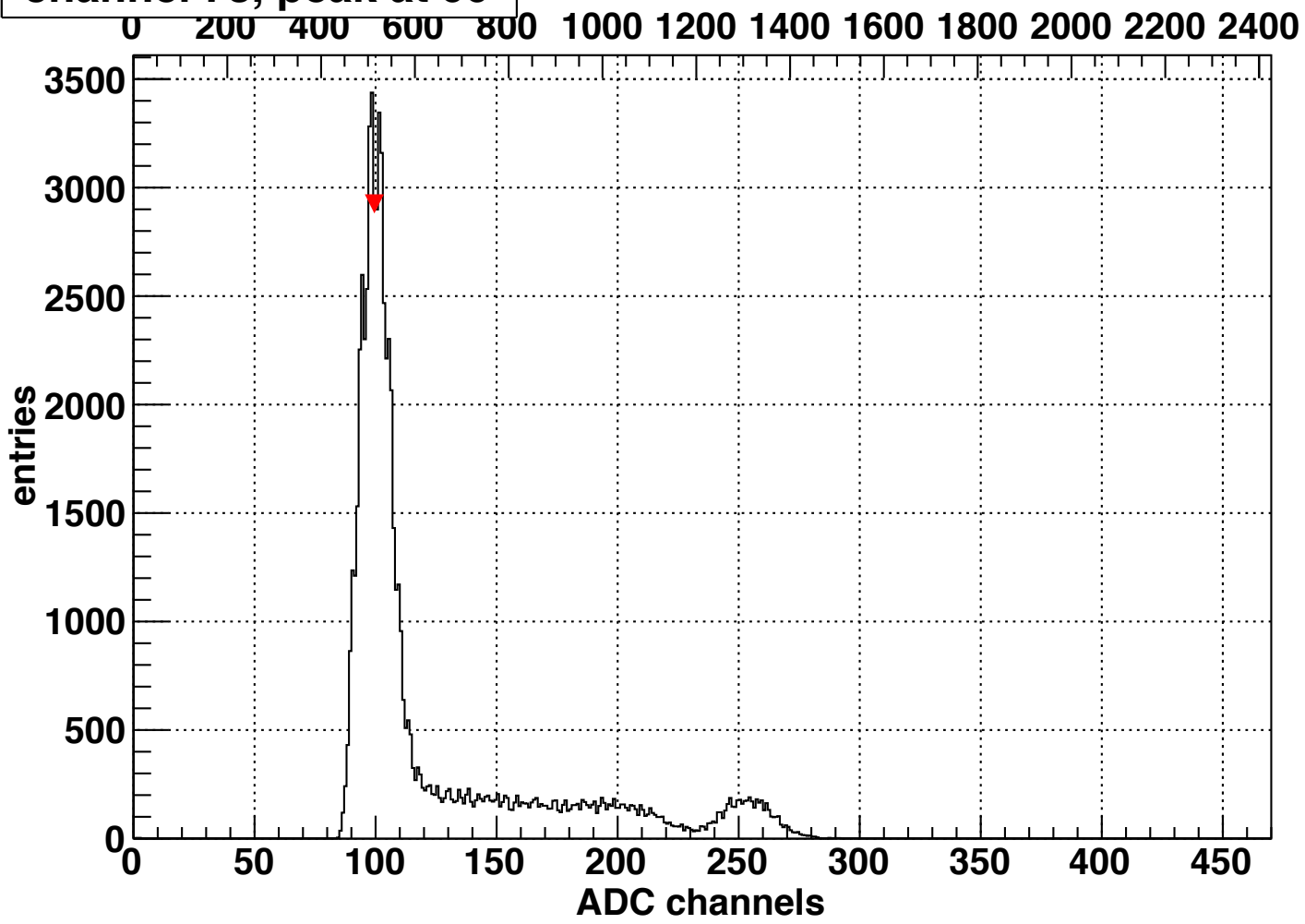
channel 77, peak at 136

energy in keV

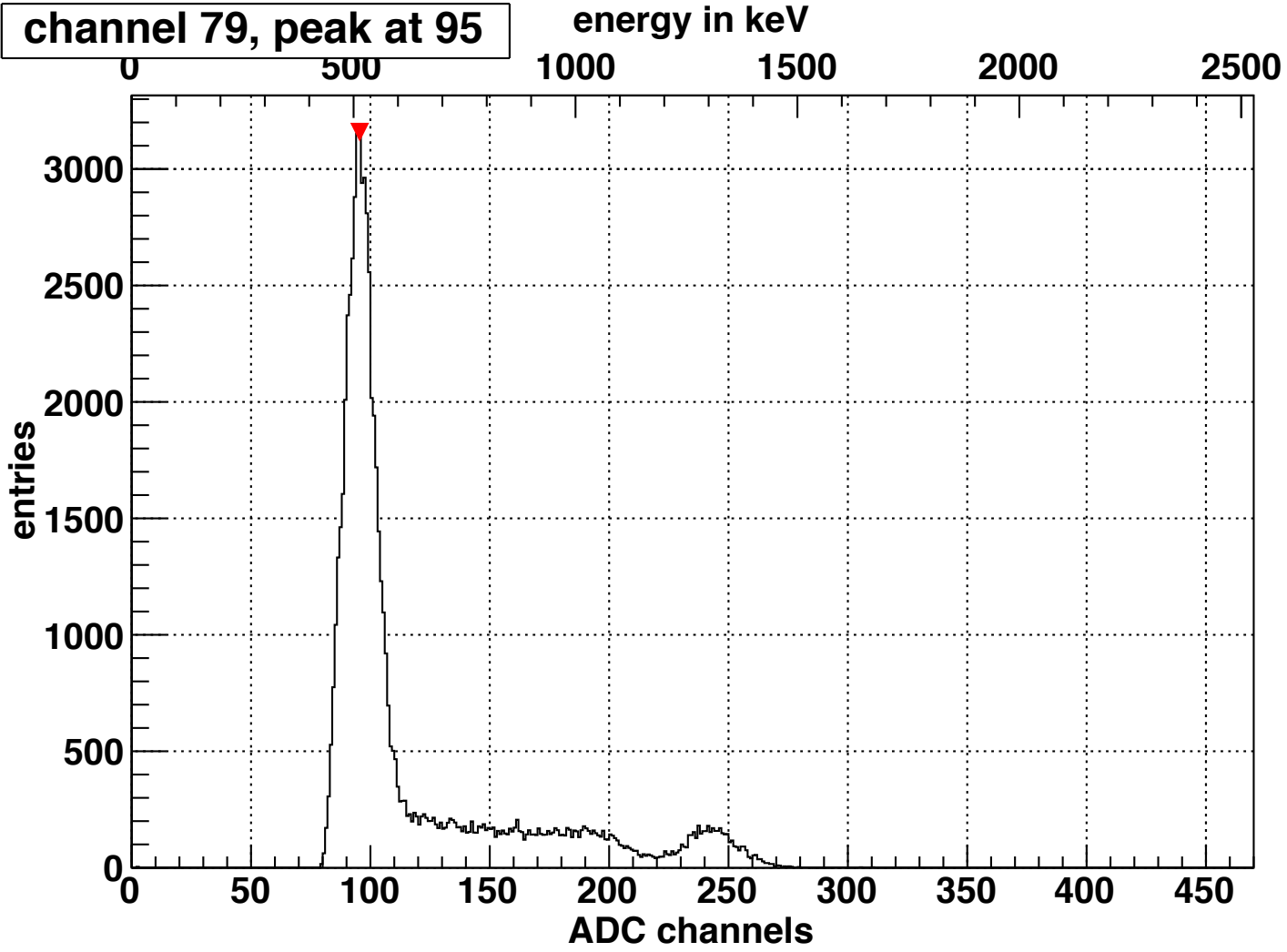


channel 78, peak at 99

energy in keV

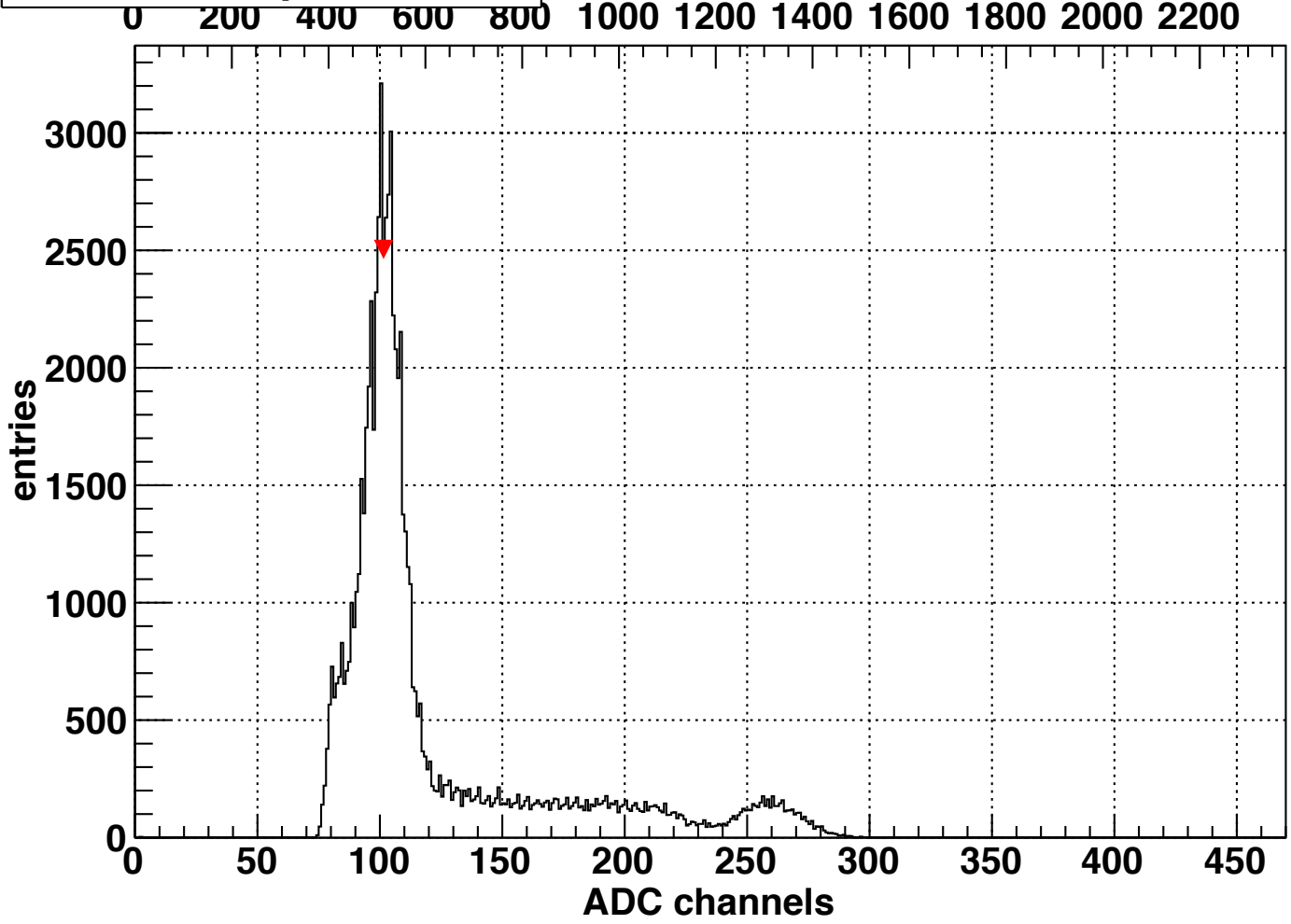


channel 79, peak at 95



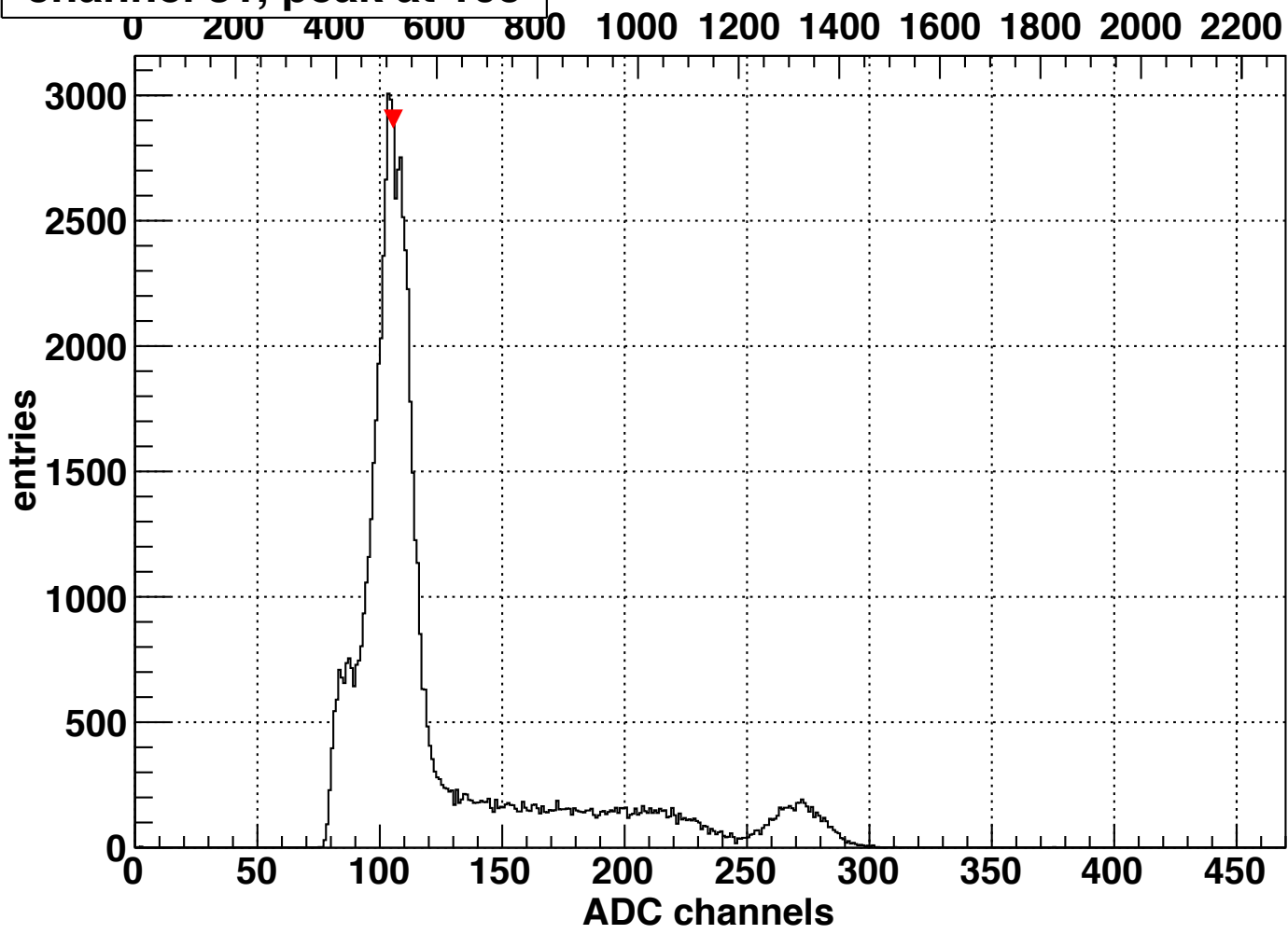
channel 80, peak at 101

energy in keV



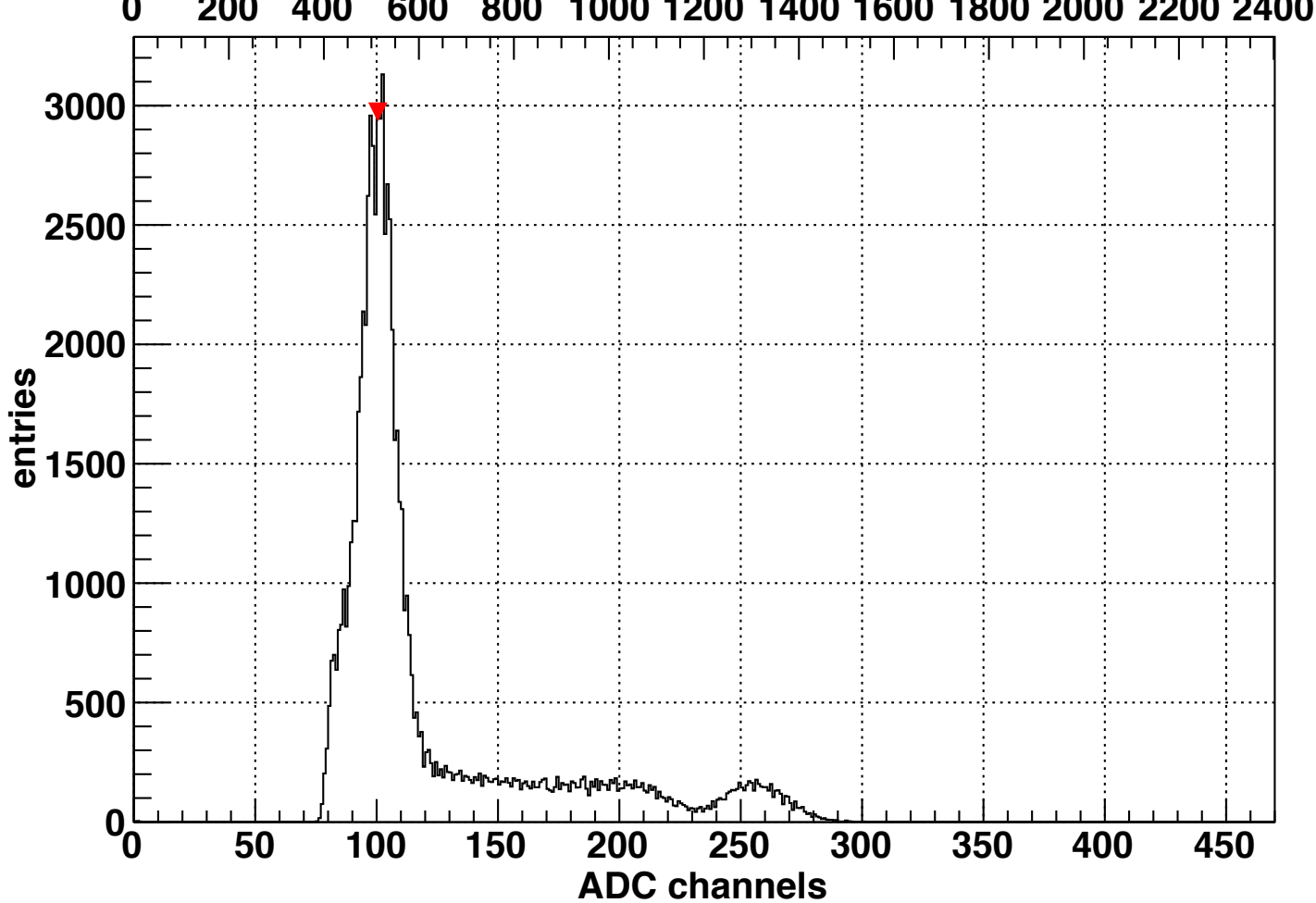
channel 81, peak at 105

energy in keV



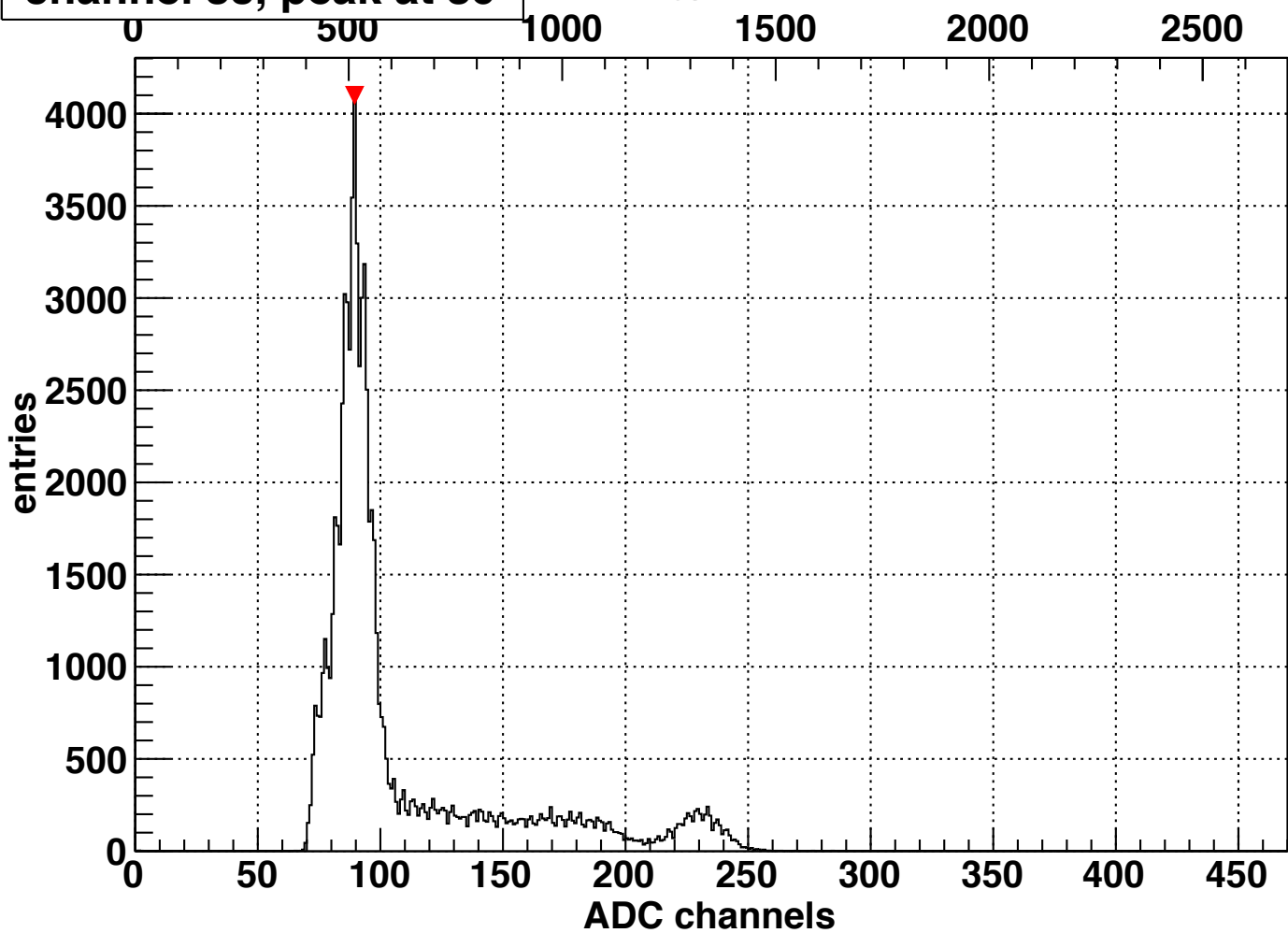
channel 82, peak at 100

energy in keV



channel 83, peak at 89

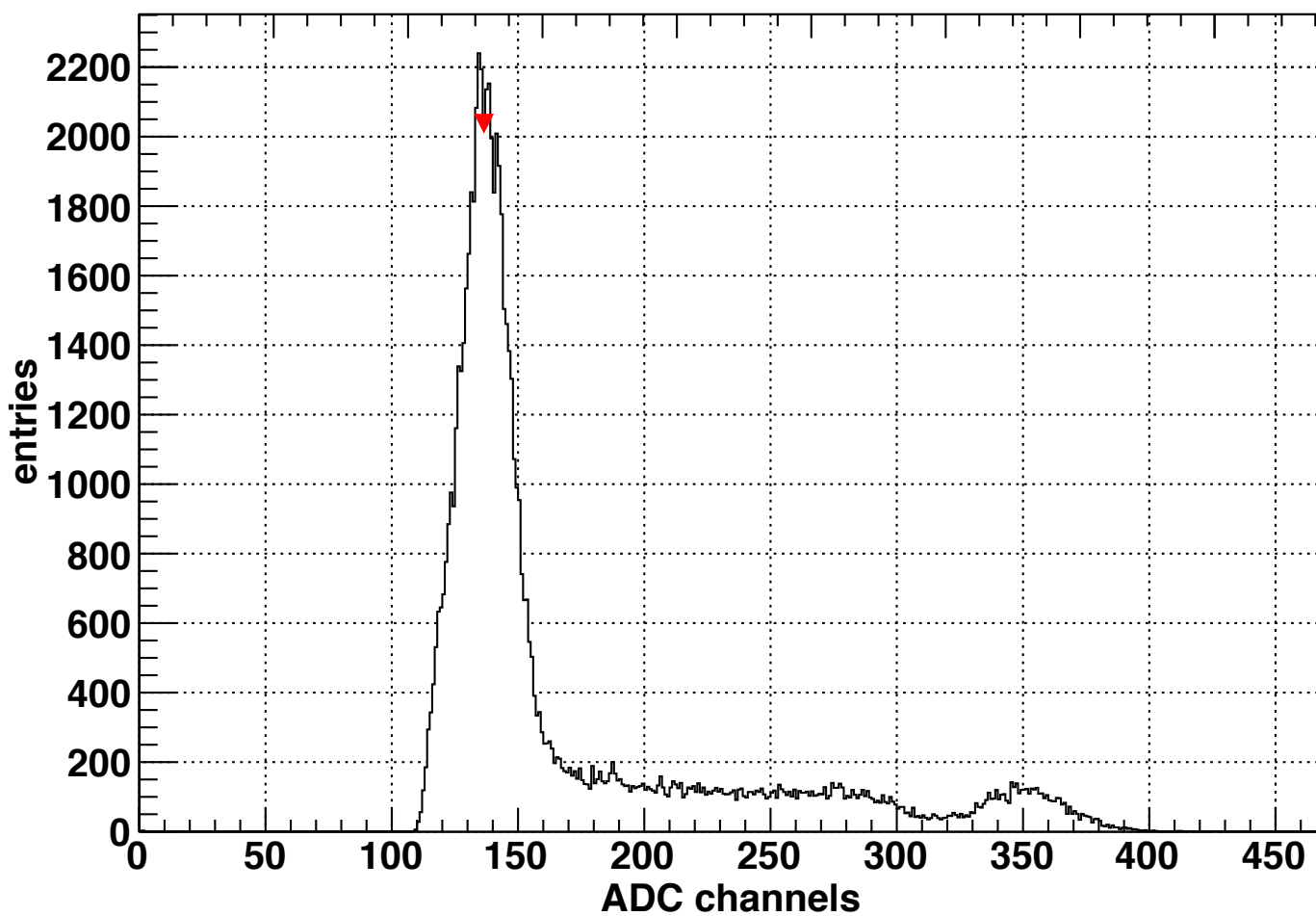
energy in keV



channel 84, peak at 136

energy in keV

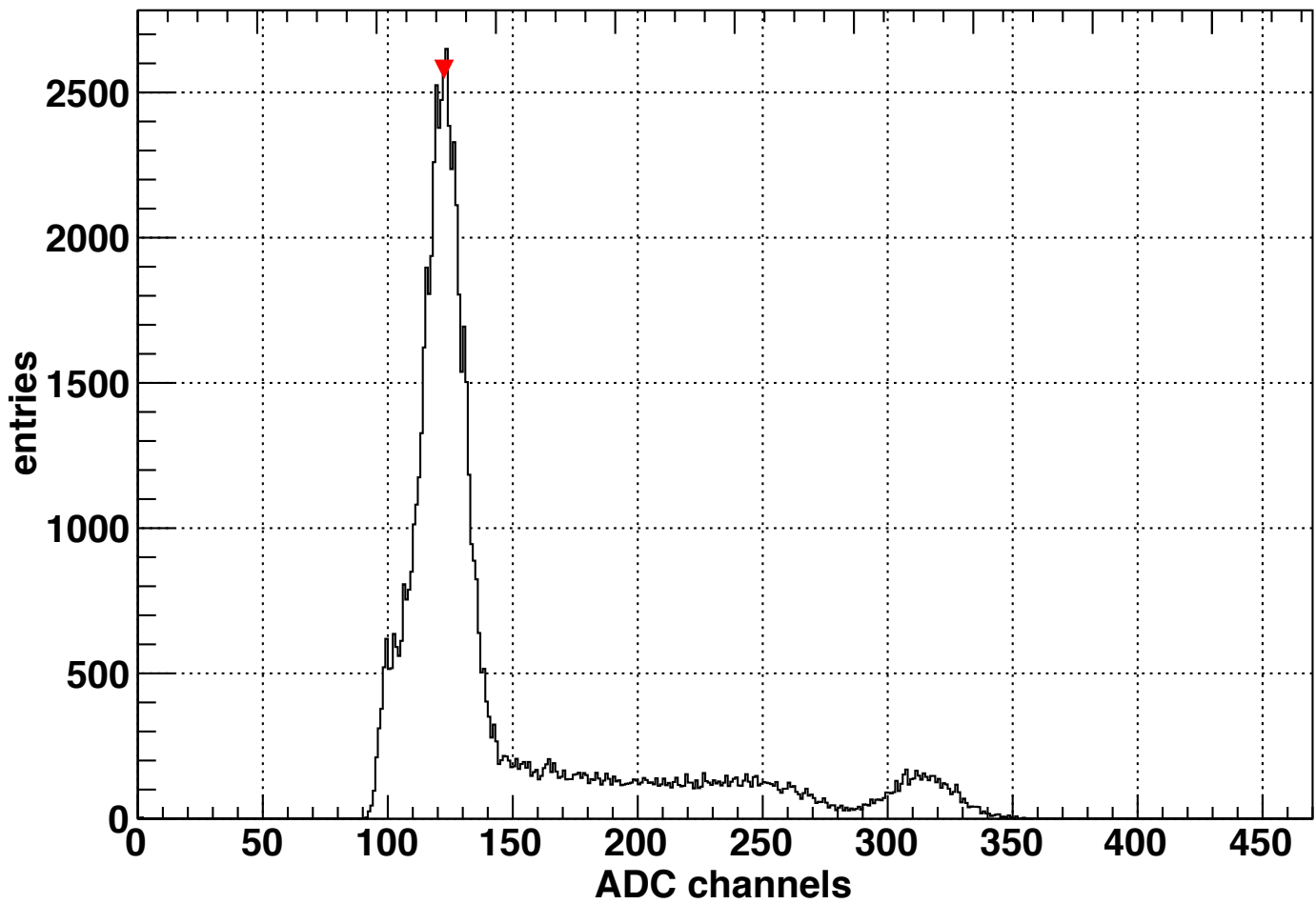
0 200 400 600 800 1000 1200 1400 1600



channel 85, peak at 122

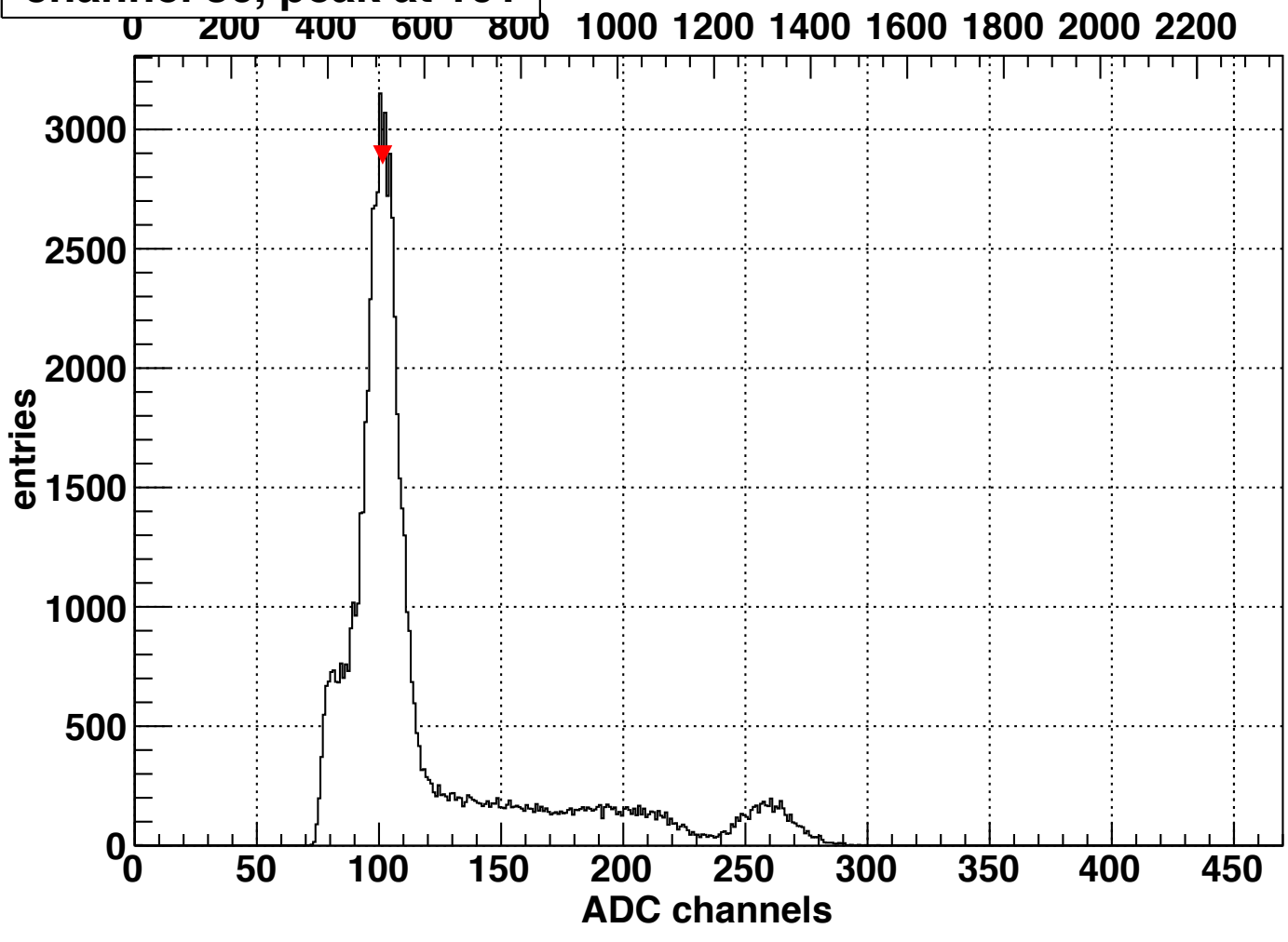
energy in keV

0 200 400 600 800 1000 1200 1400 1600 1800



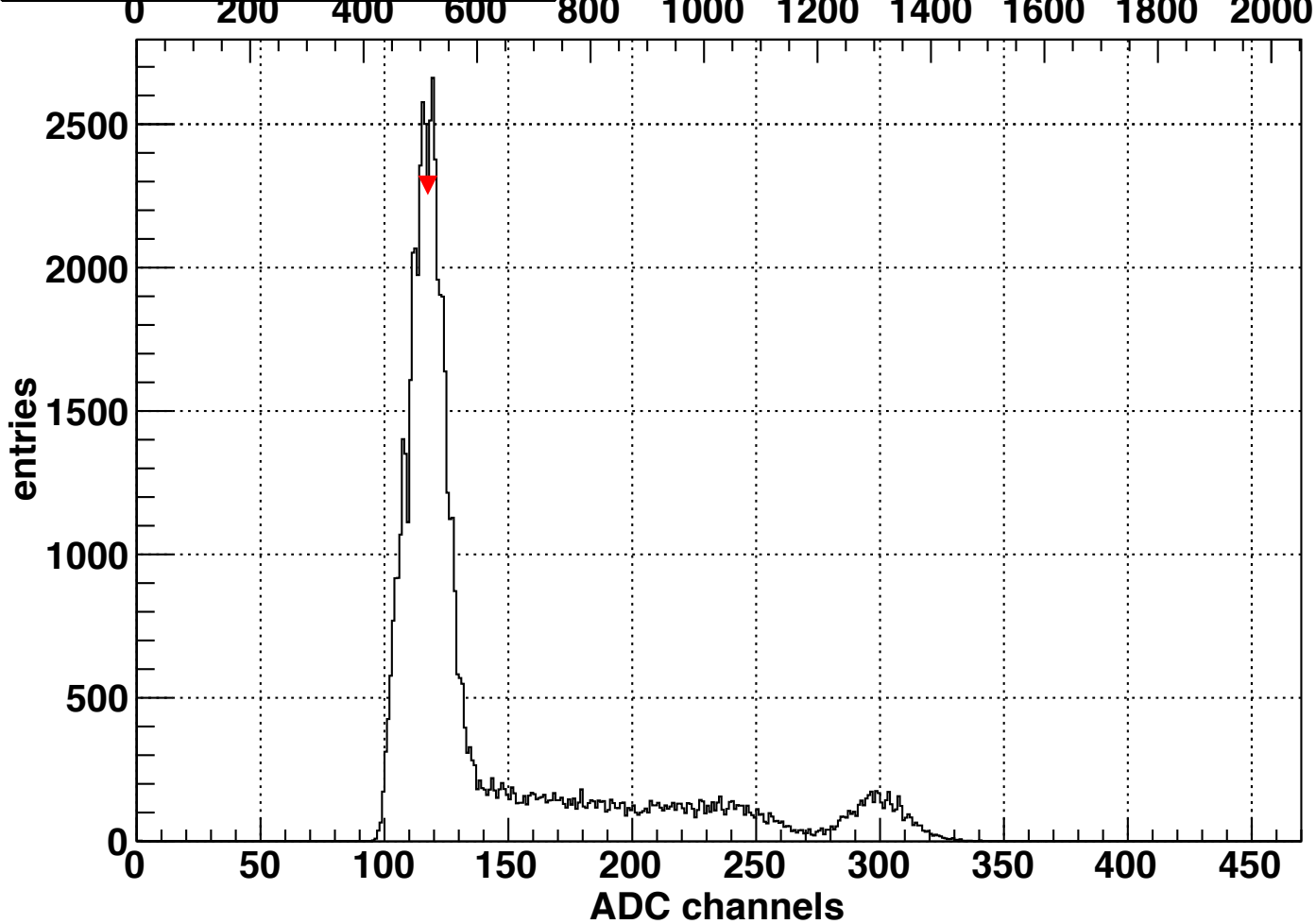
channel 86, peak at 101

energy in keV



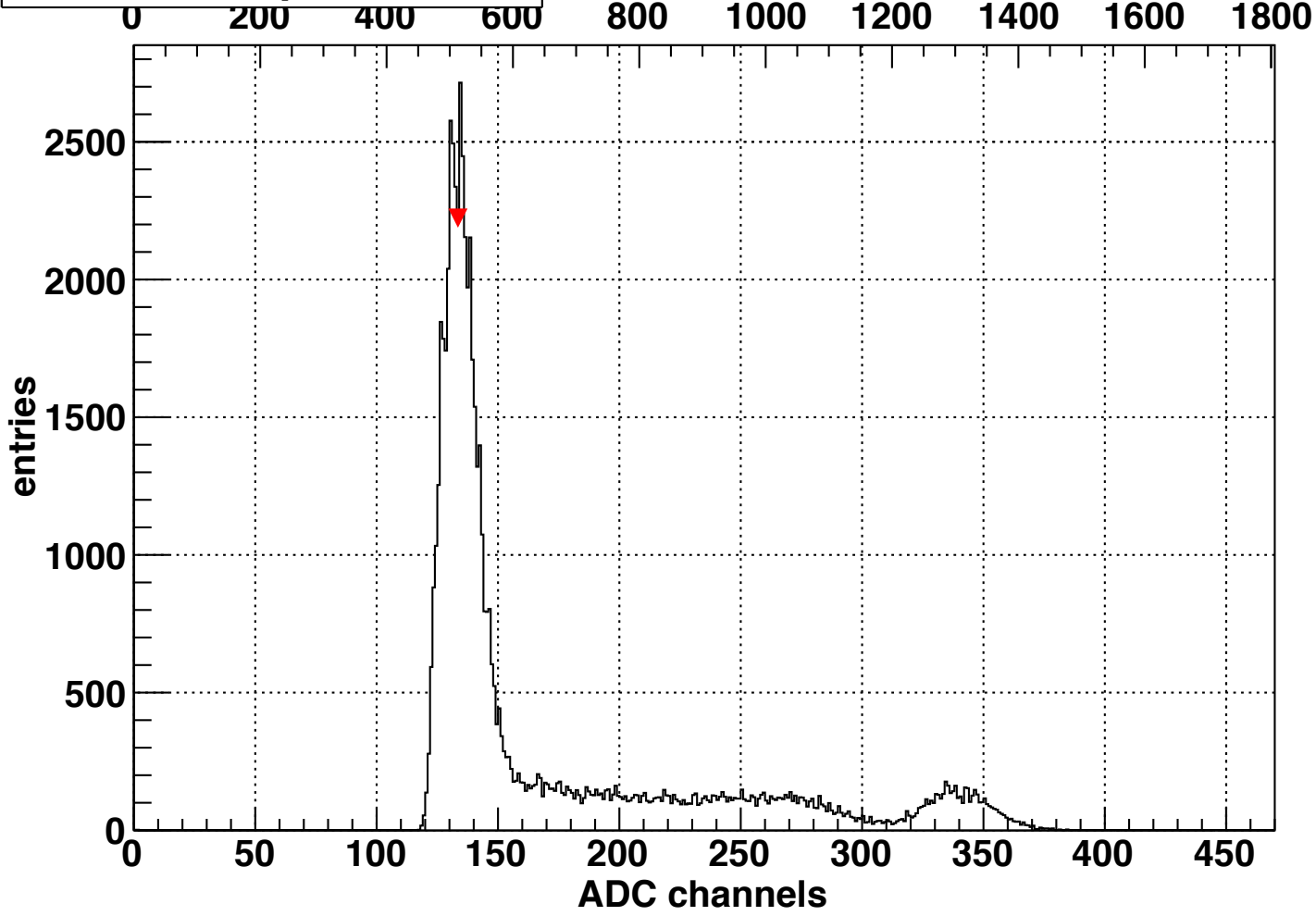
channel 87, peak at 117

energy in keV

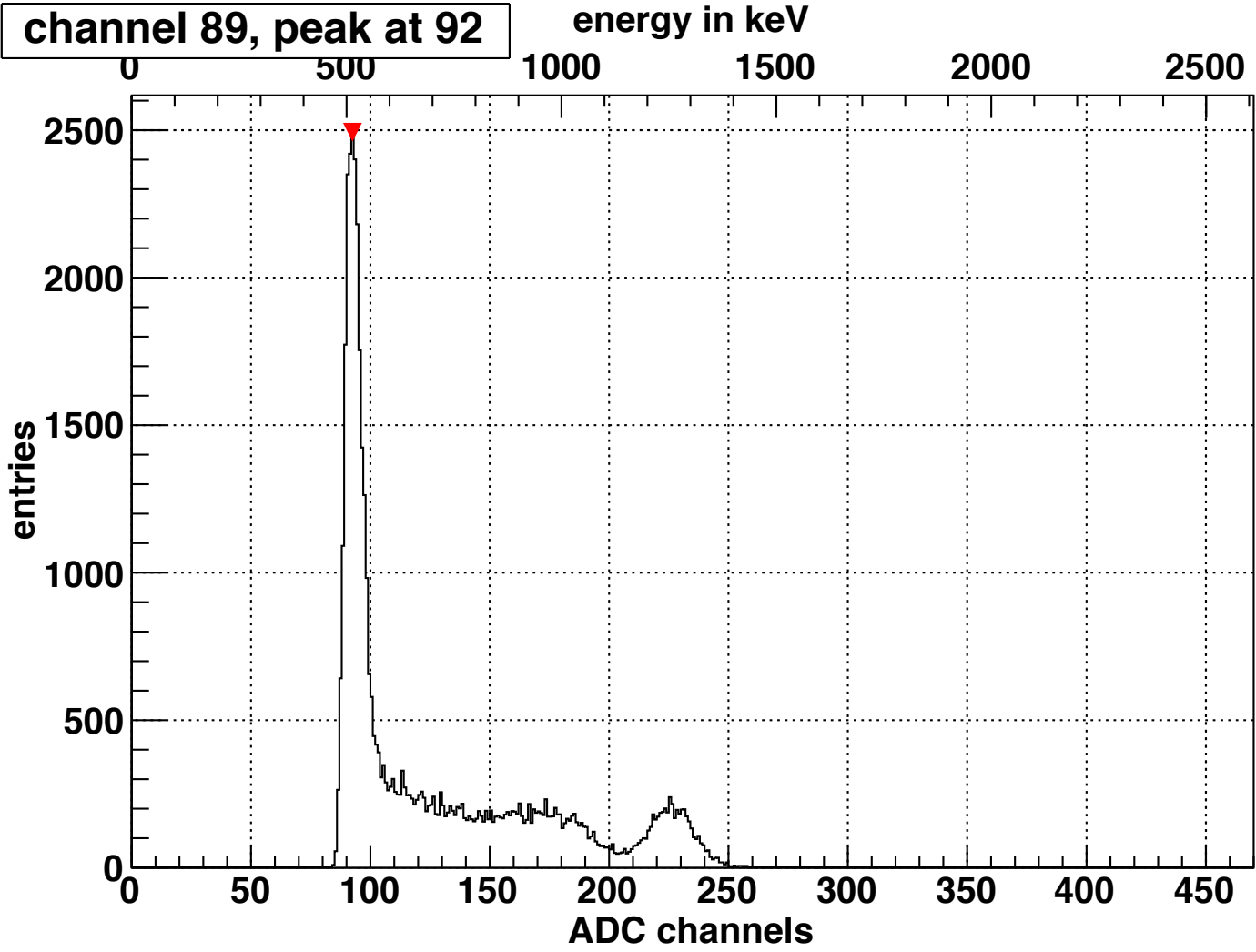


channel 88, peak at 133

energy in keV



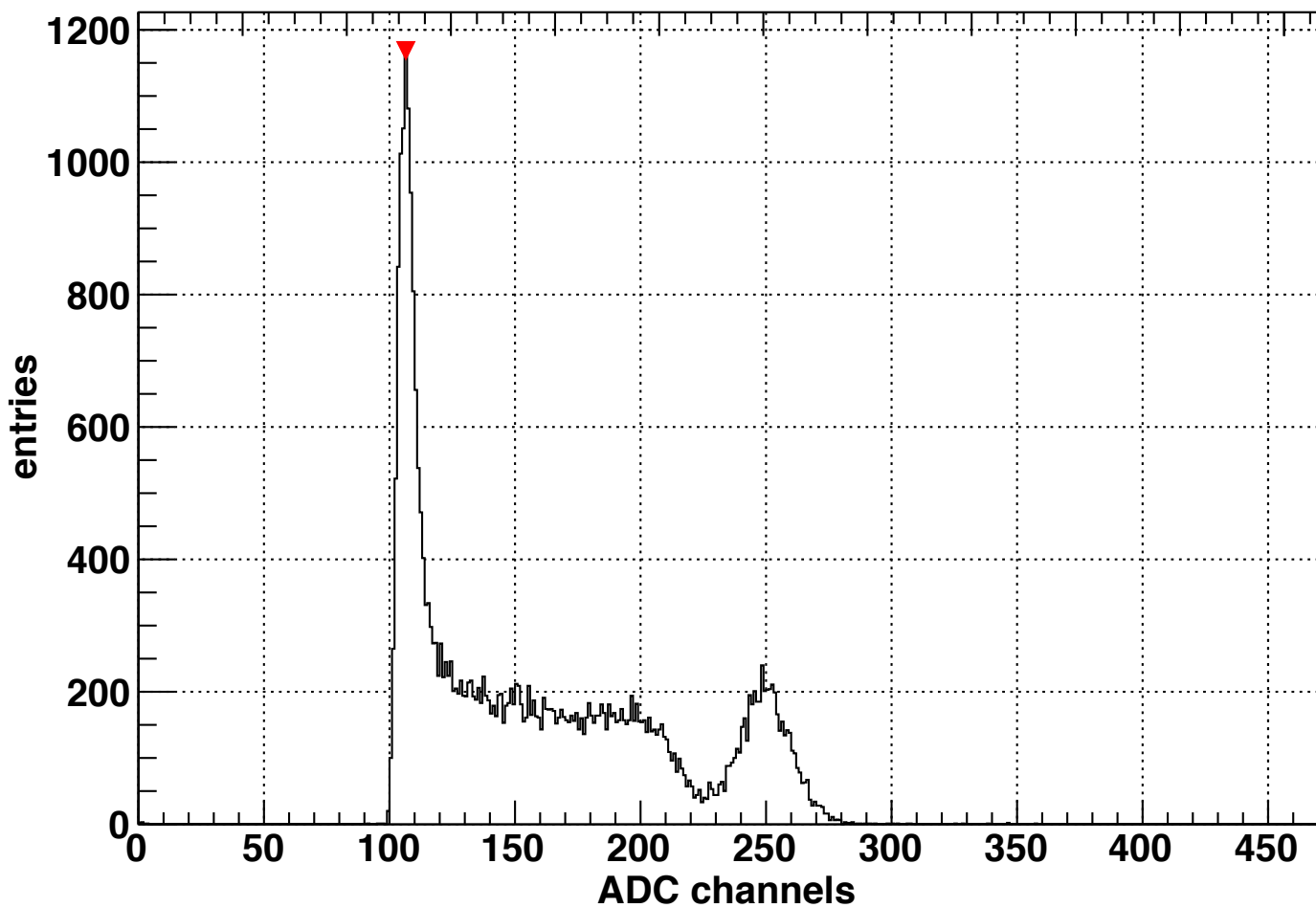
channel 89, peak at 92



channel 90, peak at 106

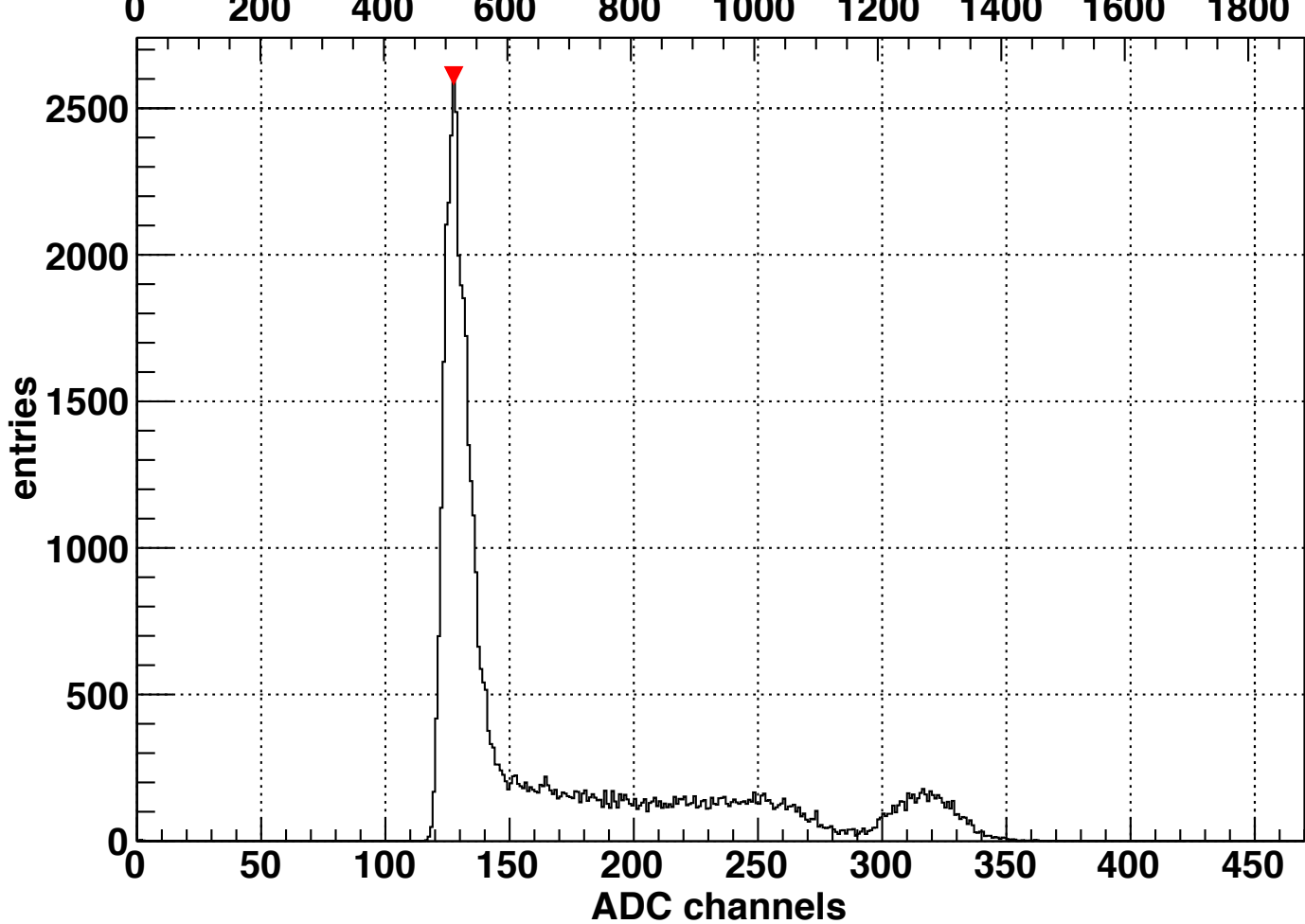
energy in keV

0 200 400 600 800 1000 1200 1400 1600 1800 2000 2200



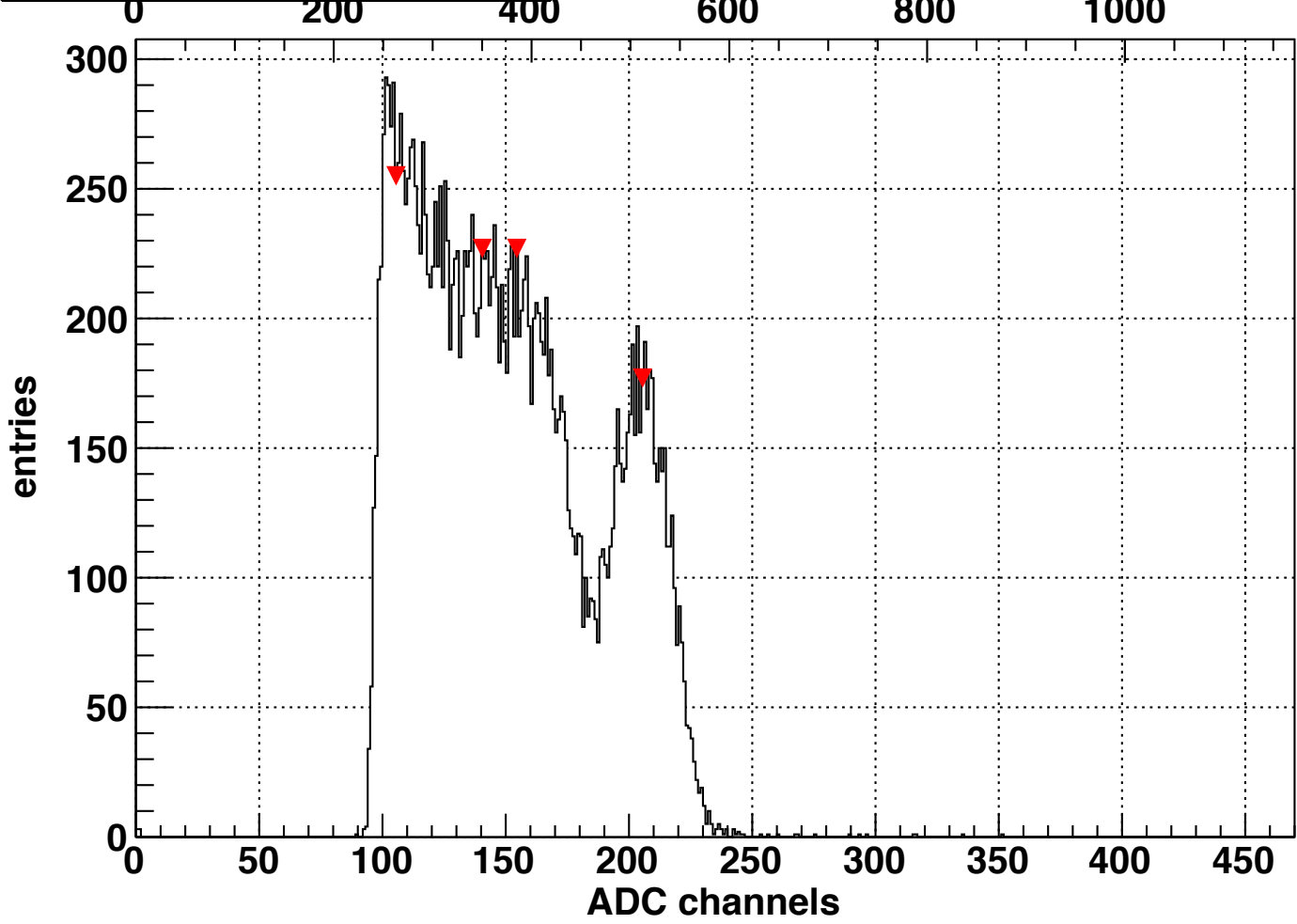
channel 91, peak at 127

energy in keV

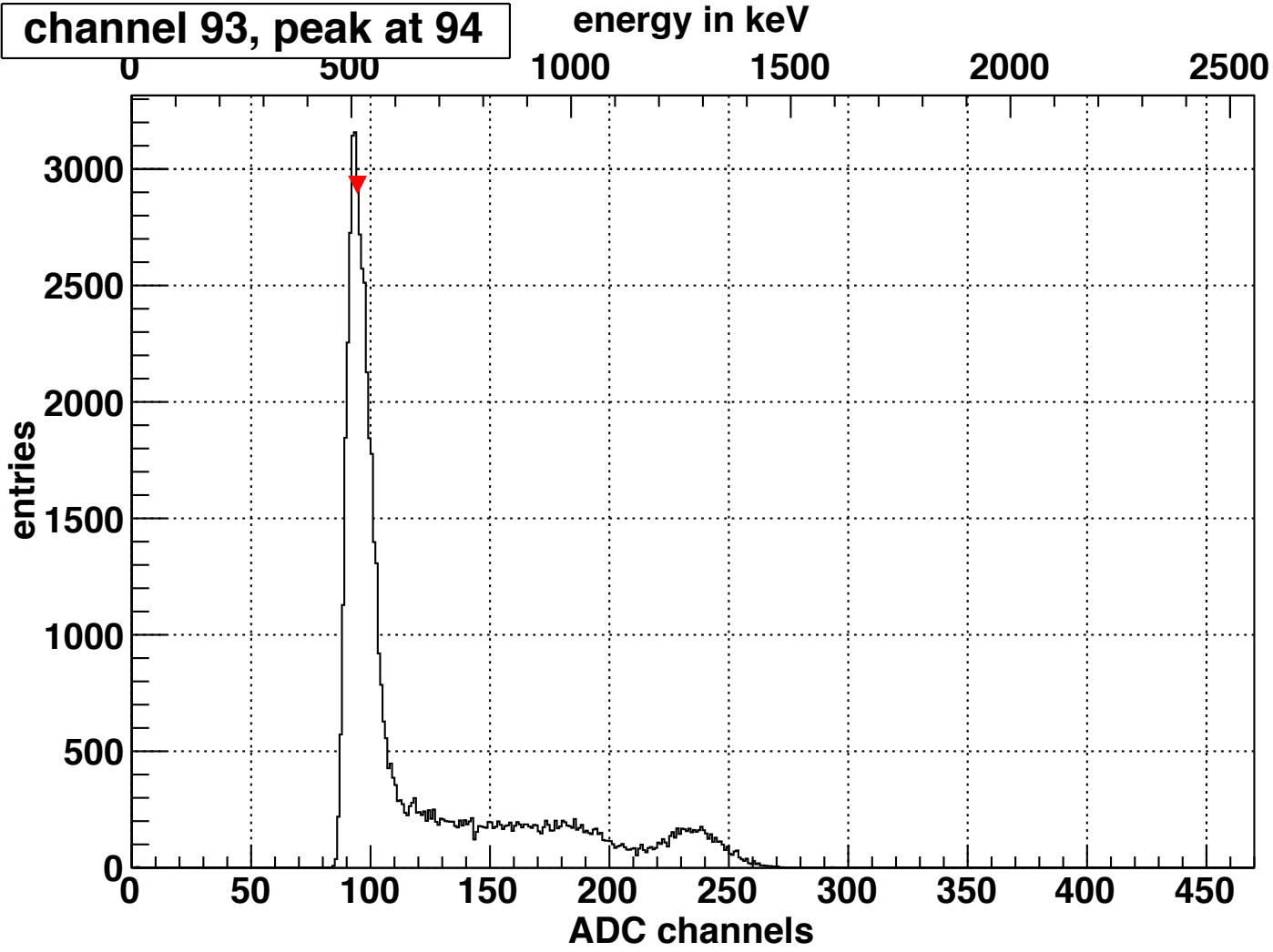


channel 92, peak at 205

energy in keV

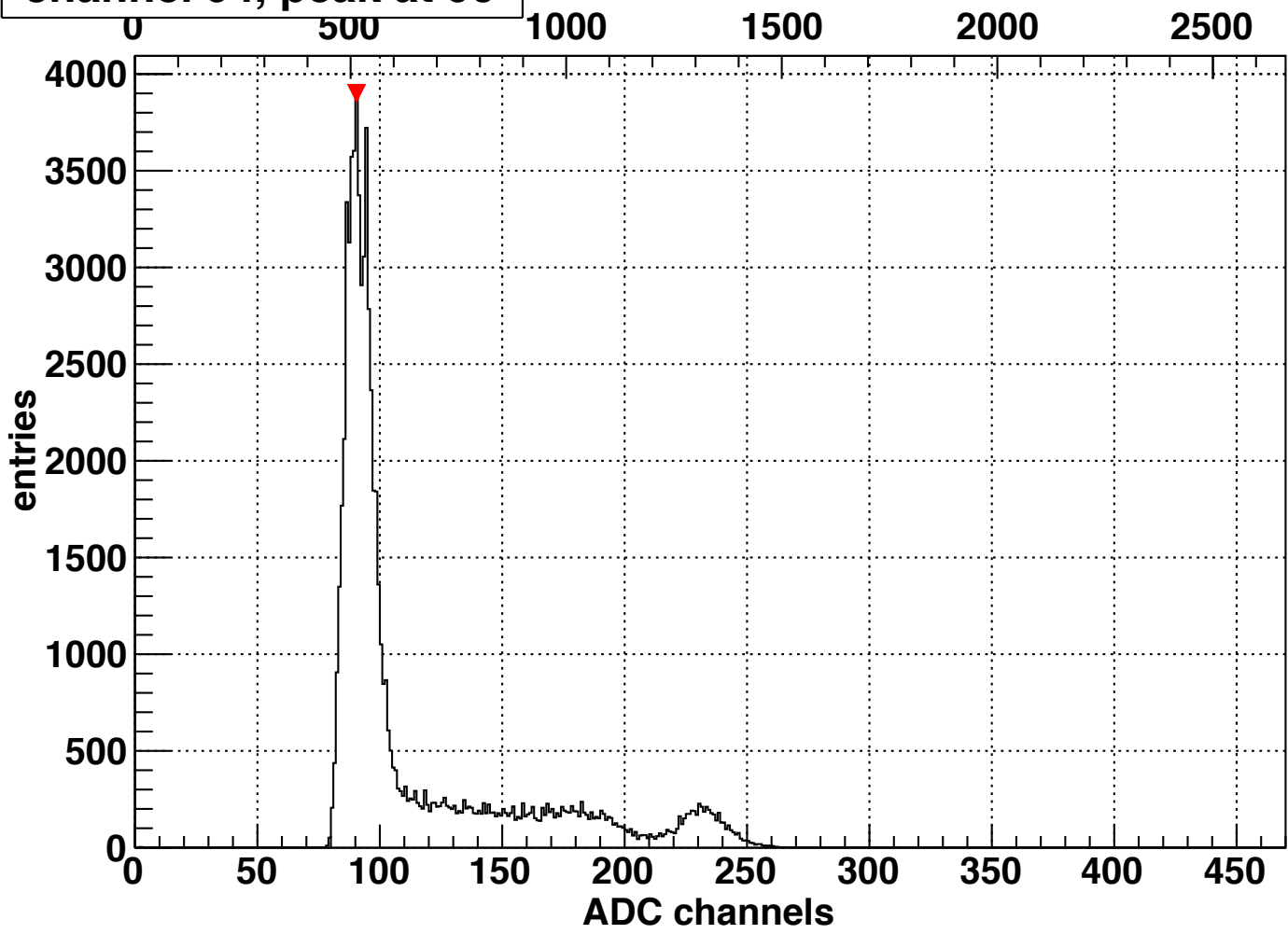


channel 93, peak at 94



channel 94, peak at 90

energy in keV



channel 95, peak at 117

energy in keV

